UNIVERSITY OF OKLAHOMA

GRADUATE COLLEGE

WET BULB GLOBE TEMPERATURE AND ASSOCIATED HEAT WAVES IN THE UNITED STATES GREAT PLAINS

A DISSERTATION

SUBMITTED TO THE GRADUATE FACULTY

in partial fulfillment of the requirements for the

degree of

DOCTOR OF PHILOSOPHY

By

BENJAMIN DAVIS
Norman, Oklahoma
2024

WET BULB GLOBE TEMPERATURE AND ASSOCIATED HEAT WAVES IN THE UNITED STATES GREAT PLAINS

A DISSERTATION APPROVED FOR THE
SCHOOL OF METEOROLOGY

BY THE COMMITTEE CONSISTING OF

Dr. Elinor Martin, Chair

Dr. Jeffrey Basara

Dr. Bradley Illston

Dr. Hank Jenkins-Smith

Dr. Jason Furtado

Acknowledgments

This dissertation is dedicated to my cat, Melody, who passed away during the writing of this dissertation.

I would like to thank my advisor Dr. Elinor Martin for all of the support and guidance provided throughout my time working on my PhD. I would like to thank my committee for their comments and feedback on this work. I would like to thank Dr. Bradley Illston for his assistance in understanding WBGT and implementing code to calculate WBGT, acquiring Oklahoma Mesonet data, and his feedback on the WBGT climatology paper that chapter 2 is largely based on. I would like to thank my research group for their support and feedback over the last few years. I would like to thank my friends and family for their support through my time in graduate school and through all of the ups and downs throughout.

This project was supported by the National Science Foundation EPSCoR program, Grant OIA-1946093.

Hersbach, H. et al., (2018) was downloaded from the Copernicus Climate Change Service (C3S) Climate Data Store. The results contain modified Copernicus Climate Change Service information 2022. Neither the European Commission nor ECMWF is responsible for any use that may be made of the Copernicus information or data it contains.

This work is based on S2S data. S2S is a joint initiative of the World Weather Research Programme (WWRP) and the World Climate Research Programme (WCRP). The original S2S database is hosted at ECMWF as an extension of the TIGGE database.

ENSO and MJO data Niño3.4 time series data used for the ENSO phases was downloaded from the NOAA Physical Sciences Laboratory at
https://psl.noaa.gov/gcos_wgsp/Timeseries/Nino34/, and is derived from the
HadISST1 dataset. MJO RMM phase data downloaded from the Australian Bureau of Meteorology at http://www.bom.gov.au/climate/mjo/

Table of Contents

List Of Tables

List Of Figures

Abstract

Heatwaves are a leading contributor of weather-related mortality, globally contributing to thousands of deaths each year. The impacts on humans may be direct or indirect through avenues such as heat stress, strained medical capacity, infrastructure breakdown, and reduced crop yields. While extreme heat is often measured by temperature and humidity, Wet Bulb Globe Temperature (WBGT) is commonly used to evaluate real-time heat stress risks in humans and correlates better with heat related illness, and is used by the Occupational Safety and Health Administration (OSHA) and the US Army. WBGT is a weighted average of air temperature, natural wet bulb temperature, and black globe temperature. A local hourly, daily, and monthly WBGT climatology will allow those planning outdoor work to minimize the likelihood of heat related disruptions. Further, understanding the characteristics of heat waves will allow emergency planners and responders to know what to expect when heat waves occur. Additionally, evaluating the predictability of WBGT heat waves allows an understanding of what advance warning may be possible and when confidence may be higher.

In this study, WBGT is calculated from the ERA5 reanalysis and is validated by the Oklahoma Mesonet and found to be adequate. Two common methods of calculating WBGT from meteorological observations are compared. The Liljegren method has a larger diurnal cycle than the Dimiceli method, with peak WBGT about 1 °F higher. The high and extreme risk categories in the southern United States Great Plains (USGP) have increased from 5 days per year to 15 days from 1960-2020. Additionally, the largest increases in WBGT are occurring during DJF, potentially lengthening the warm season in the future. Heat wave definitions based on maximum, minimum, and mean WBGT are used to calculate heat wave characteristics and trends with the largest number of heat waves occurring in the southern USGP. Further, the number of heat waves is generally increasing across the domain. This study shows that heat wave days based on minimum WBGT have increased significantly which could have important impacts on human heat stress recovery.

The predictive skill of WBGT heat waves is evaluated using ERA5 reanalysis and models from the S2S Project Database. North American atmospheric regimes are defined using K-Means clustering of detrended standardized 500 mb geopotential anomalies from ERA5 reanalysis. Additionally, heat wave types (e.g. Hot-dry or warm-humid) are defined using the standardized anomalies of temperature and humidity relative to other heat waves during the same season. An analysis of the predictive skill of atmospheric regimes, heat wave types, seasonality, and the impact of ENSO and the MJO is conducted using these datasets both with zero days lead time and at S2S lead times. Finally, regime statistics are calculated in S2S model forecasts to identify skill and forecast biases. Each regime has unique heat wave frequency, type, and seasonality characteristics. Heat waves may occur in the US Great Plains with greater than twice the climatological frequency in some regimes, however the increase is often seasonally dependent. Additionally, some skill is shown at discriminating between heat wave types in different regimes. Further, the regimes that are conducive to heat waves at short lead times differ from those that correlate with heat wave occurrence at longer lead times. When incorporating the ENSO or MJO phase heat wave in addition to the atmospheric regime, some additional predictive skill is observed, with the MJO providing more skill, as it introduces larger variation between regimes and provides information regarding timing of individual heat waves where the ENSO phase does not due to the much longer period. Combining both the ENSO and MJO phase provides the highest skill, with some ENSO/MJO/regime combinations having historically observed heat wave rates in excess of 50% at some lead times while other combinations are near 0% historically, thus leading to forecasts of opportunity when a signal for higher heat wave rates occurs. S2S models show statistically significant skill in forecasting most regimes up to 5 weeks lead time. However, the accuracy at predicting the correct atmospheric regime may not be useful beyond 1-2 weeks, which may limit the ability to incorporate regimes into heat wave forecasts at longer lead times, as this information is necessary for combination statistics that incorporate regimes.

Chapter 1

Introduction

Historic heat waves across Eurasia and North America in summer 2022 led to thousands of deaths. With global temperatures rising, similar levels of extreme heat will become more common with more frequent and intense heat waves expected in future climates (e.g Meehl and Tebaldi 2004; Teng et al. 2016; Perkins-Kirkpatrick and Gibson 2017; Lopez et al. 2019). Extreme heat leads to cascading effects such as strain on water supplies due to increased human and agricultural consumption, stress on electrical systems, and heat related illness occupying emergency medical resources (e.g. Lesk et al. 2022).

Heat waves are typically defined by air temperature (e.g. Meehl and Tebaldi 2004; Anderson and Bell 2011; Peng et al. 2011), or indices based on temperature and humidity (e.g. Steadman 1979, 1984; Tan et al. 2007), and require some minimum temporal extent (Smith et al. 2013). While using a definition solely based on temperature is convenient, and often necessitated by data limitations, air temperature does not fully capture what can make extreme heat deadly. For example, as humidity increases the human body is not able to effectively cool itself through sweat (Parsons 2006; Mora et al. 2017). In fact, if wet bulb temperature increases above 35 °C (95 °F) the human body is unable to cool to a safe level (Sherwood and Huber 2010), and in many situations this threshold may be much lower (Vecellio et al. 2022). One example of a heat wave where humidity played a significant role is the 1995 Chicago heat wave where over 500 people died over a 48-hour period (Kunkel et al. 1996; Karl and Knight 1997).

However, even humid-heat measures such as wet bulb temperature or heat index do not fully capture the physical response to extreme heat as they do not account for the wind or solar radiation, both of which can contribute to personal heat stress. In some cases the effects of these factors can be significant and result in an incorrect estimation of heat stress. Several indices have been created to measure heat stress that consider a broader range of conditions with fewer assumptions (Epstein and Moran 2006; Liljegren et al. 2008; Buzan et al. 2015) and organizations such as the Occupational Safety and Health Administration (OSHA) and the US Army use Wet Bulb Globe Temperature (WBGT) (Departments of Army and Air Force 2003; OSHA 2017). WBGT is an index that factors in temperature, humidity, wind speed, and solar radiation by taking a weighted average of dry bulb temperature, natural wet bulb temperature, and black globe temperature. By accounting for more factors, WBGT is able to better represent heat stress in humans than other metrics that just use air temperature and humidity. However, none of these metrics account for what a person is wearing and doing.

Research on WBGT has generally focused on how well it discriminates human mortality and its trend on climate scales. This research has shown that it is better at differentiating high mortality events from lower mortality events than temperature based metrics (Hyatt et al. 2010). Further, WBGT is increasing in much of the world as global temperatures increase (Hyatt et al. 2010; Knutson and Ploshay 2016; Li et al. 2020). The number of people annually exposed to extreme wet bulb globe temperatures (WBGT) above 33 °C (91.4 °F) has already tripled compared to pre-industrial numbers (Li et al. 2020). Climate projections show that WBGT will continue to increase in the future over most regions of the globe, with average WBGTs over land exceeding 1970's record maxima by the 2030's under the RCP 8.5 scenario (Li et al. 2017).

The increasing exposure to heat risk underlines the importance in understanding how heat risk presents itself. By understanding the climatology of heat risk and how

it is changing planners can better plan around typical periods of enhanced heat risk, such as scheduling for outdoor labor, and mitigate lost work due to heat risk. For emergency managers, understanding the characteristics and trends in heat waves can assist in preparing to respond when a heat wave is expected to occur. While risks in the United States Great Plains (USGP) are typically studied in terms of temperature, expanding the understanding of heat climatology and heat wave characteristics to a WBGT definition will allow this information to more accurately target conditions that impact human health outcomes. These are discussed in Chapter 2. However, while knowing what a heat wave looks like might help emergency responders prepare to respond to a heat wave, it is also beneficial to know when a heat wave might happen in advance in order to be able to respond as quickly as possible or even take mitigating action in advance, such as preparing to open cooling shelters and staffing medical facilities. Forecasts at subseasonal-to-seasonal (S2S) timescales, which is 2 weeks to 2 months, can assist in this planning and preparation. Chapter 3 quantifies sources of WBGT heat wave predictability such as ENSO, the MJO, and seasonality, and which factors lead to elevated WBGT to improve the ability to forecast specific events at S2S time scales.

It is hypothesized that WBGT heat wave climatology, trends, and sources of predictability will behave in similar ways to temperature based heat waves due to the high correlation between WBGT and temperature. However, as WBGT is a function of more variables, some situations may exist where WBGT may better describe the heat risk, such as those situations where humidity is a significant factor in heat risk. In this study several sources of predictability are evaluated to determine what skill at predicting WBGT heat waves exists. Additionally, it is important to understand the characteristics of heat waves when they occur, and what are normal conditions.

Chapter 2

Climatology of Wet Bulb Globe Temperature and Associated Heat Waves in the United States Great Plains

The material in this section is reproduced from Davis, B, E. R. Martin, and B. G. Illston, 2024: Climatology of Wet Bulb Globe Temperature and Associated Heat Waves in the United States Great Plains. *Journal of Applied Meteorology and Climatology. In review.*

Additionally, much of the material in Chapter 1 is based on this manuscript as well.

2.1 Background

Extreme heat often occurs over several days as heat waves. Studies such as Anderson and Bell (2011) suggest that longer, more intense heat waves, as well as the first heat wave of the year typically have the largest effects on human mortality, as no opportunity to acclimate to such conditions has occurred. Further, mean and minimum temperature are shown to be just as important to predicting human mortality as maximum temperature (Robinson 2001; Hajat et al. 2002; Nissan et al. 2017; Heo et al. 2019). In some locations, such as Florida, mean and minimum air temperature, heat index, and WBGT are increasing at faster rates than the maximum of the same metrics (McAllister et al. 2022). As temperature variability could increase in the future, the

frequency and/or intensity of heat waves could increase (Teng et al. 2016). However, as WBGT is a function of more environmental variables, WBGT heat wave characteristics have been shown to differ from those of temperature based heat waves in some regions. In South Korea, Heo et al. (2019) showed that heat waves defined by WBGT last 15% longer than those defined by air temperature or heat index, motivating a need to understand the behaviour of heat waves defined by WBGT in the USGP.

In the USGP, a region with large gradients in environmental quantities such as temperature and humidity, our understanding of heat waves has focused on temperature based definitions (e.g. Anderson and Bell 2011; Peng et al. 2011; Smith et al. 2013, Perkins-Kirkpatrick and Gibson 2017). Heat waves in the USGP typically occur with high pressure and clear skies with at least one heat wave on average each summer (e.g. Anderson and Bell 2011; Smith et al. 2013; Teng et al. 2013). Heat waves are often preceded by 15-20 days by anomalous mid-latitude planetary waves with wave number 5 (Teng et al. 2013). Additionally, heat waves in the USGP and mid-latitudes have also been shown to be driven by latent heat release by the Southeast Asian monsoon (Lopez et al. 2019) and La Niña (Hoerling et al. 2014; Seager et al. 2014; Lopez et al. 2019).

As WBGT is better than air temperature and other common humid-heat metrics at predicting human mortality, and the increased urgency in discriminating between heat mortality events, it is important to understand extreme heat events under the WBGT paradigm. This study creates a gridded climatology of WBGT from reanalysis data in the USGP calibrated by observations from the Oklahoma Mesonet and uses this climatology to define heat waves in the USGP in order to provide a basis for future work evaluating extreme heat in the USGP.

2.2 Data and Methods

2.2.1 Oklahoma Mesonet

The Oklahoma Mesonet records five minute observations of meteorological variables at 120 sites (https://www.mesonet.org/about/mesonet-sites) across the state of Oklahoma (Brock et al. 1995; McPherson et al. 2007). This study uses 1.5-meter air temperature, 2- and 10-meter wind speeds, 1.5-meter dew point temperature, surface pressure (measured at 0.75 m), and incoming solar radiation (measured at 1.5 m) from 1998-2020 to calculate WBGT using the instantaneous observations at the top of every hour. The Oklahoma Mesonet data are used to verify the WBGT calculations as described in section 2.2.3.

2.2.2 Fifth Generation ECMWF Atmospheric Global Reanalysis (ERA5)

ERA5 reanalysis hourly data on single levels from 1960-2020 is used for this study (Hersbach et al. 2018). Several recent studies have used hourly ERA5 for calculating WBGT using various formulations (Li et al. 2020; Spangler et al. 2022; Kong and Huber 2022). To calculate WBGT, the following ERA5 variables are used: 2-meter temperature, 2-meter dewpoint temperature, downward shortwave solar radiation flux (solar radiation), 10 meter wind speed, and surface pressure. 2-meter wind speed is extrapolated from 10 meter wind speed as described in 2.2.3. All variables are interpolated to a 0.5 ° x 0.5 ° grid via an option in the ERA5 API at the time of download due to storage limitations. As the climatological analyses conducted in this study are investigating large-scale patterns or shown for a single point the coarser spatial resolution has minimal impact on the results. While the Oklahoma Mesonet

solar radiation is instantaneous, the downward shortwave solar radiation flux from ERA5 is a time average over the 1 hour leading up to the analysis time. Due to the time averaging, the ERA5 downward shortwave solar radiation flux is valid at HH:30. To account for the timing differences the ERA5 downward shortwave solar radiation flux is linearly interpolated to HH:00 to match the valid time of all remaining data.

2.2.3 WBGT Calculation

WBGT can be measured using specialized equipment that measures wet bulb temperature, dry bulb temperature, and black globe temperature at 2m above ground level. However, this equipment is expensive and not commonly placed at meteorological observing stations. As a result, several studies have derived formulations of WBGT based on standard meteorological variables (Hunter and Minyard 1999; Matthew et al. 2001; Liljegren et al. 2008; Dimiceli et al. 2011). These formulations are often able to recreate WBGT to within 1 °C (1.8 °F) of the instrumentation.

This study calculates WBGT from the Oklahoma Mesonet observations (2.2.1) and ERA5 reanalysis (2.2.2). Oklahoma Mesonet data are regridded to a 0.5 ° x 0.5 ° grid to match the ERA5 grid prior to calculating WBGT. Missing data and data that failed the Oklahoma Mesonet quality control procedure are removed prior to interpolation.

This study uses two methods to calculate WBGT. Both methods calculate WBGT following eq. (2.1) (Yaglou and Minard 1957), but differ in their calculation of T_{bg} and T_{nwb}. In the first method, Dimiceli WBGT, which is used operationally by the Oklahoma Mesonet, T_{bg} is calculated following Dimiceli et al. (2011) and wet bulb temperature is calculated following the operational equations used by the Oklahoma Mesonet, which in turn were obtained from the National Weather Service, and is described in eqs. (2.2)-(2.5) (Bradley G. Illston, 2021, personal communication).

$$WBGT = 0.7 * T_{nwb} + 0.2 * T_{bgt} + 0.1 * T_{db} \tag{2.1}$$

$$T_{LCL} = T_d - (0.212 + (0.01571 * T_d) - 0.000436 * T_{db}) * (T_{db} - T_d) + 273.15 \tag{2.2}$$

$$r = 6.21 \frac{e_s}{p_s - e_s} \tag{2.3}$$

$$e_s = 6.11 * 10^{\frac{7.5 * T_d}{T_d + 237.3}} \tag{2.4}$$

$$\theta_e = T_{db} \left(\frac{1000}{p_s} \right)^{\frac{R_d}{c_p}(1 - 0.28 * r)} exp^{(\frac{3376}{T_{LCL}} - 2.54) r (1 - 0.81 r)} \tag{2.5}$$

The Dimiceli et al. (2011) black globe temperature is derived by linearizing the energy balance equation from Hunter and Minyard (1999), modified to include a convective heat transfer coefficient that is a function of the solar zenith angle and the solar irradiance, about T_{bg}=40 °C. To solve for wet bulb temperature, we first solve eqs. (2.2)-(2.5) using the observed T_{db} and T_d, to obtain an observed θ_e. In eq. (2.2) T_{LCL} is the temperature (in Degrees K) at the lifting condensation level (LCL), T_{db} and T_d are the 2-meter dry bulb air temperature and 2-meter dewpoint temperature (°C). In eq. (2.3) r is the mixing ratio, p_s is the surface pressure (hPa) and e_s is the saturation vapor pressure (hPa), which is calculated by eq. (2.4). In eq. (2.5) θ_e is the equivalent potential temperature (degrees K), R_d is the dry air gas constant and c_p is the heat capacity of dry air at constant pressure. Note that in eq. (2.5) T_{db} is in Kelvin. Second, replace T_{db} and T_d with T_{wb} (i.e. $T_{db} = T_d = T_{wb}$) in eqs. (2.4)-(2.5), where

T_{wb} is the wet bulb temperature (°C, except in eq. 2.5 where it is degrees K). T_{LCL} remains the same value as calculated from the observed T_{db} and T_d. Finally, iterate T_{wb} and solve eqs. (2.3)-(2.5) until the value of θ_e matches the value calculated from the observed T_{db} and T_d.

Natural wet bulb temperature is then calculated following eq. (2.6) (Hunter and Minyard 1999), where T_{nwb} is natural wet bulb temperature (°C), ws_{2m} is 2-meter wind speed (m/s), and $Srad$ is incoming solar radiation (W/m^2).

$$T_{nwb} = T_{wb} + max(0, ((0.0021 * Srad) - (0.43 * ws_{2m}) + 1.93)) \tag{2.6}$$

The second method used in this study to calculate WBGT, Liljegren WBGT, follows Liljegren et al. (2008) for both T_{bg} and T_{nwb}, which is calculated using cython code obtained from Kong and Huber (2022). Unlike Dimiceli et al. (2011), the Liljegren et al. (2008) T_{bg} is not linearized and is more computationally expensive. A full description of this method can be found in Liljegren et al. (2008) and Kong and Huber (2022). Notable differences between the results from the two methods are discussed where appropriate.

Because 2-meter wind speed is not available in ERA5, it is extrapolated using the log law (equation 2.7) with roughness length derived empirically from the 2- and 10-meter winds in the Oklahoma Mesonet data for each spatiotemporal grid point.

$$u_1 = u_2 \frac{ln(\frac{z_1}{z_0})}{ln(\frac{z_2}{z_0})} \tag{2.7}$$

In eq. (2.7) , u_1 and u_2 are wind speed at 2 different heights, z_1 and z_2 are the respective heights of u_1 and u_2, and z_0 is the roughness length. The spatial and temporal mean of all grid points west of 97 °W is calculated for each hour 00 UTC-23 UTC each calendar month. Terrain east of 97 °W in Oklahoma is much rougher

than that west of 97 °W and the rest of the USGP due to the Ouachita and Ozark Mountains as well as forests and is therefore not representative of the roughness length in the remainder of the domain. Roughness length values outside of [0,2] are excluded as these result in either non-physical values or wind speeds decreasing with height. Further, when observed 2-meter winds are greater than observed 10-meter winds, the roughness length rapidly increases, greatly biasing the mean roughness length. The empirical roughness lengths are in line with those expected for typical plains grassland during the daytime (Krishnamurthy et al. 2021). A consequence of this method is that typical stability parameters that affect the apparent roughness length are implicitly included in the calculated roughness length, so while this method does not calculate true roughness length, it does calculate the effective roughness length. Therefore to account for the different stability regimes throughout the day and year, this study uses a unique climatological effective roughness length value for each hour of the day and each month for the calculation of WBGT.

2.2.4 WBGT Risk Categories

WBGT is often divided into risk categories based on the human impacts and necessary precautions needed to avoid heat stress. The National Weather Service (NWS) and the Oklahoma Mesonet use the categories in Table 2.1, which we refer to throughout as "Uniform Categories". WBGT is shown in Table 2.1 in °F and throughout the paper for consistency with operational users such as the NWS, the Oklahoma Mesonet, OSHA, and the US Army. As acclimation varies based on local climatology, the risks associated with a given WBGT range may vary regionally. Grundstein et al. (2015) proposed regional adjustments to these risk categories based on local MJJAS 90th percentile of daily maximum WBGT, which were calculated from airport surface observation using the Liljegren et al. (2008) model for WBGT. Areas with 90th percentile of mean

MJJAS <86 °F are classified as Region 1, areas between 86 and 90 °F are classified as Region 2, and >90 °F are classified as Region 3, and adjusts the risk category ranges per region as shown in Table 2.2. This study considers these adjustments using regions shown in Figure 2.1 which approximates the regions in Grundstein et al. (2015) while considering differences between the datasets and WBGT calculation method used. Specifically, this study follows the methods of Grundstein et al. (2015) except that the the 90th percentile of daily maximum WBGT ranges that classify each region are shifted 4.0 °F cooler for Dimiceli WBGT and 2.0 °F cooler for Liljegren WBGT. These offsets are determined by finding the value that best aligns the boundaries of the regions calculated from our WBGT datasets (Fig. 2.1) with those presented in Grundstein et al. (2015). The risk thresholds for the Grudstein regions are as shown in Table 2.2 and are referred to throughout the paper as "Regional Categories." Note that the same risk levels are used for all WBGT datasets, and thus will not offset any differences between the two datasets.

2.2.5 Heat Wave Definition

Three definitions for heat waves are used in this study due to the importance of maximum daytime temperatures and warm overnight minimum temperatures to human heat stress. The first definition uses daily maximum WBGT, the second uses daily minimum WBGT, and the third uses daily mean WBGT. The daily maximum, minimum, and mean WBGT are defined as the maximum, minimum, and mean of the hourly WBGT values from 00 UTC through 23 UTC each day respectively. A WBGT daily threshold is established by taking a centered 31 day period and calculating the 90th percentile over the 61 year period of record. For each definition, a heat wave is

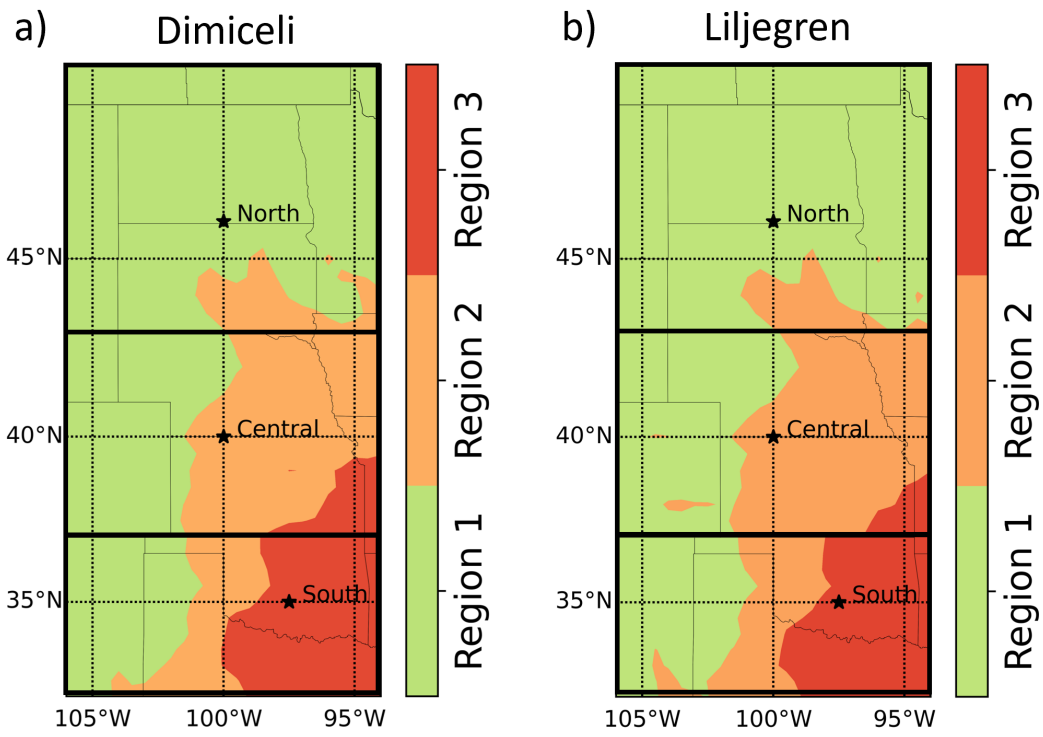

Figure 2.1: Map of regional categories based on Grundstein et al. (2015) as used throughout the dissertation, with boxes representing the northern, central, and southern USGP subdomains and locations used for point analysis from the Northern, Central, and Southern USGP indicated by stars. a) Dimiceli WBGT, b) Liljegren WBGT.

declared when the metric is at or above the threshold for two consecutive days. A heat wave is terminated when the metric is below the threshold for two consecutive days. The two days at the end which fail to meet the threshold are not considered part of the heat wave. However, once a heat wave begins, a single day below the threshold will not terminate the heat wave. This is done to prevent a single prolonged period of extreme heat from being counted as separate heat waves because a single day may have been just below the threshold.

2.2.6 Statistical Significance

Statistical significance of trends throughout this study is calculated using two-tailed Monte Carlo resampling. The analysis is repeated 5000 times while randomly shuffling the order of the years without resampling each iteration. A trend is considered statistically significant at the 95% confidence level (α=0.05) if it is below the 2.5 percentile or above the 97.5 percentile ($\alpha/2$) of the trends calculated from the randomly sampled data.

Table 2.1: WBGT heat risk categories as defined by the Oklahoma Mesonet and the NWS and work/rest recommendations for unacclimated individuals (Oklahoma Mesonet 2016).

$RiskLevel$	$RiskCategory$	$WBGT(°F)$	$LightWork$	$ModerateWork$	$HardWork$
0	No Risk	<80	50/10 min	40/20 min	30/30 min
1	Low	80-85	40/20 min	30/30 min	20/40 min
2	Moderate	85-88	30/30 min	20/40 min	10/50 min
3	High	88-90	20/40 min	10/50 min	avoid
4	Extreme	>90	10/50 min	avoid	avoid

Table 2.2: Regional WBGT heat risk categories as adapted from Grundstein et al. (2015)

$RiskLevel$	$RiskCategory$	$Region1WBGT(^{\circ}F)$	$Region2WBGT(^{\circ}F)$	$Region3WBGT(^{\circ}F)$
0	No Risk	<76	<80	<82
1	Low	76-81	80-85	82-87
2	Moderate	81-84	85-88	87-90
3	High	84-86	88-90	90-92
4	Extreme	>86	>90	>92

2.3 Verification of WBGT

2.3.1 Verification of ERA5 Ability to Recreate Observations

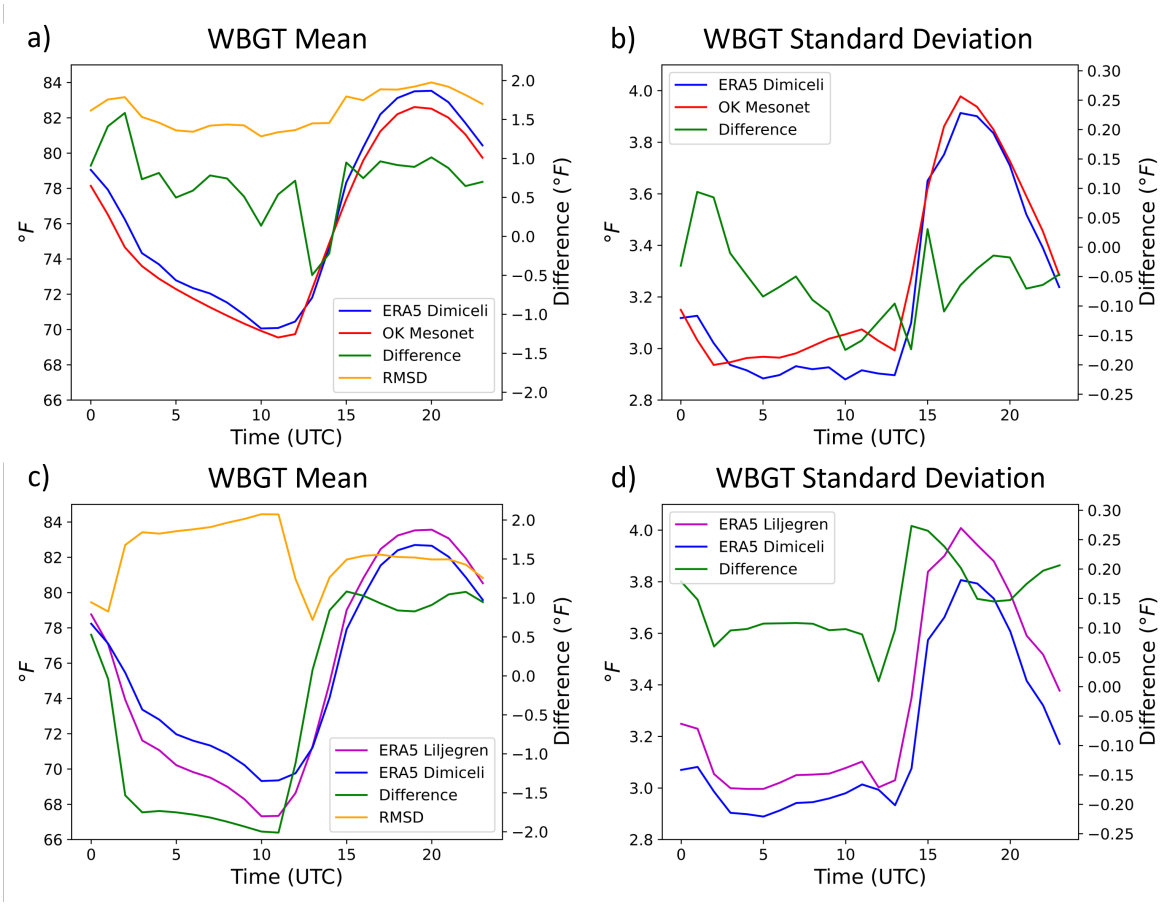

Figure 2.2: Verification of July a,b) ERA5 Dimiceli WBGT against Oklahoma Mesonet Dimiceli WBGT by hour showing area averaged values and differences for the state of Oklahoma west of 97 °W and c,d) ERA5 Dimiceli WBGT against ERA5 Liljegren WBGT by hour showing area averaged values and differences for the state of Oklahoma. a,c) Mean, difference, and RMSD of WBGT, and b,d) standard deviation of WBGT.

Before ERA5 can be used to investigate WBGT, it must first be verified that it is capable of accurately representing WBGT. Here, WBGT is calculated from the ERA5 using Dimiceli's WBGT formulation and the mean and standard deviation are compared to those from WBGT calculated from Oklahoma Mesonet observations, and

the root mean square difference (RMSD) between the two WBGT datasets is calculated (shown in Fig. 2.2a,b for July). Values are area averaged for all points in Oklahoma west of 97 °W. The difference in the mean is between 0.5 and 1.0 °F (0.3 and 0.6 °C) and the absolute difference in standard deviation is typically under 0.2 °F (0.1 °C), which is less than 5% error. The difference in mean is mostly explained by a difference in the temperature overnight and difference in dewpoint temperature during the day. Finally, the RMSD is typically $\leq$1.8 °F (1 °C). As this error is smaller than the categorical ranges (Tables 2.1 and 2.2), this is sufficiently small to be certain of the results within +/- 1 risk category. Further, the largest errors in the mean are overnight when temperatures are the coolest. The combination of these results suggests that WBGT has been well recreated by the ERA5 reanalysis. Other comparisons, such as Liljegren et al. (2008), have concluded that similar errors compared to a reference are acceptable. Other months (not shown) show similar results.

2.3.2 Comparison of Dimiceli and Liljegren WBGT

As with the comparison between ERA5 and Oklahoma Mesonet WBGT, the Dimiceli and Liljegren WBGT formula are compared. Notably, the Liljegren formula results in lower WBGT overnight but higher WBGT during daytime hours throughout the year (as shown in Fig. 2.2c,d for July). The larger diurnal range in Liljegren WBGT explains the necessity of using different ranges of WBGT for the Dimiceli and Liljegren WBGT datasets compared to Grundstein et al. (2015) when defining the 3 heat risk regions, which are defined using MJJAS 90th percentile of daily maximum WBGT. Further, this suggests that the Oklahoma Mesonet may report lower WBGT risk during the hottest part of the day than the Liljegren WBGT formula would suggest. The standard deviation of the two formulations are in good agreement (Fig. 2.2d). The RMSD between the Liljegren WBGT and Dimiceli WBGT is largest during the winter

(not shown) and overnight (Fig. 2.2c). During the summer daytime hours the RMSD is around 1.8 °F (1.0 °C), while during winter months it may be as high as 3.2 °F (1.8 °C). Nighttime RMSD is consistently near 1.8 °F (1.0 °C) year-round. As the forthcoming results (other than category based analysis) use thresholds based on percentiles, the results shown for the remainder of the paper are using Dimiceli WBGT from ERA5 except where notable differences exist between Dimiceli WBGT and Liljegren WBGT.

2.4 Climatology of WBGT and Risk Categories

2.4.1 Trends in WBGT

To evaluate how the frequency of each category is changing over time, the trend in the number of days with a daily maximum Dimiceli WBGT in each category during the extended summer (May-September; MJJAS) is shown (Fig. 2.3). These trends are calculated by taking the mean of the number of days per year at each grid point with a daily maximum WBGT category across each subdomain (Fig 2.1) and calculating the trend using linear ordinary least squares regression. The extended summer is chosen for this analysis to capture the annual trend without including a large period of time that is overwhelmingly in the no risk category (around 135-140 of the MJJAS days with uniform categories and around 120-130 days per year for regional categories). In general, the northern USGP shows weak, non-significant trends (Fig. 2.3a,d) with almost all risk days in the low risk category at ∼10-20 days per year for uniform categories and ∼20-30 days per year for the regional categories. With regional categories the number of moderate risk days is ∼5-10 per year. In the central USGP the total number of low and moderate risk days increases from ∼25 to ∼35 days per year for low risk and from ∼5 to ∼10 days per year for moderate risk with uniform categories and from ∼30 to ∼40 days per year for low risk and from ∼5 to ∼10 days per year for moderate risk

with regional categories (Fig. 2.3b,e). Correspondingly, the number of no risk days decreases from ∼125 to ∼110 days per year from 1960 to 2020. The number of high and extreme risk days is small but with slight positive significant trends.

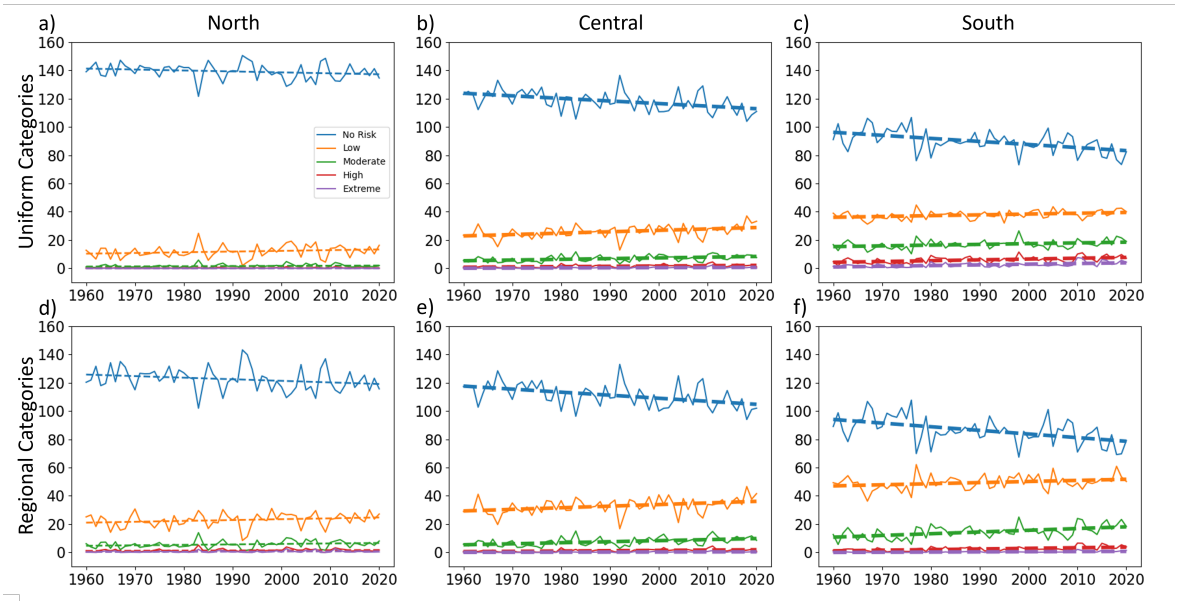

Figure 2.3: Trend in subdomain mean number of MJJAS days with each daily maximum Dimiceli WBGT category for uniform (a-c) and regional (d-f) categories for the northern (a,d), central (b,e), and southern (c,f) USGP. Dashed lines indicate the trend, with trends that are statistically significant at the 95% confidence level in bold

In the southern USGP when using uniform categories both the high and extreme risk categories increase significantly over the 1960-2020 period (Fig. 2.3c). For high risk the annual number of days increases from ∼5 per year in 1960 to ∼10 in 2020. During the same period, extreme risk increases from ∼1 day per year to ∼3 per year. Correspondingly, there is a significant decrease in no risk days, dropping from around 100 days per year to ∼80 days. Low (∼40-50 days per year) and moderate risk (∼20-25 days per year) show statistically significant positive trends as well with uniform categories. For the southern USGP using regional categories the total number of high and extreme risk days are smaller than with uniform categories but still show statistically

significant positive trends. There is a statistically significant increase in the number of moderate risk days, with number of days per year increasing from ∼10 in 1960 to ∼20 by 2020. The number of no risk days decreases from ∼95 to ∼80 days per year over the same period.

Liljegren (Fig. A.1) categories exhibit similar trends to Dimiceli. However, because Liljegren tends to have warmer maximum WBGT, there are fewer no risk days and more days in the other risk categories. No risk days are typically reduced by ∼10-15 per year with those days distributed proportionally to the risk days frequency in the northern USGP, primarily to the low and moderate risk days in the central USGP, and primarily to the high and extreme risk days in the southern USGP. Additionally, the analysis is repeated at the 3 points from Fig. 2.1 which suggests that the southern point, which is near Oklahoma City and within Region 3, has substantially more moderate and high risk days than shown by the regional means (Fig. A.2 and A.3).

Trends in WBGT by day of the year are shown using WBGT at 20 UTC, as this is typically the warmest part of the day across most of the domain. The trends presented in Fig. 2.4 represent the trend in the mean of the 20 UTC WBGT across the entirety of each subdomain calculated via linear ordinary least squares regression. Trends in Dimiceli WBGT are generally positive except during transitional seasons. In fact, during October all three subdomains experienced negative trends during the study period. Across the domain, the largest trends are during the extended cold season of December-March, with trends of up to 1 °F per decade. Warm season trends are typically between 0.2 and 0.4 °F per decade. The positive cold season WBGT trends tend to be the largest in the northern USGP during January and the central USGP in March. Differences in trends between Dimiceli WBGT and Liljegren WBGT are minimal (Fig. A.4).

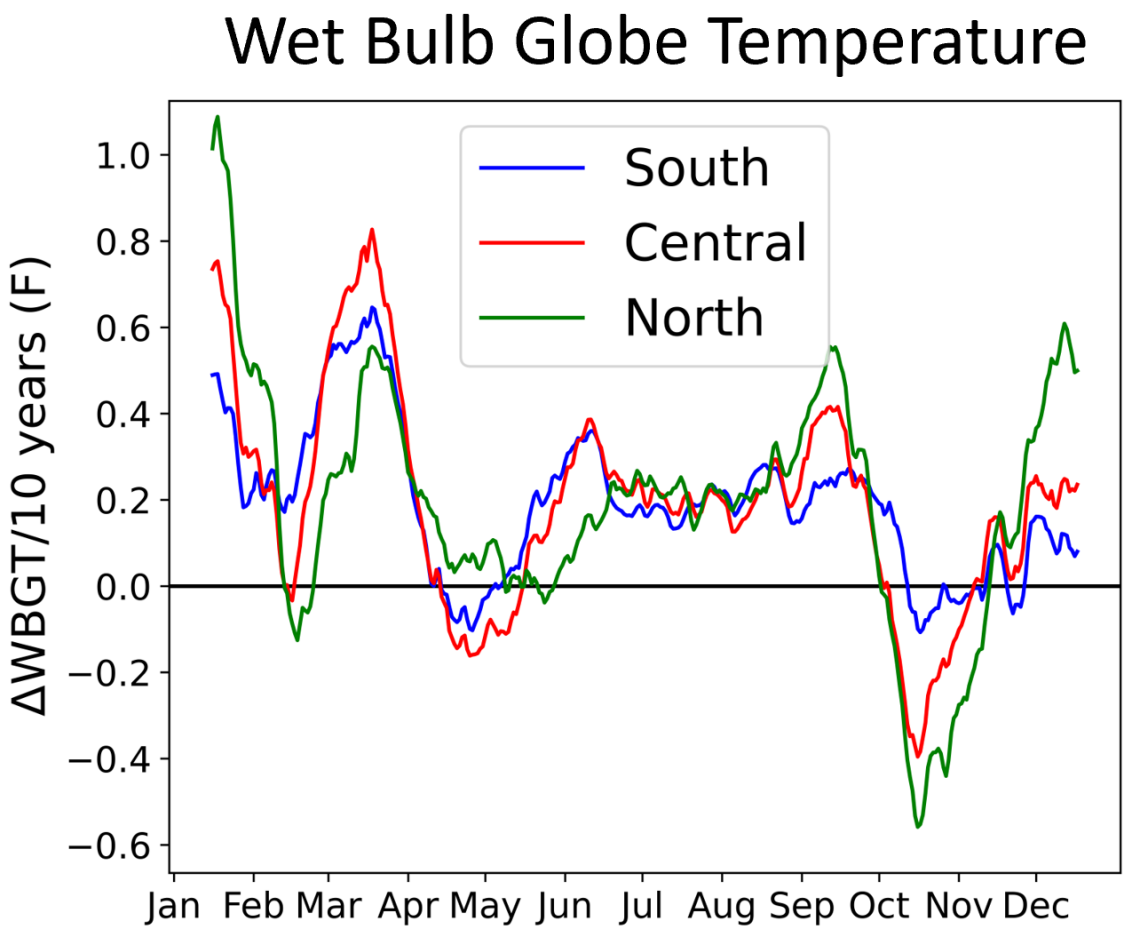

Figure 2.4: Trend in 20 UTC Dimiceli WBGT averaged across each subdomain.

2.4.2 Seasonality of WBGT risk

Figure 2.5a-c shows the distribution of daily maximum Dimiceli WBGT uniform category per day for three representative locations shown in Figure 2.1. As mentioned previously, the category never exceeds low risk outside of April-October (extended warm season), with the southern location having the longest period where low risk or higher regularly occur. The north only exceeds no risk on about 35% of days during the peak in July, with the June-August period generally exceeding no risk >20% of days. Typically at the northern USGP location, when there is a heat risk, it is a low risk, as moderate and high risk only exceed 5% combined for a brief period at the end of July. However, most of the year does not see any days with any heat risk during the study period when using uniform categories. Due to infrequently exceeding the no risk level, individuals in the northern USGP may not be well acclimated to low risk or upper no risk conditions. At the central location, the low risk is the most common daily maximum category during the peak warm season, and as many as 20% of all days reaching moderate risk. At the south location for the peak of the warm season in July and August the most frequent category is moderate, peaking at about 50% of all days, with both high risk and low risk being more frequent than no risk. In fact, no risk is only the maximum category for around 10% of all days in July and August while high risk peaks at just under 20% of days. For the remainder of the extended warm season outside of July and August, low risk is the most frequent category at around 45-60% of days.

Repeating this analysis using the mean over each subdomain results in fewer low risk days in the central USGP regardless of which categorization scheme is used (Fig. A.5). In the southern USGP there are more no risk and low risk days and fewer moderate risk days during the warm season, with low not having a reduced frequency

in July and thus remaining more frequent than moderate risk throughout the warm season.

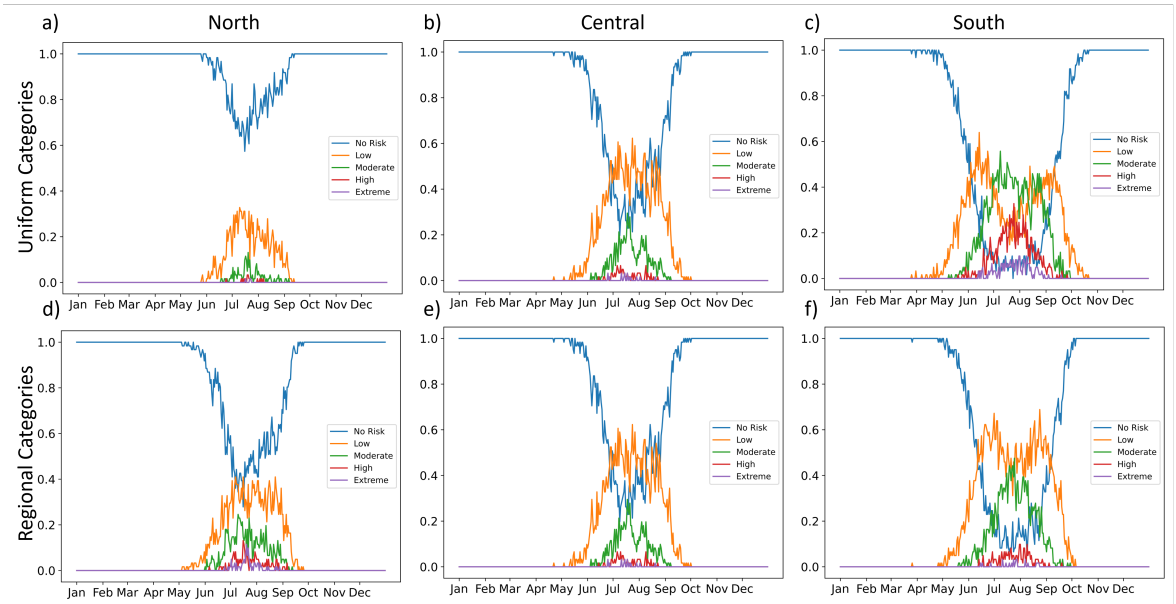

Figure 2.5: Daily maximum Dimiceli WBGT category by relative frequency using a-c) uniform categories, d-f) regional categories, for the a,d) north, b,e) central, and c,f) southern USGP.

Using Liljegren WBGT (Fig. 2.6) increases the amount of days in high and extreme risk, while decreasing the frequency of no risk days in all regions. This is consistent with the higher daytime WBGT found shown in Section 2.3.2. The most clear example is in the South location where extreme risk occurs >20% of all days at the peak in late July and early August (Fig. 2.6c), increasing from under 10% when using Dimiceli WBGT (Fig. 2.5c). A corresponding decrease in low risk days results in each of the moderate and extreme categories becoming more frequent than the Low risk category. At the North location the Liljegren WBGT results in a decrease in no risk days that corresponds with increases in all other categories, however no risk remains the most frequent category for all days. These results show that southern portions of the domain face significant heat risk for much of the summer months. In these conditions, many

outdoor activities should be moved to the morning or evening, especially if they cannot be moved indoors or delayed until conditions improve (Table 2.2).

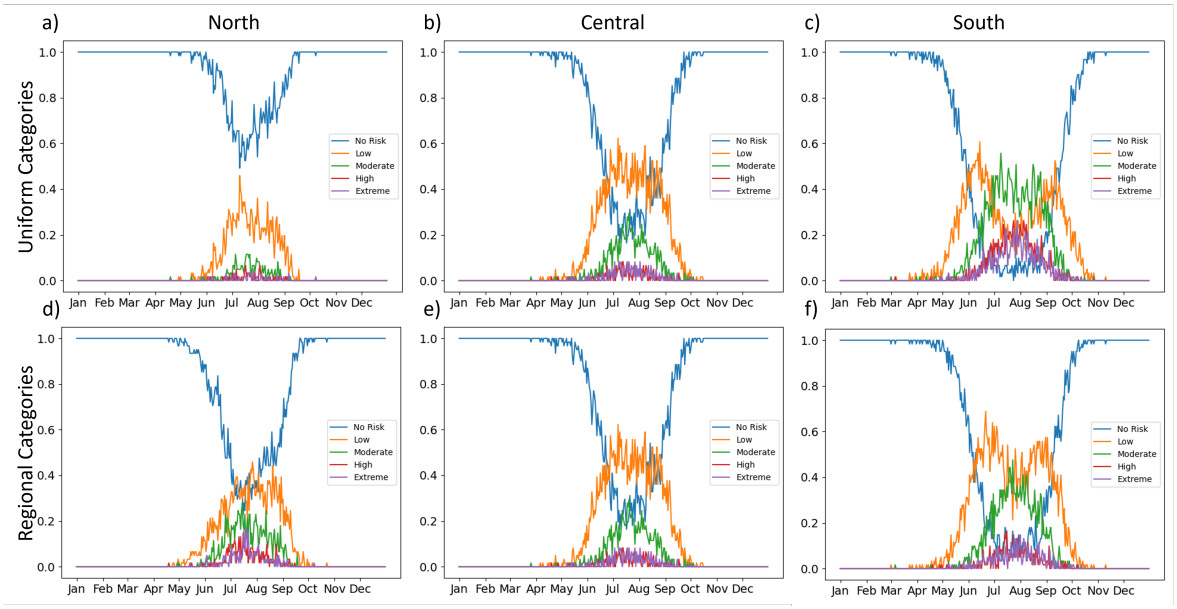

Figure 2.6: Daily maximum Liljegren WBGT category by relative frequency using a-c) uniform categories, d-f) regional categories, for the a,d) north, b,e) central, and c,f) southern USGP.

If regional acclimation is accounted for in the category definitions (i.e. using regional categories), then the differences in the distributions across regions is reduced by design (Figs. 2.5d-f and 2.6d-f). The northern location is in Region 1, the central location is in Region 2, and the southern location is in Region 3 (Fig. 2.1). In the north, no risk is still the most common maximum category, but it is nearly matched by low risk at between 40 and 50% while moderate risk is nearly 20% at peak frequency in July (Fig. 2.5d). The central region is unchanged from the uniform category distribution (Fig. 2.5b and e are identical). The south has a reduced frequency of moderate category days during the warm season, leading to the low risk days being the majority of all days during the duration of the warm season. Moderate risk is still more frequent than no risk during July and August, reaching between 20 and 40%. The regional categories

suggest that southern regions still see higher heat risk categories than northern climates after accounting for regional acclimation, but the difference is less pronounced than for uniform categories. Differences between Liljegren and Dimiceli WBGT using regional categories are consistent with those for uniform categories (Fig. 2.5d-f, 2.6d-f). As with Dimiceli WBGT, analyzing the subdomain mean daily maximum heat risk frequencies fewer low risk and more no risk days in the central USGP while the southern USGP has more no risk and low risk days and fewer moderate, high, and extreme days (Fig. A.6). As the peak of the WBGT warm season is July throughout the domain, the remainder of the climatology in this paper will focus on July.

2.4.3 Diurnal cycle of WBGT

As WBGT undergoes a significant diurnal cycle (Fig. 2.2) and nighttime heat can prevent heat stress recovery, here we examine the diurnal cycle in more detail. Figure 2.7 shows that the lowest values of Dimiceli WBGT occur in the northern USGP and the highest values in the southern USGP, as expected. The southern location peaks at approximately 82 °F with the central and northern USGP at around 78 and 74 °F respectively. The maximum WBGT occurs at approximately 20 UTC in all locations, with the minimum at approximately 10 UTC. Nighttime low WBGTs follow the same relative pattern with WBGTs around 67, 63, and 60 °F for the southern, central and northern points. Liljegren WBGT does not show any notable differences from Dimiceli WBGT (Fig. A.7) aside from the previously shown increase in diurnal range.

One limitation of using either of the risk categories is that the WBGT is always in the no risk category overnight in our domain, which is problematic if one wishes to use low temperature as part of a heat wave definition. This is not a problem when using uncategorized WBGT, but many users of WBGT, including the public, may not

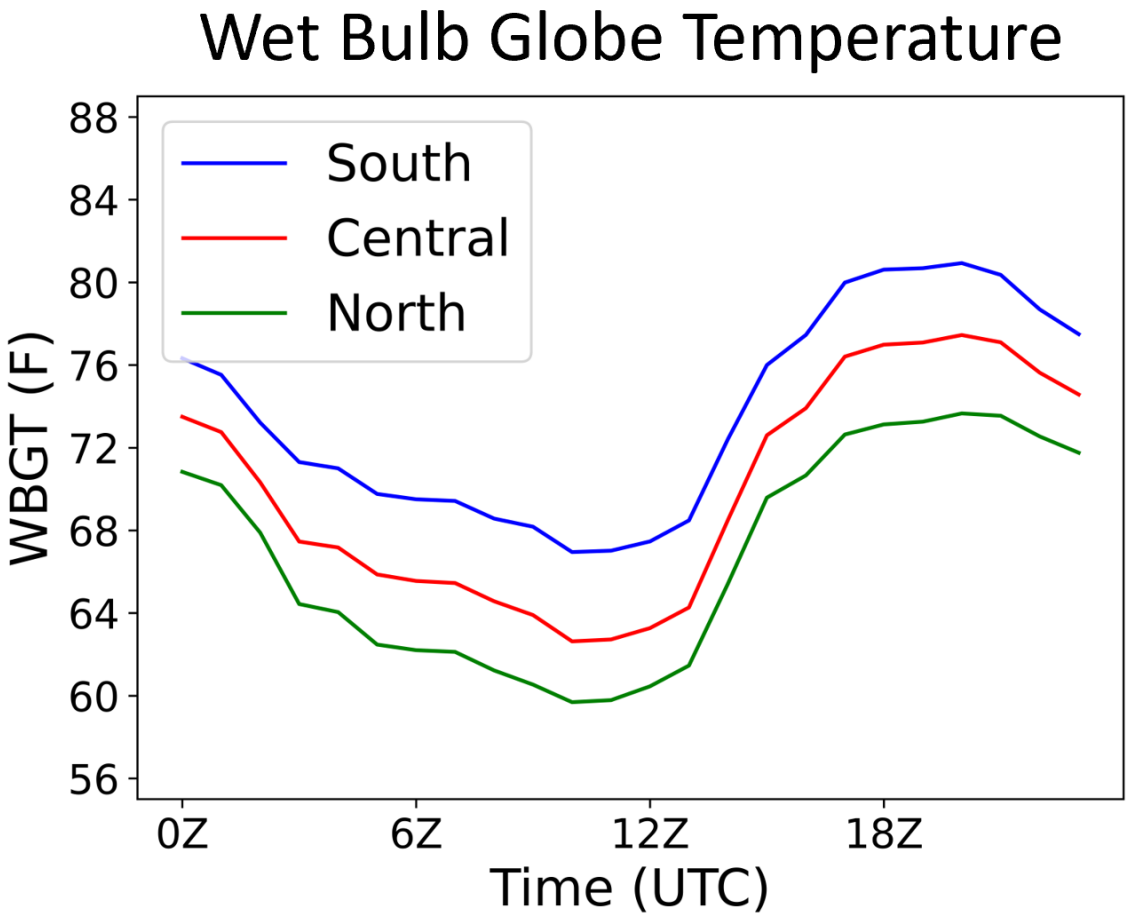

Figure 2.7: July hourly mean of Dimiceli WBGT representing the northern (green), central (red), and southern (blue) USGP subdomains.

be familiar with these values and their context, which is an advantage of the category system.

2.4.4 Distribution of WBGT

To examine the WBGT distribution, the mean and standard deviation of the daily maximum, minimum, and mean WBGT for July are shown (Fig. 2.8). For each the mean WBGT increases to the south and east while the standard deviation increases to the north and east, with standard deviations in the northern portions of the USGP twice those in the southern USGP. Mean daily maximum WBGT is around 70 °F in the northern portions of the USGP while the southeastern portions of the USGP are around 85-90 °F. Minimum WBGTs are around 15 °F below the maximum and mean WBGTs are typically around the midpoint of the Maximum and Minimum WBGT. Liljegren WBGT results in a similar pattern but with a larger diurnal range and noisier standard deviations (Fig. A.8).

Further, histograms of July daily maximum, minimum, and mean Dimiceli WBGT are shown for one location in each subdomain (Fig. 2.9). Along with the lower peak in the northern USGP, the distribution of daily maximum WBGT is wider than the southern locations. In all regions, the distribution is skewed to the left. This suggests that exceptionally cool daily maximum WBGT values are more common than exceptionally hot daily maximum WBGT values. The Liljegren maximum WBGT distributions are skewed slightly warmer, typically with longer warm tails but the same mode (Fig. A.9).

Histograms of the daily minimum Dimiceli WBGT are shown in Figure 2.9d-f. Dimiceli WBGT has a peak in the 55-65 °F range in the Northern USGP, with the central peak at 65-70 °F and the southern USGP peaking at the 70-75 °F bin. As with

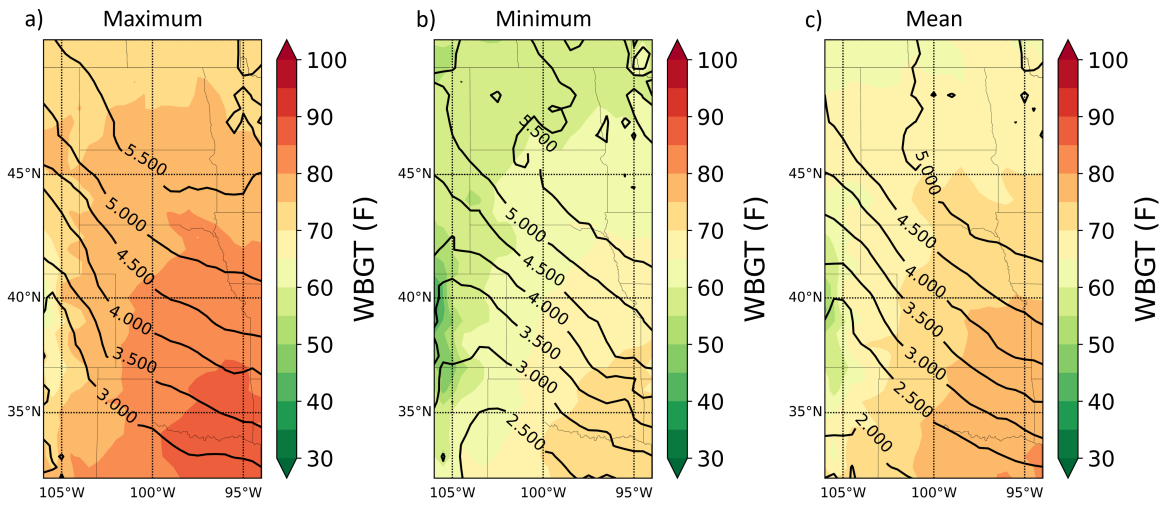

Figure 2.8: Mean (filled contours) and Standard Deviation (contours) of July daily a) maximum, b) minimum, and c) mean Dimiceli WBGT.

the maximum Dimiceli WBGT, the distribution is wider with lower frequency at the peak (<40%) in the northern USGP and a narrower distribution and higher frequency at the peak of the distribution (∼70%) in the southern USGP. The distributions tend to be left skewed in the central and southern USGP, but near-normal in the northern USGP. This suggests that while most days are near the higher part of the distribution, it is more common to have an exceptionally cool low than an exceptionally warm low. The Liljegren WBGT (not shown) is typically shifted to the left of Dimiceli WBGT (Fig. 2.9d-f), consistent with the observation that Liljegren WBGT is cooler at night than Dimiceli WBGT (Fig. 2.2c).

Histograms of daily mean Dimiceli WBGT are shown in Figure 2.9g-i. In the northern USGP, the peak is in the 65-70 °F bin with a frequency near 40%, the central USGP peaks in the 70-75 °F bin at around 50% of all days, and the southern USGP peaks at the 75-80 °F bin peaking around 70%. Correspondingly, the distribution in the northern USGP tend to be wider than those in the southern USGP. The Liljegren WBGT formulation produces nearly identical results and is not shown.

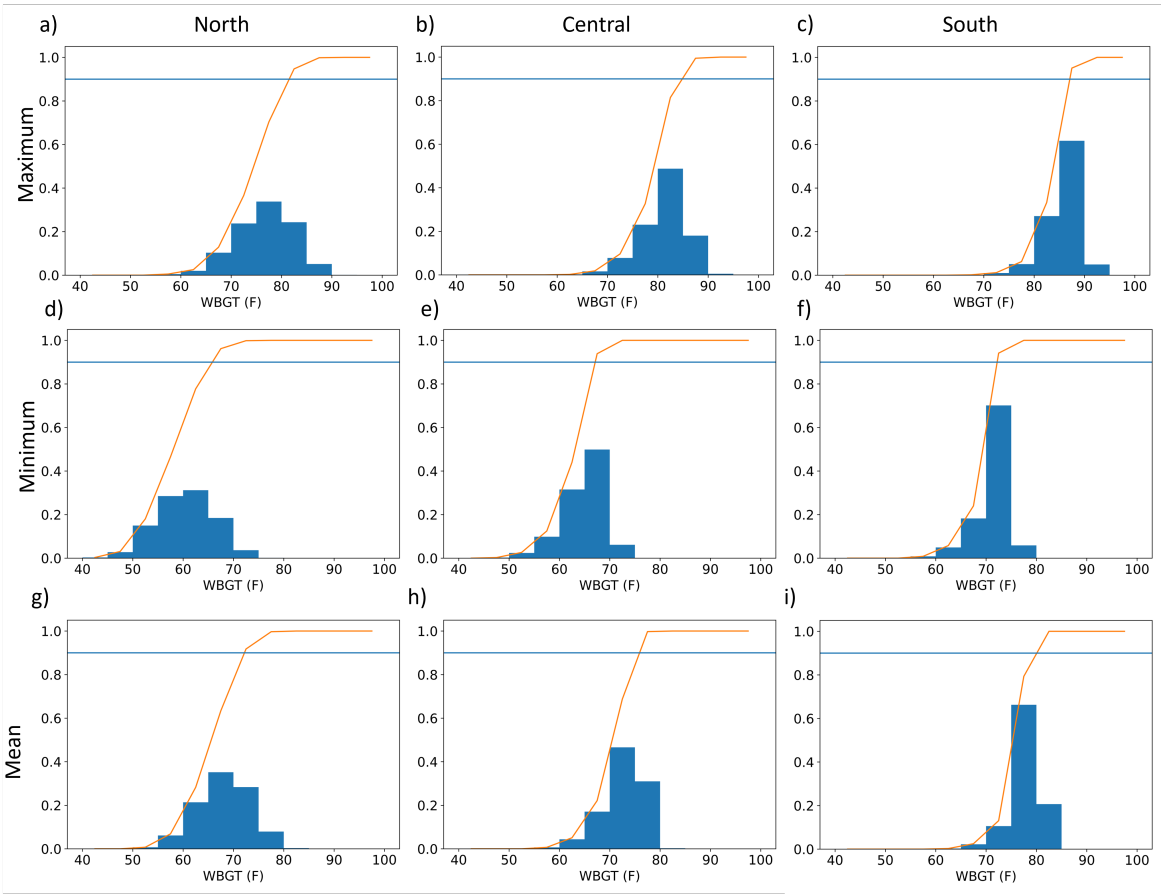

Figure 2.9: Distribution of July daily a-c) maximum, d-f) minimum, and g-i) mean Dimiceli WBGT for the a,d,g) Northern, b,e,h) Central, and c,f,i) Southern USGP. Cumulative distribution function in orange with the 90th percentile indicated by the blue horizontal line.

2.5 Heat Wave Climatology

As discussed in Section 2.2.5, three heat wave definitions are presented here. The definitions are based on 1) daily maximum WBGT, 2) daily minimum WBGT, 3) daily mean WBGT. These three definitions are chosen as each have been shown to be important for heat stress and recovery (Robinson 2001; Hajat et al. 2002; Anderson and Bell 2011; Smith et al. 2013; Nissan et al. 2017). Heat wave thresholds are based on the 90th percentile of the centered 31-day period of the appropriate metric across the 61-year period of the dataset. The threshold must be met for 2 consecutive days to be classified as a heat wave, and must fail to be met for 2 consecutive days to terminate a heat wave.

Heat wave definitions based on categories were investigated, but are not included here for several reasons. First, the number of WBGT categories is small, so categories containing the 90th percentile often contain significantly more than 10% of the data and thus leads to varying effective thresholds across the domain, even with regionally varying categories. Second, minimum WBGT is universally in the no risk category, making heat waves using this definition non-existent. Third, it is challenging, and not very meaningful, to define mean WBGT category. Even when doing so, as overnight is in the no-risk category it only provides information about daytime conditions, thus negating much of the reason for using mean WBGT. Additionally, only definitions based on local percentiles are presented as thresholds that do not vary spatially have the additional problem of failing to account for acclimation.

2.5.1 Heat Wave Thresholds

The 90th percentile thresholds are shown for Dimiceli and Liljegren maximum WBGT (Fig. 2.10a,b), minimum Dimiceli WBGT (Fig. 2.10c), and mean Dimiceli WBGT

(Fig. 2.10d). Minimum Liljegren WBGT is shown in Figure A.10a. These values consider the period of July 1-31, which is the threshold applied to the July 16 WBGT. The 90th percentile of maximum, minumum, and mean WBGT all exhibit both a north-south and west-east (dominant) gradient for both Dimiceli and Liljegren WBGT. This is due to both the north-south gradient in temperature, as well as the east to west slope in elevation and west to east moisture gradients. Maximum (minimum) Liljegren WBGT has slightly higher (lower) values of WBGT due to the larger diurnal variation as shown in section 2.3.2. Mean WBGT is similar for both Liljegren and Dimiceli WBGT (Fig. A.10b).

2.5.2 Heat Wave Characteristics

To see the behavior of heat waves in the USGP, several heat wave characteristics are presented. The first characteristic is the annual number of heat wave days. When using the maximum WBGT heat wave definition there is a local minimum of heat wave days centered over eastern Colorado and western Kansas (∼20-24 days) with higher numbers (∼26-30 days) occurring in northern and eastern parts of the domain (Fig 2.11a-c). For the definition using minimum WBGT, the gradient is from northwest to southeast. A local maximum associated with a strong gradient occurs in northeast Texas decreasing across Oklahoma and western Texas before decreasing in magnitude over the rest of the domain. Overall, much of the north and western portions of the domain see ∼22-26 heat wave days each year, while much of Oklahoma and North Texas see greater than 28 days per year. For the mean WBGT definition, the number of heat wave days is largest in the south decreasing gradually to the north. As a result, most regions see the most heat wave days (∼25-30) under the mean WBGT definition.

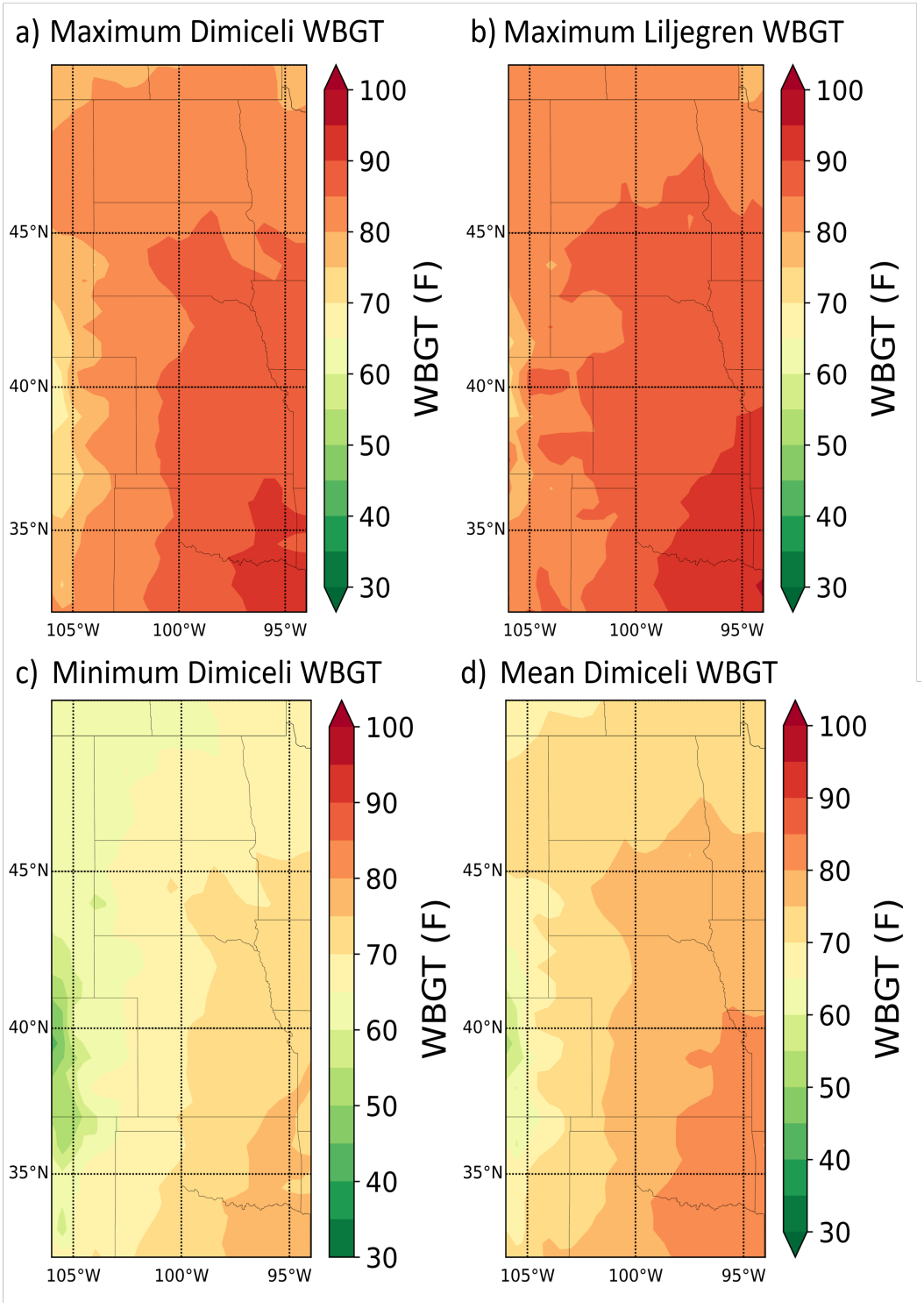

Figure 2.10: July 16 31-day centered 90th percentile a) maximum Dimiceli WBGT, b) maximum Liljegren WBGT, c) minimum Dimiceli WBGT, and d) mean Dimiceli WBGT.

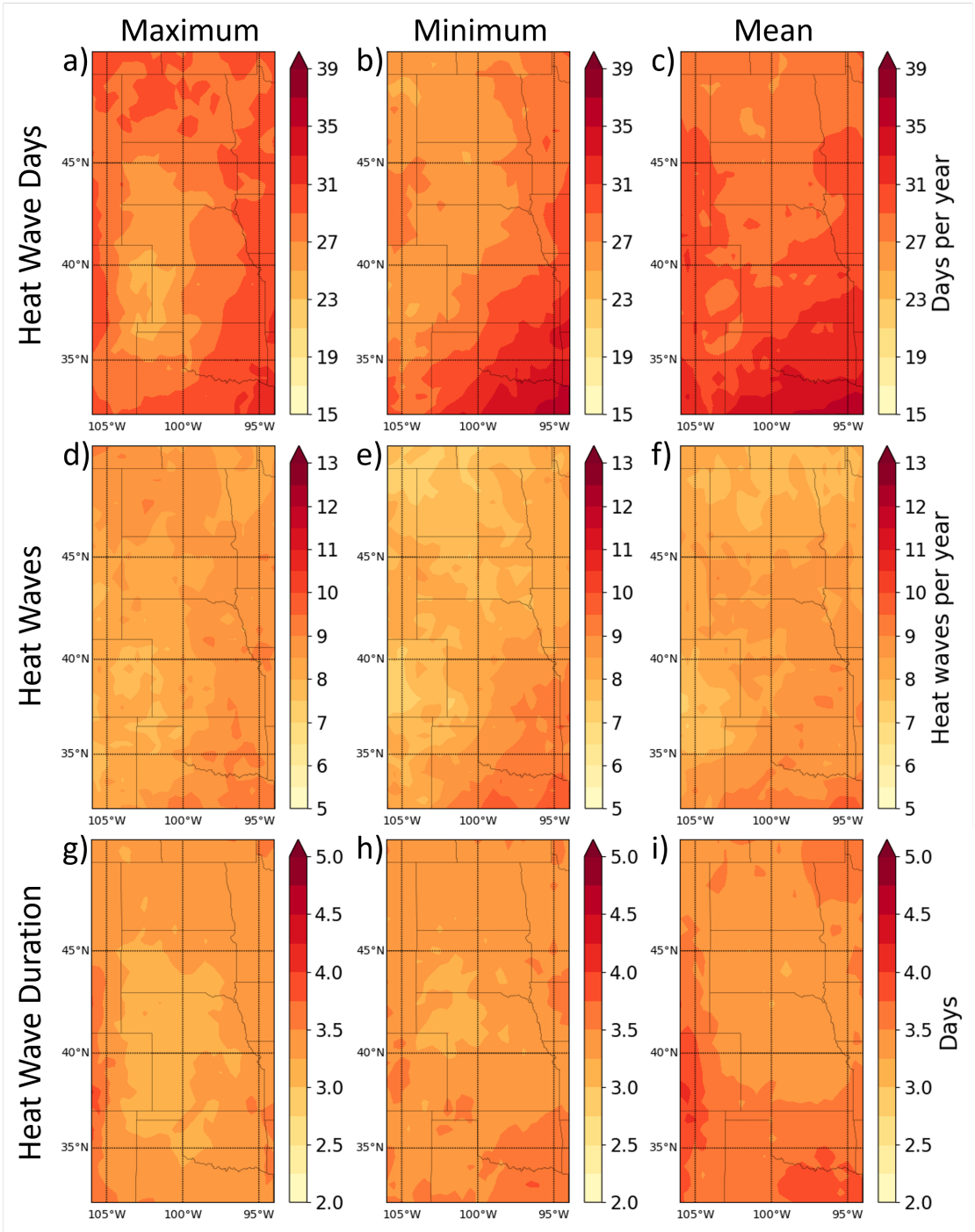

Figure 2.11: Mean a-c) heat wave days per year, d-e) number of heat waves per year, g-i) number of days per heat wave using a heat wave definition based on a,d,g) maximum WBGT, b,e,h) minimum WBGT, and c,f,i) mean WBGT.

The second characteristic is the average number of heat waves per year (Fig. 2.11d-f). For all three definitions, there is a local maximum in northeast Texas. Because this is coupled with a local maximum in heat wave days and heat wave duration (Fig. 2.11g-h), this suggests that this local maximum is driven by a persistent phenomenon. Some possible explanations may be moisture from evapotranspiration from the local forests, relative ease of moisture transport from the Gulf of Mexico due to proximity, or fewer cold fronts to break up heat. For maximum WBGT, the local maximum extends into much of eastern Oklahoma and eastern Kansas, with another local maximum in western North Dakota. Each of these local maxima are around 10 heat waves per year. The minimum frequency is in eastern Colorado, western Kansas, and into the Texas and Oklahoma panhandles, at around 7-8 heat waves per year. For the minimum WBGT heat waves, there is a stronger north to south gradient with around 8 heat waves per year in the north increasing to around 11 in the south. However, as with the maximum WBGT heat waves, there is a higher amount in Oklahoma and eastern Kansas than in regions to the west. The mean WBGT heat wave definition leads to a similar north to south gradient but it is more gradual than with minimum WBGT.

The third characteristic presented is heat wave duration, or the average number of days in a heat wave. Heat wave duration (Fig. 2.11g-i) based on maximum WBGT is typically slightly shorter than other definitions, with a broad area in the west-central USGP between 3-3.25 days with much of the rest of the region being 3.25-3.5 days. While the duration is similar using minimum WBGT the region of 3-3.25 days is confined largely to southwest South Dakota and western Nebraska, with much of the rest of the domain being in the 3.25-3.5 range. Parts of the southeastern and far eastern domain exceed 3.5 days. When using mean WBGT most of the domain is around 3.25-3.5 days per heat wave, with the southern USGP exceeding 3.5 days per heat wave.

Liljegren WBGT produces fewer maximum WBGT heat waves than Dimiceli WBGT across the USGP region, generally reducing the number of heat wave days (Fig. 2.12a versus Fig. 2.11a). Correspondingly, the number of heat waves per year is reduced by about 2 days per year when using maximum Liljegren WBGT (Fig. 2.12b). For minimum and mean WBGT there are no notable differences between Liljegren and Dimiceli WBGT heat waves (Fig. A.11 and Fig. A.12).

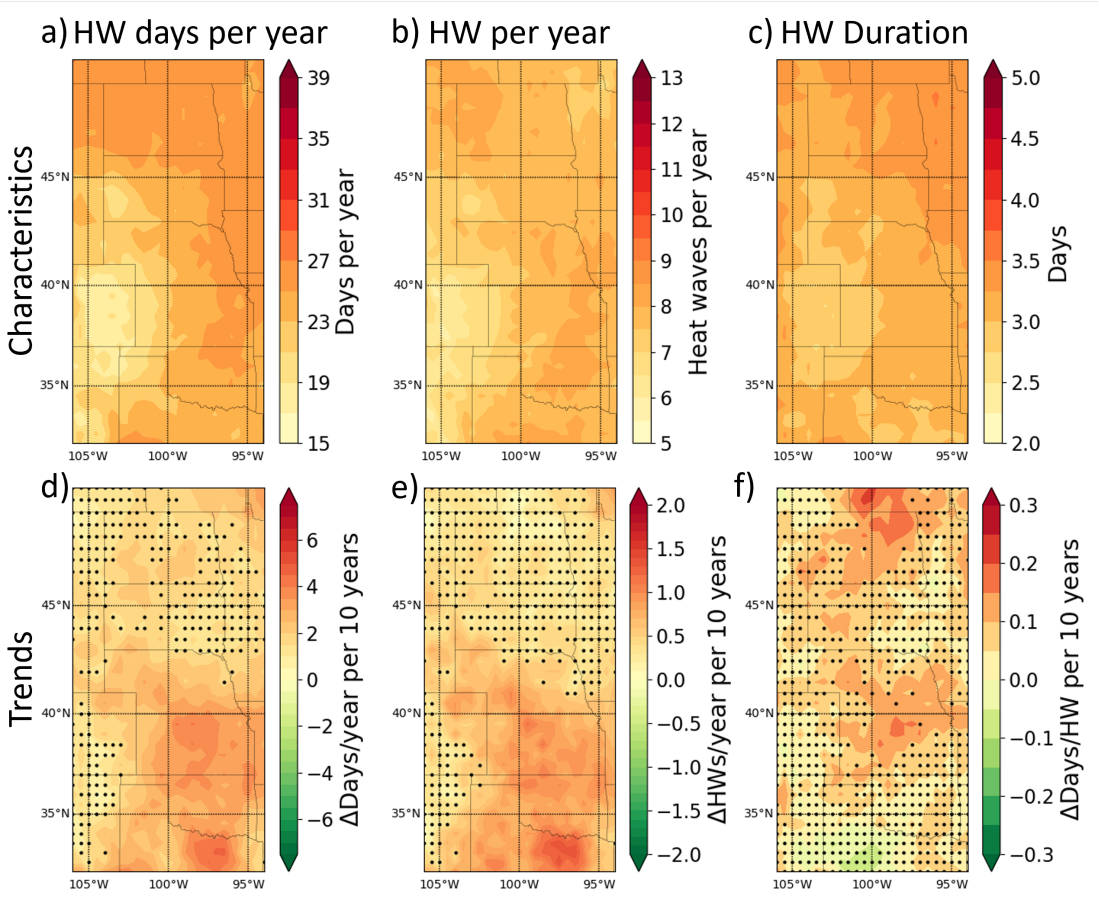

Figure 2.12: Mean a) heat wave days per year, b) number of heat waves per year, c) number of days per heat wave, and trend in d) heat wave days per year, e) number of heat waves per year, and f) number of days per heat wave. All panels use a heat wave definition based on daily maximum Lijegren WBGT. Black dots indicate trends that are not statistically significant at the 95% confidence level.

2.5.3 Heat Wave Characteristics Trends

Trends in the number of heat wave days, annual number of heat waves, and number of days per heat wave are calculated using linear ordinary least squares regression over the period 1960-2020. Generally, the number of WBGT heat waves and heat wave days have increased throughout the domain (Fig. 2.13a-f), consistent with the broad increases observed in WBGT shown previously. The strongest trends in heat wave days are in minimum and mean, with the strongest trends in the south and the total number of heat wave days increasing by more than 15% of the mean value each decade on average over the study period. Trends in heat waves show much of the same pattern as number of heat wave days. The largest increases in heat waves increases occur in the southern portions of the domain. Further, minimum and mean WBGT heat waves are increasing at rates faster than those when defined by maximum WBGT. Peak rates of increase exceed 1.5 additional heat waves per decade, or nearly 20% of the mean per decade in some locations.

Heat wave duration trends are generally small, with trends in the maximum and minimum WBGT heat waves mostly insignificant and near 0. However, in regions of eastern Kansas, Nebraska, and the Dakotas the length of heat waves is increasing >0.05 days per heat wave per decade in the maximum WBGT definition. In south-eastern portions of the domain, heat wave duration for the mean WBGT heat waves is increasing between 0.05 and 0.1 additional day per heat wave per decade. Further, southern Manitoba experiences >0.1 additional day per heat wave per decade across all definitions.

Trends in heatwaves using Liljegren WBGT (Fig. 2.12d-f) are similar to those when using Dimiceli WBGT, but with a lower magnitude, reflecting the reduction in the number of heat waves and heat wave days each year.

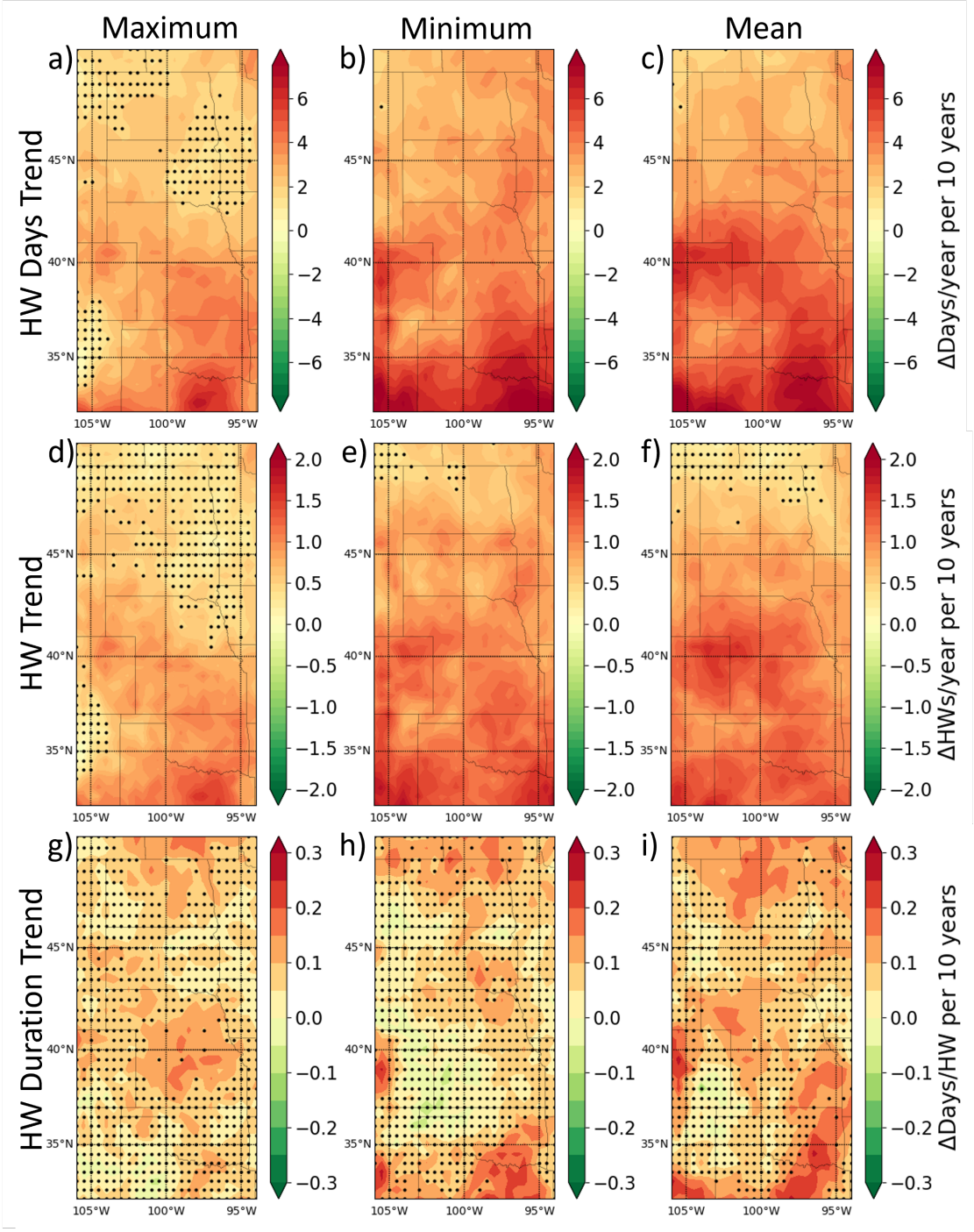

Figure 2.13: Trend in mean a-c) heat wave days per year, d-f) number of heat waves per year, g-i) number of days per heat wave using a heat wave definition based on a,d,g) maximum WBGT, b,e,h) minimum WBGT, and c,f,i) mean WBGT. Black dots indicate trends that are not statistically significant at the 95% confidence level.

Generally, heat wave days are increasing regardless of the heat wave definition used. However, the number of heat waves is increasing fastest in the minimum and mean WBGT definitions. For most regions, the increase in heat wave days is primarily due to an increase in the total number of heat waves. However, using the mean WBGT definition, the duration of heat waves is also increasing in some regions, compounding with the number of heat waves to lead to a large increase in the number of heat wave days.

2.6 Discussion

WBGT is typically calculated from standard observations and several methods exist to estimate it. Here we show notable differences in USGP WBGT characteristics depending on which of two commonly used methods of calculating WBGT are used - Dimiceli (Dimiceli et al. 2011) and Liljegren (Liljegren et al. 2008). The mean WBGT does not change significantly depending on which method is used. The Liljegren WBGT is shown to have a larger diurnal cycle than the Dimiceli WBGT with Liljegren WBGT about 1 °F higher for the daily maximum WBGT and 2 °F lower for the daily minimum WBGT. As a result, Liljegren WBGT reaches higher risk categories more frequently during the warm season compared to Dimiceli WBGT throughout the USGP. Conversely, as Liljegren WBGT has lower WBGT overnight, this suggests better opportunities for heat stress recovery than those suggested by Dimiceli WBGT. Patel et al. (2013) found that Liljegren WBGT performed better at calculating the daily maximum WBGT than WBGT calculated from other methods (e.g. Matthew et al. 2001), but with a larger RMSD at higher WBGT values. However, Rennie et al. (2021) found that Dimiceli WBGT performs comparably to Liljegren WBGT on average, with regional variability in which method correlates better with observed WBGT.

In this study we found that during the daytime the Dimiceli WBGT was around +1 °F warmer and Liljegren +2 °F warmer when using ERA5 compared to the Oklahoma Mesonet (Fig. 2.2), which uses Dimiceli WBGT calculated from observations. The Dimicelli WBGT from ERA5 reproduces the Oklahoma Mesonet WBGT distribution more closely during the warmest part of the day. However, this is likely the result of using the same model for both. Ahn et al. (2022) shows that Liljegren WBGT has a slight positive bias across the USGP at a majority of stations in Nebraska and Kansas (our central USGP subdomain) compared to in situ observations. Additionally, Ahn et al. (2024) shows that in climate regions common to the USGP, Liljegren WBGT calculated from ERA5 tends to overestimate WBGT more than with other input sources and more than some other models with ERA5 input. However, because Ahn et al. (2024) does not examine Dimiceli WBGT it is uncertain if the ERA5 input is the source of the differences in Liljegren WBGT and Dimiceli WBGT in our study. Each of these studies are limited by the small number of in situ WBGT observations available, which can bias results toward those found in certain environmental conditions. We do not assess the accuracy of either method compared to directly observed WBGT and from this work and prior studies mentioned, it is unclear which of Liljegren WBGT and Dimiceli WBGT perform better in the USGP. Users of modeled WBGT are cautioned to understand which methodology is used and to use caution when making comparisons between WBGT from different datasets or methodologies.

A relative threshold at the 90th percentile is used for each of the daily minimum, daily maximum, and daily mean WBGT to define heat waves to account for local acclimation, which is in the typical range of other heat wave studies (Smith et al. 2013). The mean and minimum WBGT heat wave definitions tend to have more heat waves and heat wave days than the maximum WBGT heat wave definition. Further, the mean WBGT heat wave definition produces heat waves of longer duration, particularly

in the southern USGP than the other definitions. Because mean WBGT is an average of 24 observations throughout the day compared to a single extreme value in minimum or maximum WBGT, which may reduce the day to day variability and prevent this variability from being the factor that ends a heat wave early or delays the start of a heat wave, or even prevent the onset of a heat wave altogether.

Over the 61-year study period, the total number of heat waves and heat wave days increased. Using the maximum WBGT heat wave definition the increase is mostly occurring in the southern and central portions of the USGP. Perkins (2015) notes in their review of heat wave literature that there is a "warming hole" over portions of North America in the second half of the 20th century. While the exact location changes based on methodology and choice of dataset, the warming hole often extends into the USGP and may be driven by the Interdecadal Pacific Oscillation (Meehl et al. 2012). As such, these regions could see stronger increases in the future.

The mean and minimum WBGT heat wave definitions result in larger increases in heat waves and heat wave days over the entire domain compared to the maximum WBGT heat wave definition. Studies have shown that minimum temperature and heat waves based on minimum temperature are increasing faster than their maximum temperature equivalents (Perkins 2015; Oswald 2018). As WBGT is strongly correlated with air temperature this rapid increase in minimum air temperatures is likely the culprit for the similar behaviour in minimum WBGT heat waves. Additionally, since the mean WBGT incorporates the minimum WBGT into its calculation it explains why the mean WBGT heat waves see similar trends to the minimum WBGT heat waves. This is particularly concerning given the evidence that overnight low temperatures are critical for recovery from heat stress (Robinson 2001; Hajat et al. 2002; Nissan et al. 2017). Seasonally, WBGT is increasing faster during the winter and early spring

months, with the largest trends in the northern USGP. Studies have shown that northern latitudes are warming faster than the midlatitudes and even faster in the winter than the summer (Bekryaev et al. 2010; Collins et al. 2013). While winter heat risks are currently zero, if these trends continue it could lead to more days in which outdoor activities are disrupted outside of the current warm season.

2.7 Conclusions

This study calculates a climatology of WBGT and the associated heat waves for the USGP using ERA5 reanalysis using the WBGT formulation from Dimiceli et al. (2011), which is used in several operational settings. WBGT calculated from ERA5 is shown to be able to accurately represent the WBGT calculated from Oklahoma Mesonet observations to within 2 °F and well represents the overall statistical distribution of WBGT. Further, the Dimiceli WBGT is compared to the Liljegren et al. (2008) formulation of WBGT. The Liljegren WBGT is found to have a larger diurnal cycle than the Dimiceli WBGT, leading to higher WBGT during peak heating ($\sim +1°F$) but lower WBGT overnight than the Dimiceli WBGT ($\sim -2°F$). As a result, Liljegren WBGT has slightly more frequent occurrences of the high and extreme heat risk categories than Dimiceli WBGT in the southern USGP, and of the low and moderate categories in the northern and central USGP. Otherwise, the differences are small. In the southern USGP the most frequent categories during the warm season are moderate, however high and extreme categories occur more frequently than in other parts of the plains, where it is uncommon to experience a risk higher than moderate.

WBGT trends are strongest in the winter. However, as these WBGT values are below the low risk threshold, the cold season category trends are universally 0. During the warm season the southern regions of the domain are both warmer and the WBGT

and risk category is increasing faster than in northern portions of the region. During the warm season, the no risk category is decreasing in frequency in the central and southern USGP as the low and moderate regions increase in frequency in the central USGP while the high and extreme categories become as much as three times more frequent over the 61-year study period in the southern USGP.

Overall, there tend to be more heat waves in the southern part of the domain than in the northern part, however the maximum WBGT heat wave definition tends to produce a more west to east gradient than north to south. The most heat wave days and longest heat waves tend to occur when using a mean WBGT heat wave definition. While using minimum and mean Liljegren WBGT to define heat waves produces similar results to using Dimiceli WBGT, the maximum WBGT heat wave definition does have some notable differences. Specifically, the Liljegren WBGT defintion produces fewer heat waves than Dimiceli WBGT, with a shorter average duration as well. This suggests that there could be some additional variability in the Liljegren WBGT that may be breaking up longer strings of extreme heat that may be damped in the Dimiceli WBGT. The trends in heat waves and heat wave days are generally positive, with the strongest occurring in the southern USGP and with definitions based on the minimum and mean WBGT. However, the heat wave length does not show statistically significant trends using the minimum WBGT definition, and only some localized positive trends appear in maximum and mean WBGT based heat waves.

The information presented in this study may be useful to those planning outdoor work to schedule the work more efficiently. Further, the trends presented suggest that the risk of heat stress has been increasing, making it more important than ever to understand the risks and their timing.

Chapter 3

Predictability of Environments Associated with Wet Bulb Globe Temperature Heat Waves

3.1 Background

Heat Waves can have strong impacts on humans through a variety of direct and indirect impacts as discussed in Chapter 1. While Chapter 2 discusses the climatology and characteristics of heat waves, it is important to understand the drivers of heat waves and temperature extremes in order to maximize the ability to mitigate risks associated with extreme heat. Forecasts on S2S timescales can help preparation towards mitigating the risks associated with extreme heat. S2S timescales refer to the period between 2 weeks and 2 months, between the periods where weather models are able to provide skillful predictions (<2 weeks) and seasonal prediction (3-6 months) (e.g. Vitart et al. 2017). Sources of predictability on S2S time scales typically include phenomenon such as sea surface temperatures, the MJO, and soil moisture (e.g. Vitart et al. 2015; Vitart et al. 2017; Vitart and Robertson 2018 and citations within).

Heat waves typically occur under high pressure and clear skies with light winds, with longer heat waves typically associated with blocking highs, however shorter heat waves may also be associated with Rossby waves (Perkins 2015). It has also been shown that below average rainfall the preceding 6-8 months may greatly exacerbate the risk of extreme heat (Hoerling et al. 2013). Low soil moisture leads to a positive

feedback loop between the soil and the air through sensible heat flux, intensifying both heating of the air and further drying soil (Perkins 2015). Another known predictor for heat waves is wave number 5 anomalies, which often precede heat waves in the USGP by 15-20 days (Teng et al. 2013).

Ideally, we would be able to directly forecast WBGT through the use of dynamical models, such as those in the S2S Project database (Vitart et al. 2017). However, due to limitations of the data it is difficult to get a meaningful value for WBGT. For example, solar radiation is accumulated over a 24 hour period, wind speed is at 0 UTC, and there is a single value for daily maximum, minimum, and for some model minimum temperature. This value temperature value and the wind speed value will likely not occur at the same time, and the solar radiation will vary throughout the day. Compounded by the nonlinearity of WBGT, any attempt to directly calculate WBGT from this data will not be meaningful. Because of this, this study will instead evaluate WBGT heat wave rates through several known predictors of heat and heat waves such as ENSO and MJO, as well as through the use of atmospheric regimes.

Atmospheric regimes represent the predominant patterns in the atmosphere and have previously been used in similar studies in the USGP to predict temperature anomalies (e.g. Lee et al. 2023; Millin et al. 2022), with Millin et al. (2022) using atmospheric regimes to predict cold snaps in the USGP, and Lee et al. (2023) showed temperature anomalies associated with . Similar studies have used atmospheric regimes to predict changes in wintertime minimum temperature extremes over the Iberian Peninsula (Ortizbeviá et al. 2011) and have been used extensively in Europe to predict wind energy, air quality, and temperature extremes (Ortizbeviá et al. 2011; Van Der Wiel et al. 2019; Garrido-Perez et al. 2020; García-Herrera et al. 2022). Generally in the aforementioned studies, positive heat anomalies are associated with high pressure,

while negative anomalies with low pressure, consistent with earlier studies summarized in Perkins (2015).

Teleconnections from a variety of tropical circulations can have significant impacts on heat in the USGP. The SE Asian monsoon has been shown to be a source of heat wave predictability. During summers with a strong monsoon the latent heat energy released induces an equivalent barotropic wave train in the subtropical jet stream, which sets up a blocking pattern similar to composites during heat waves over the Central United States (Lopez et al. 2019).

The El Niño-Southern Oscillation (ENSO) is another such factor. On average during El Niño, the southeast and south-central US are colder than normal, and the northern US is warmer, while the opposite is true for La Niña (Ropelewski and Halpert 1986; Kenyon and Hegerl 2008; Koster et al. 2009; Hoerling et al. 2013, 2014; Seager et al. 2014; Lopez et al. 2019). For example, the 2011 Texas heat wave is largely attributable to La Niña (Hoerling et al. 2014). Heat waves in Eastern Europe and the south central United States are also more frequent during summers with a decaying El Niño or developing La Niña than with a decaying La Niña or developing El Niño (Behera et al. 2013; Loikith and Broccoli 2014; Luo and Lau 2020).

The MJO also impacts temperature in North America. Lee and Grotjahn (2019) found that in the California Central Valley, heat waves often occurred within 14 days after MJO phase pairs 8-1 and 2-3, particularly when the heat wave was not preceded by a heat wave in northwestern North America. Over eastern North America, the influence on temperatures by the MJO are strongest when a PNA-like pattern is in place (Schreck et al. 2013). Further, Schreck et al. (2013) showed positive temperature anomalies over the USGP 6-10 days following MJO phase 6 with the anomalies dampened during PNA-like patterns. Similarly, MJO phase 3 produced positive temperature

anomalies over the northern USGP into the Midwestern US during neutral PNA patterns. Further, Moon et al. (2011) showed that in the Pacific Northwest temperature anomalies during MJO phases are modulated by the phase of ENSO, with the region experiencing opposing impacts during MJO phase 3 depending on whether ENSO is positive or negative.

Generally, the above sources of predictability are for air temperature. However, as discussed in Chapter 1, there are other factors that can impact human perception of heat, which WBGT is better suited for. Understanding of the predictability of extreme heat from a WBGT perspective allows for heat wave forecasts that are more targeted toward human impacts. While not every event will have high confidence, certain situations may present a "forecast of opportunity" where the specific situation presents a higher than normal confidence in the forecast. By having advanced notice of heat waves, individuals planning outdoor work can benefit by being able to adjust schedules in advance, emergency responders can prepare in advance and have resources in place in time, and medical facilities can increase staffing and supplies.

3.2 Data and Methods

3.2.1 Domain

This study focuses on the USGP, defined for the purposes of this study as the area bounded by 106 °W and 94 °W longitude and 32 °N and 50 °N, as shown in Fig. 2.1. The domain is divided into three subdomains, the northern, central, and southern USGP, with the Northern USGP defined as areas north of 43 °N, the Southern USGP areas along and south of 37 °N, and the central USGP in between. There is a location shown for each of the three regions, with the north and central locations located at the center of their subdomain, and the south location located near Norman, OK. These

locations will be used to represent each subdomain when discussing time series of heat wave rates and distributions of heat wave types.

3.2.2 WBGT calculation

This study uses the gridded WBGT dataset from Chapter 2 which is calibrated to the USGP using WBGT from the Oklahoma Mesonet. The dataset contains WBGT for the years 1960 through 2020 for a total of 61 years and is at 0.5 ° x 0.5 ° resolution. WBGT is calculated as a weighted average of dry bulb air temperature (T_{air}), black globe temperature (T_{bg}), and natural wet bulb temperature (T_{nwb}) as described in eq. (2.1) (Yaglou and Minard 1957). T_{bg} is calculated following Dimiceli et al. (2011), and T_{nwb} follows the internal equations from the Oklahoma Mesonet as described in section 2.2.3. The Dimiceli T_{bg} is a linearized version of that described in Hunter and Minyard (1999) modified to include a convective heat transfer coefficient that is a function of solar irradiance and solar zenith angle. The T_{nwb} is calculated by first calculating the wet bulb temperature iteratively as described in section 2.2.3 which in turn follows the Oklahoma Mesonet and the National Weather Service, then applying the adjustment found in Hunter and Minyard (1999). The input data for the WBGT is from the ERA5 reanalysis, using 2-meter wind speed (from 10-meter wind speed which is extrapolated to 2-meter as described in section 2.2.3), 2-meter temperature, 2-meter dewpoint temperature, surface pressure, and mean surface downward short-wave radiation flux.

3.2.3 ERA5

ERA5 500 mb geopotential (Hersbach et al. 2018) from 1960-2020 is used in this study to train a K-Means clustering model to define North American atmospheric regimes

as described in section 3.2.7. Additionally 2-meter air temperature, 2-meter dewpoint temperature, 10-meter U and V wind, surface pressure, and mean surface downward short-wave radiation flux were used in the calculation of the WBGT dataset in Chapter 2. ERA5 data is interpolated to 0.5 ° x 0.5 ° resolution at the time of download via an option in the API due to storage limitations.

3.2.4 ECMWF S2S model

This study uses reforecast data from the European Center for Medium Range Weather Forecasting (ECMWF) Subseasonal-to-Seasonal (S2S) model, accessed through the the S2S Project database (Vitart et al. 2017). The ECMWF S2S model contains 1 control member and 10 perturbed members for a total of 11 members. The model output is on a 1.5 ° x 1.5 ° grid, and has daily output through lead time 45 days. Forecasts are initialized 52 times per year from 1996 through 2014, with forecasts initialized starting on January 1 and every 7 days after through the end of February, and on March 3 then continuing every 7 days after through the end of December. During non-leap years this results in a 6 day gap between the last run in February and the first run in March, and a 9 day gap between the last run of each year and the first run of the following year. This study uses 500 mb geopotential height which is used to classify each day in the model output as described in section 3.2.7.

3.2.5 Heat wave definition

Following section 2.2.5 the daily threshold for heat waves is defined by taking the mean WBGT each day, and calculating the 90th percentile of the rolling centered 31-day by 61-year window. A heat wave is considered to have occurred when this threshold is exceeded for two consecutive days and continues until two consecutive days are below

this threshold with the two days below the threshold at the end not considered to be part of the heat wave.

3.2.6 Heat Wave Types

Heat wave days are divided into different types based on the mean temperature and humidity characteristics of the heat wave day relative to the climatology of heat wave days that occur during the same month. Specifically, for each month the climatological mean and standard deviation of mean temperature ($\bar{T_{air}}$) and mean dewpoint temperature ($\bar{T_d}$) of heat wave days only is computed, and then each heat wave days' $\bar{T_{air}}$ and $\bar{T_d}$ is standardized. A neutral day is defined as any where the distance of the point (standardized $\bar{T_{air}}$, standardized $\bar{T_d}$) from (0,0) <= 0.5. For all other heat wave days, the day is classified as hot-humid if both $\bar{T_{air}}$ and $\bar{T_d}$ are >0, warm-humid if $\bar{T_{air}}$ is <0 and $\bar{T_d}$ is >0, hot-dry if $\bar{T_{air}}$ is >0 and $\bar{T_d}$ is <0, and warm-dry if both $\bar{T_{air}}$ and $\bar{T_d}$ are <0. The distribution of heat wave types is shown in Fig. 3.2 for the three locations marked on 2.1 as examples.

3.2.7 500 mb North American Atmospheric Regimes

K-Means clustering, an unsupervised machine learning method, is used to classify each day into one of 9 regimes. The model is trained using the detrended and standardized 00 UTC 500 mb geopotential from the ERA5 reanalysis at 1.5 ° x 1.5 ° resolution to match that of the ECMWF model output. A domain between 15 °N to 90 °N and from 180 °W to 30 °W is used for this model. The model was tested at various resolutions to ensure that the solution is robust. The same regimes were produced regardless of the resolution with only a small number of days being classified into a different regime for each resolution. As this behaviour is also seen when training the model on the same

data at the same resolution multiple times there is no reason to believe the coarser resolution used in this study impacts the results significantly. While most studies retain 4 or 5 regimes over North America (Lee et al. 2019, 2023; Millin et al. 2022), this study will retain 9 total regimes as it was found that inclusion of the additional regimes increases heat wave predictability in the USGP for robust dynamical reasons compared to retaining only 4 or 5 regimes (See section 3.3.2).

The regimes produced are shown in Fig. 3.1, where the regimes are assigned numbers 0-8, with no null regime. Regime 0 corresponds to the Arctic High (Lee et al. 2019; Millin et al. 2022) or Greenland High (Lee et al. 2023) from previous studies. Regime 1 shows a tripole with positive geopotential anomalies over the eastern Pacific and the US west coast as well as in the western Atlantic, with a negative geopotential anomaly over the Arctic. Regime 2 corresponds the Pacific Trough regime (Lee et al. 2019, 2023; Millin et al. 2022). Regime 3 corresponds to the Alaskan Ridge from those same studies. Regime 4 has a strong negative geopotential anomaly over the tropics with a weak anomalous trough over the western US and weak ridges over the north Pacific and eastern Canada. Regimes 5, 6, and 7 are all Rossby wave trains across the domain, where Regime 5 locates a positive geopotential anomaly over the Pacific and eastern North America, and negative geopotential anomalies over western North America and the central Atlantic and corresponds to the Arctic Low (Lee et al. 2019; Millin et al. 2022) and Pacific Ridge (Lee et al. 2023) regime. Regime 6 resembles Regime 5 shifted 1/4 phase westward, putting a positive geopotential anomaly over the western and central United States. Regime 7 further shifts the Rossby wave train 1/4 phase westward, corresponding to the West Coast Ridge from Millin et al. (2022), and roughly inverting the pattern from Regime 5. Regime 8 is then a strong positive geopotential anomaly across the tropics with a weak positive anomaly over central

North America and weak negative anomalies over Alaska and far northeastern North America, which is roughly the inverse pattern of Regime 4.

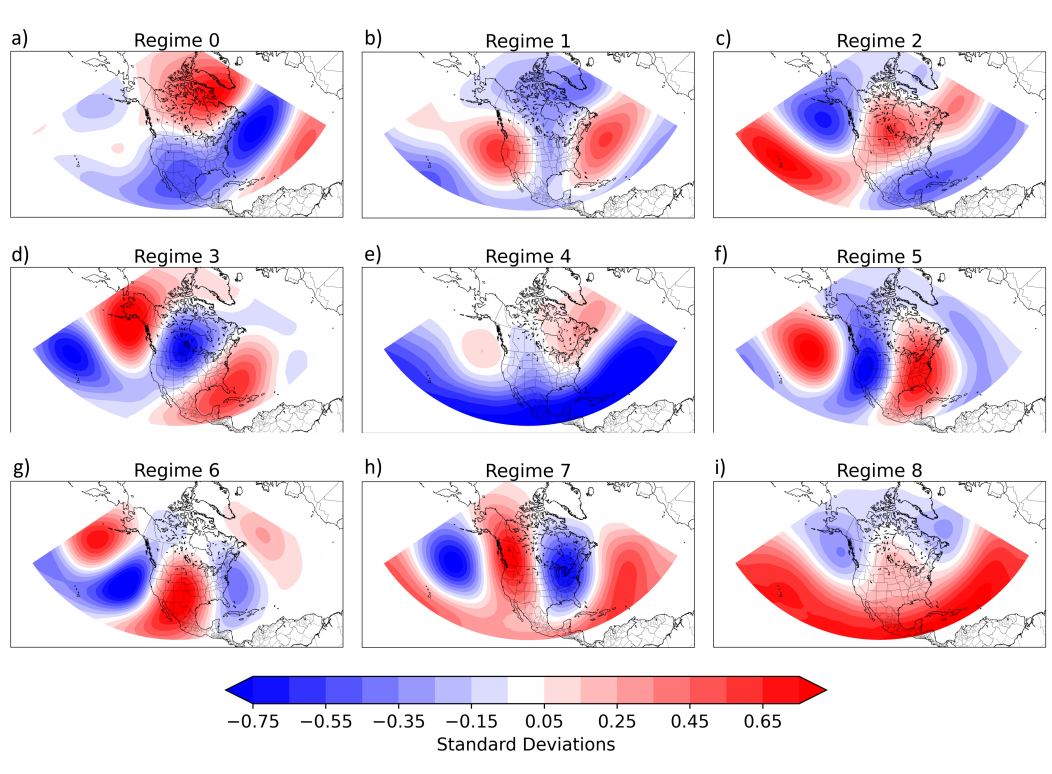

Figure 3.1: 500 mb geopotential standardized anomalies for each regime from K-Means clustering.

3.2.8 El Niño Southern Oscillation and Madden-Julian Oscillation

Data for ENSO is based on the monthly Niño3.4 (Barnston et al. 1997) index which is acquired from the NOAA Physical Sciences Laboratory at https://psl.noaa.gov/gcos_wgsp/Timeseries/Nino34/. Niño3.4 is an average of sea surface temperature perturbations between from 5 °N-5° and 170 °w-120 °W perturbations

across the equatorial Pacific Ocean, averaged over a 5 month period. This study classifies all days in a month as El Niño-like conditions if the Niño3.4 index is > 0.5 for the month, La Niña-like conditions if the Niño3.4 index if < -0.5, and neutral if it is between -0.5 and 0.5. For simplicity, the El Niño-like and La Niña-like will be referred to as El Niño and La Niña throughout.

The Madden-Julian Oscillation (MJO) is an oscillation in tropical convection over the Indian and Pacific Oceans (Madden and Julian 1971, 1972). The MJO is divided into 8 phases using the Real-time Multivariate MJO (RMM) index, which takes the first and second principal components of the combined 850 and 200 hPa zonal winds and the outgoing longwave radiation and calculates the magnitude of each, which is then mapable to into polar coordinates, where the angle represents the phase, and the magnitude is the strength. In this study if the strength is < 1, the phase is classified as neutral. RMM index data was downloaded from the Australian Bureau of Meteorology at http://www.bom.gov.au/climate/mjo/.

3.2.9 Statistical Significance

Statistical significance is assessed using a Monte Carlo resampling technique. Each analysis is repeated 5000 times with random sampling without replacement. For most cases the a random subset equal in size to the number of days that the heat wave rate is defined as the number of days in the population where a heat wave occurs divided by the total number of days in the population, is calculated from is selected from the set of all days, and the heat wave rate is calculated for the random subset. Heat wave rate is defined as the number of days in the population where a heat wave occurs divided by the total number of days in the population. When comparing the rate of a heat wave type within a specific regime, a subset of all days equal to the number of days the regime is selected and a the rates of each regime is recorded. For comparing the

seasonality of a heat wave rates within regimes, days are only sampled from the pool of days corresponding to the specific season to compare the heat wave rate. For each of these analyses the observed value is compared to the distribution of the 5000 randomly sampled values, and is considered different from the baseline value if the percentile rank of the observation is outside of the interval $[\alpha/2, 100 - \alpha/2]$ where alpha is 5, indicating confidence at the 95% level.

3.3 Results

3.3.1 Heat Wave Types

Because many heat wave studies in the USGP only evaluate temperature based heat waves, this study defines several heat wave types to identify which factors drive extreme heat in different heat waves. Heat waves that are of warm-humid in particular may be overlooked when using just a temperature based heat wave definition, as these heat waves by definition have lower air temperatures, and thus demonstrate where an index like WBGT or a humid-heat index may provide an advantage over temperature alone. Heat wave types are defined as described in section 3.2.6, based on the standardized anomalies of temperature and dewpoint relative to the monthly climatology of other heat wave days. Figure 3.2 shows the distribution of heat wave days by the standardized daily maximum air temperature, dewpoint, and season at the three locations shown in Fig. 2.1. At the southern and central locations the JJA heat wave distribution tends to have a strong negative correlation between temperature and dewpoint, leading to warm-humid and hot-dry heat waves being the most common (Fig 3.2g,k). At the northern location temperature and dewpoint are still negatively correlated, but not nearly as much as the southern and central locations for JJA (Fig. 3.2c). Generally DJF, MAM,

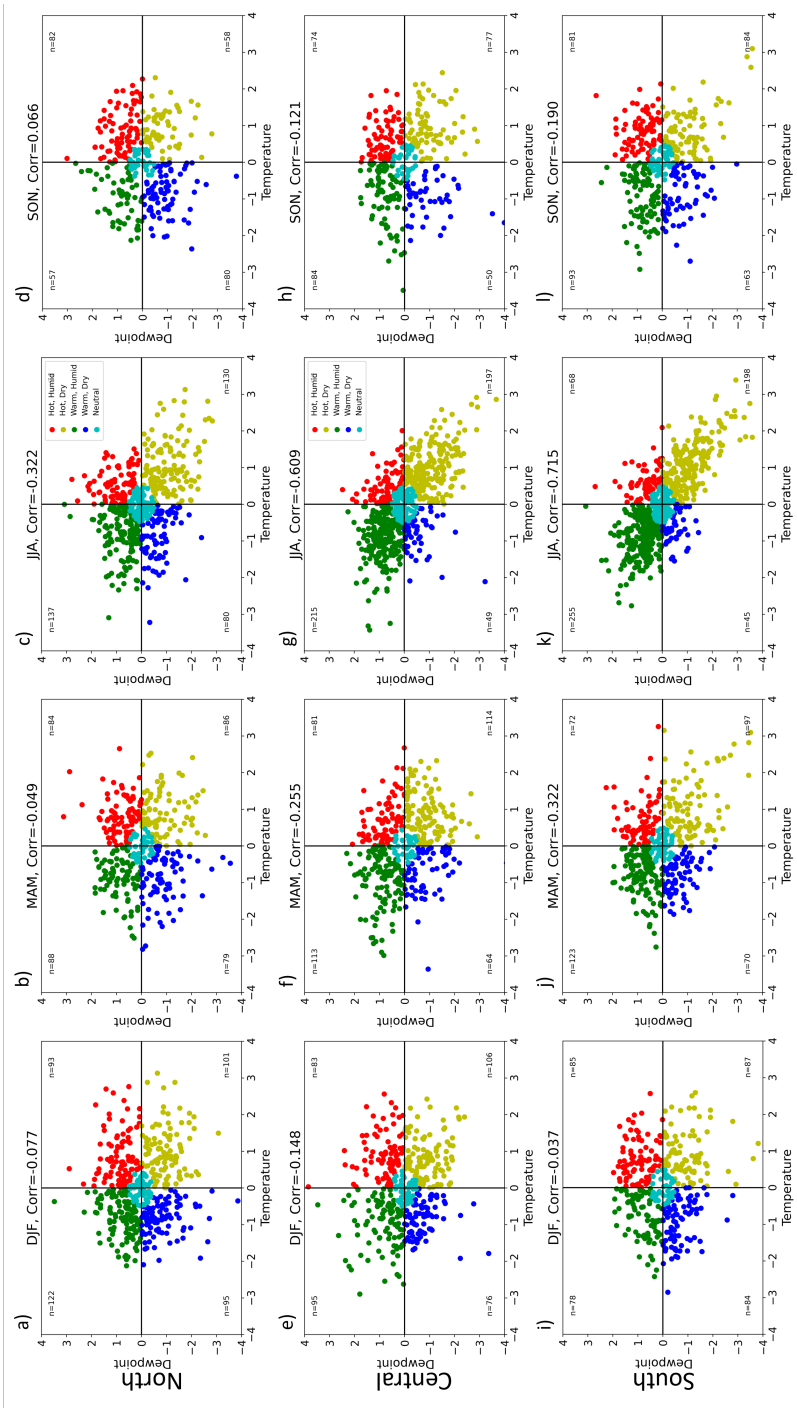

Figure 3.2: Scatter plot of standardized temperature and dewpoint temperature with colors indicating heat wave type for a-d) the Northern, e-h), Central and i-l) Southern USGP locations for a,d,i) DJF, b,e,j) MAM, c,f,k) JJA, and d,h,l) SON.

and JJA all show negative correlation which is not surprising given that humid air takes more energy to heat due to the specific heat capacity of water being larger than that of dry air (Fig. 3.2). During SON the correlations are much weaker and slightly positive, except that the southern location remains slightly negatively correlated (Fig. 3.2l). Overall, this suggests that outside of the JJA season, particularly further north in the USGP, that heat waves are more evenly distributed between types than they are in JJA and further south in the USGP, where hot-dry and warm-humid are the most common types.

3.3.2 Heat Wave Rates and Seasonality

Breaking down the heat wave frequency by regime zero days after the occurrence of a regime (Lag 0) shows that at the southern location (Fig. 3.3a-c), heat waves occur most frequently during regimes 5 and 6 with heat wave rates around 20% and 14% respectively, and at about 12% and 15% in the Central USGP. Heat wave rate is defined as the number of days in the population where a heat wave occurs divided by the total number of days in the population. Both of these regimes place positive geopotential anomalies over the southern and central USGP suggestive of anomalous southerly surface winds, which often bring warm air advection (Fig. 3.1f,g). Regime 5 tends to be more conducive to warm-humid heat waves while regime 6 tends to be associated with hot-dry heat waves. As Regime 5 is further east, it is anomalously advecting humid air from the Gulf of Mexico, while Regime 6 is further west and the anomalous advection is from over land, leading to the advection of hot, dry air.

In the Northern and Central USGP Regime 2 (Fig. 3.1c) is also conducive to heat waves. In the Northern USGP Regime 2 slightly favors the hot-humid heat waves, while in the central USGP Regime 2 favors the hot-dry and warm-humid types.

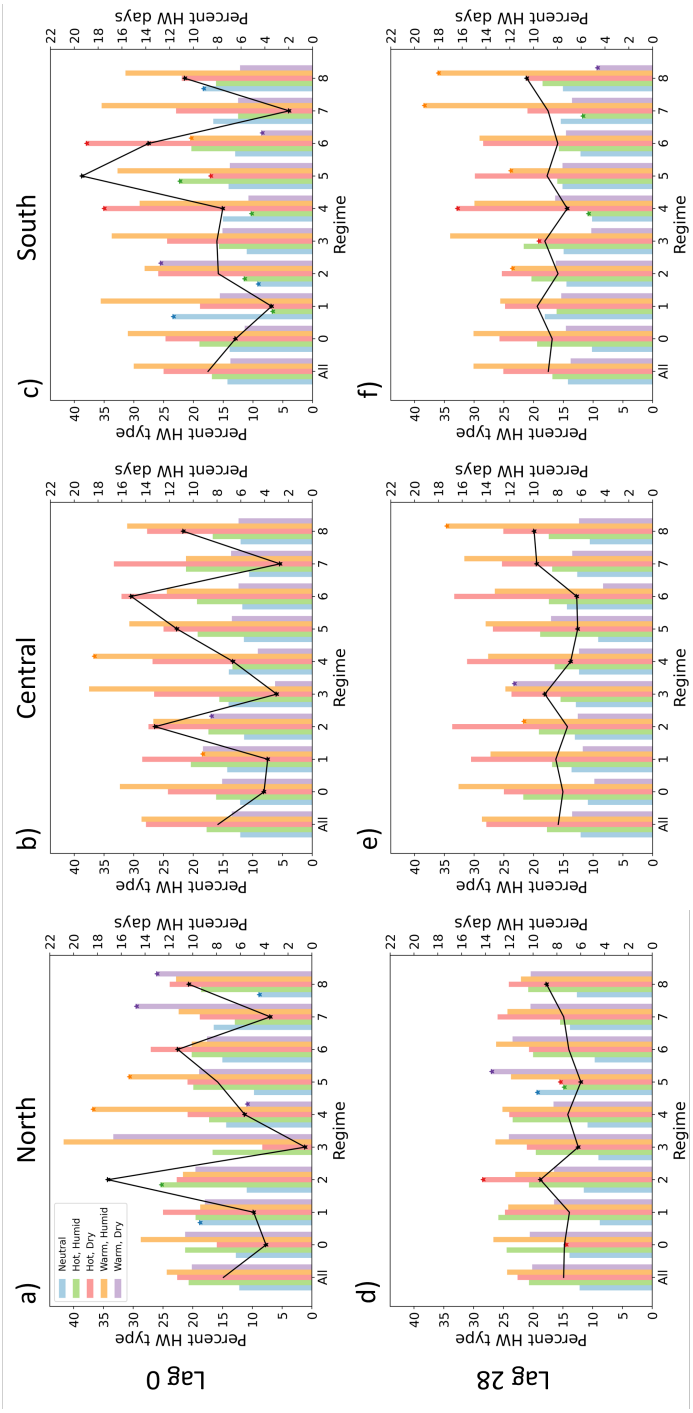

Figure 3.3: Black line: Heat wave rates for the indicated regime. Bars: distribution of heat wave types given a heat wave occurred in the specified regime. Stars indicate statistically significant results relative to all categories. Heat wave rates and percent HW type at at a,b,c) 0, and d,e,f) 28 days following the occurance of a regime for the a,d) Northern, b,e) Central, c,f) and Southern USGP locations.

Suppressed heat wave rates are associated with regimes 1 and 7 (Fig. 3.1b,h) across the USGP at 4% and 2-3% respectively in the Southern and Central USGP, and 4-5% for each in the Northern USGP (Fig. 3.3b,c). Additionally, heat wave rates in the Northern and Central USGP are around 4% for Regime 0 (Fig. 3.1a). Both regimes 1 and 7 put the southern USGP under negative geopotential anomalies in patterns that suggest anomalous surface advection of cool air from the north. Regimes 5,6,7 are primarily Rossby wave trains at different phases over North America, but their placement results in differing impacts for a given location depending on the Regime.

As an example at S2S lead times, 28 days following the occurrence of a regime (Fig. 3.3d-f) the only regimes that suggest heat wave rates that are different at the 95% confidence level from the heat wave rate for all regimes (Baseline rate) in the Southern USGP are regimes 4 and 8. Both regimes have weak 500 mb geopotential anomalies over the USGP, however, both have strong anomalies over the tropical latitudes, suggesting that the tropics may be a source of predictability at this lead time. In the Central USGP Regimes 4, 5, and 6 are associated with reduced heat wave rates, while Regimes 3, 7, and 8 are associated with increased heat wave rates at day 28. Regimes 2 and 8 are associated with day 28 increased heat wave rates and Regimes 3 and 5 are associated with reduced heat wave rates in the Northern USGP. Each of these are only small deviations from the baseline heat wave rate, so while these values are statistically significant it is unlikely that this information will be useful for forecasting heat wave rates at S2S lead times.

To help identify the source any variations in heat wave rates for each regime, the regimes and heat wave rates are further broken down by season. Because heat waves may occur at different rates during different seasons within the same regime, and regimes may occur at different rates across seasons, it is possible that an apparent

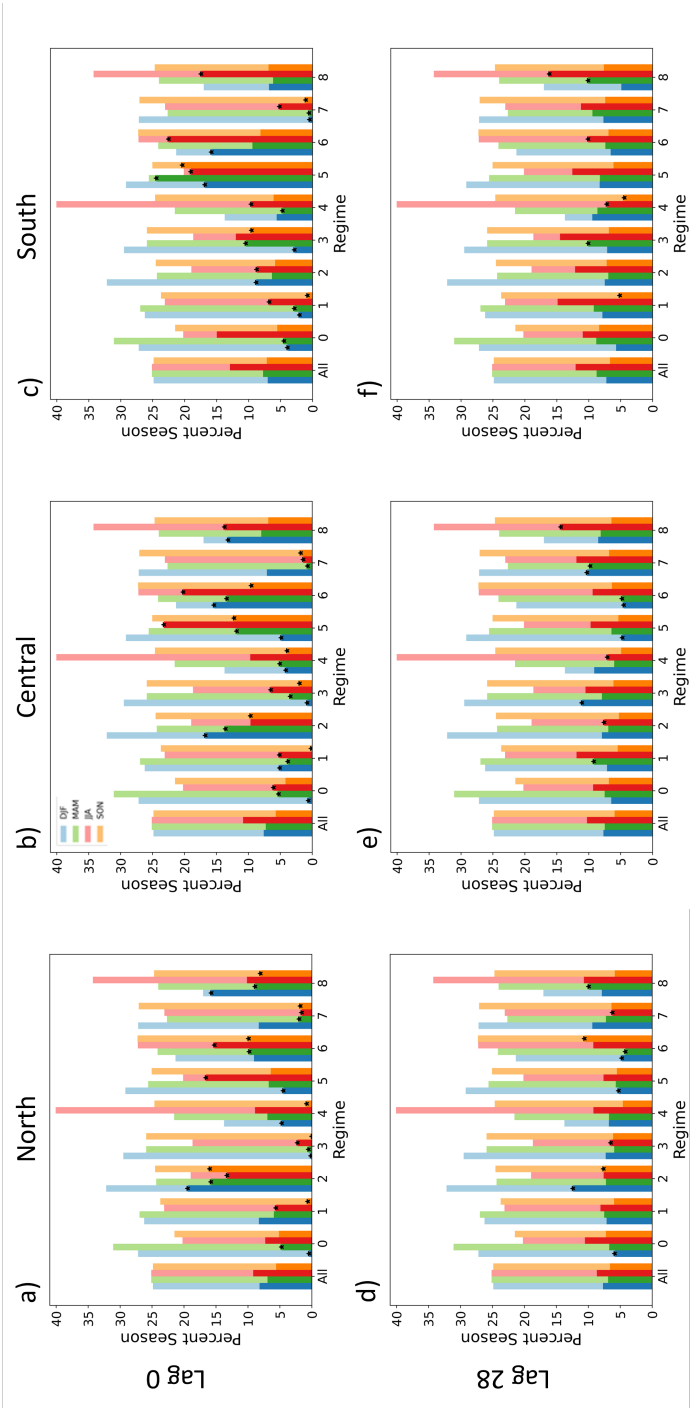

Figure 3.4: Light Bars: Percent of days within the indicated regime that occur during the specified season. Dark bars: percent of days within the indicated regime and season that are heat wave days. Stars indicate statistically significant differences from the same season for all regimes.

anomaly in heat wave rates in a regime could be due to the the regime being more or less frequent in certain seasons. Additionally it is possible the increase may only occur in a portion of the year. Regime 5 occurs slightly more frequently during the winter than the average regime, while slightly less often during the summer (Fig 3.4c). However, at lag 0 in the Southern USGP enhanced heat wave activity occurs during all seasons for Regime 5. Regime 6, however, only shows enhanced heat wave activity during DJF and JJA and occurs more frequently in JJA and SON. Regimes 1 and 7 occur similarly across all seasons with Regime 1 being more common during DJF and MAM, while regime 7 is more common in SON and DJF. Conversely, Regimes 4 and 8 occur much more frequently than other seasons and compared to other regimes during the summer, with nearly 40% and 35% of all days in each regime occurring during JJA respectively. In fact, JJA is the month where the anomalous frequency of heat waves is primarily occurring for both regimes (although for regime 4 SON is also suppressed). In the Central USGP at lag 0 Regime 6 is largely associated with enhanced heat wave rates while Regime 2 is enhanced outside of JJA, while regimes 1 and 3 are suppressed for all seasons (Fig. 3.4b). In the northern USGP Regime 2 is enhanced across all seasons, Regime 5 is enhanced in JJA, and Regime 6 is enhanced outside of DJF, while heat waves are suppressed in all seasons in Regime 3 (Fig. 3.4a). At lag 28 Regime 8 is largely producing increased heat wave rates only during JJA in the Southern and Central USGP and MAM in the Northern USGP (Fig. 3.4d-f). In the Central USGP most anomalous heat wave rates are due to anomalous heat wave rates in DJF and MAM. In the Northern USGP Regime 2 has higher than average heat wave rates in DJF, Regime 3 is suppressed during JJA, Regime 5 is suppressed during DJF.

Zooming out to a national level, the first thing to note is that the anomalous heat wave rate pattern closely matches the 500 mb geopotential anomalies for all regimes

(figs 3.1,3.5-3.7,B.1-B.6). Regimes 2, 5, and 6 are discussed below due to their tendencies to produce enhanced heat wave rates across the USGP. Regime 2 is associated with a higher heat wave rate over the northern and central USGP despite being near the baseline rate over the southern USGP (Fig. 3.5). When there is a heat wave in Regime 2, the northern USGP tends toward hot-humid while the southern and central USGP tends toward warm-dry heat waves. For regime 5, warm-humid heat waves are even more common for the northern USGP than was shown in the southern USGP (Fig. 3.6). Regime 6 tends toward the hot-dry HW type for most of the USGP, but that tendency is stronger towards the southern USGP than for more northern portions of the USGP (Fig 3.7). For completeness, the remaining regimes are shown in the Appendix in Figs. B.1-B.6.

3.3.3 Heat Wave Rates by ENSO and MJO phases

In this section heat wave frequency as a function of the ENSO and MJO phases, lead time, and atmospheric regime is evaluated. As discussed in section 3.1, both ENSO and MJO have been shown to modulate temperatures over the USGP, and WBGT is correlated to air temperature, it is hypothesized that WBGT heat waves will be modulated by the ENSO and MJO phases as well. Throughout this section the ENSO and MJO phase indicated will be the phase(s) on day 0, while the atmospheric regime and heat wave rates occur on the day indicated by the lag. Results are presented for ENSO and MJO separately and then for the joint ENSO and MJO phases together.

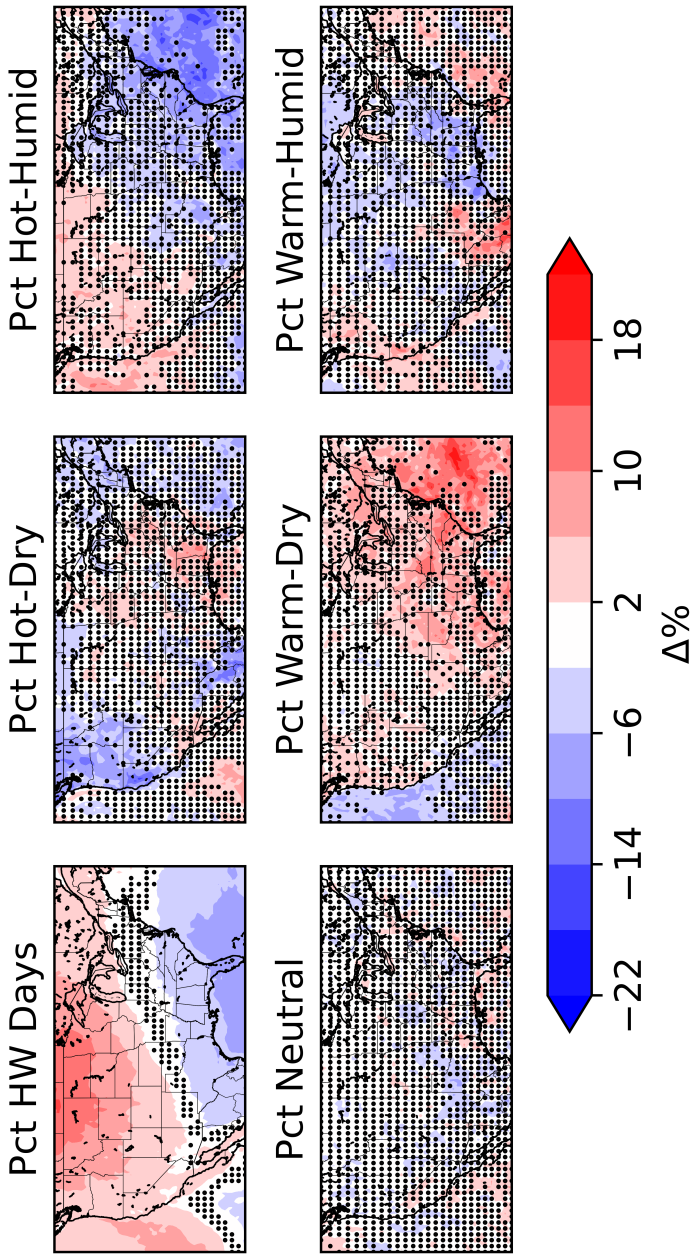

Figure 3.5: a) Heat wave rate for Regime 2 minus all regimes, b) Percent of heat waves that are of type Hot-Dry for Regime 2 minus all regimes, c) Percentage of heat waves that are of type Hot-Humid minus all regimes, d) Percentage of heat waves that are of type Neutral minus all regimes, e) Percentage of heat waves that are of type Warm-Dry minus all regimes, f) Percentage of heat waves that are of type Warm-Humid minus all regimes. Dots indicate where the difference from the baseline heat wave rate is not statistically significant at the 95% confidence level.

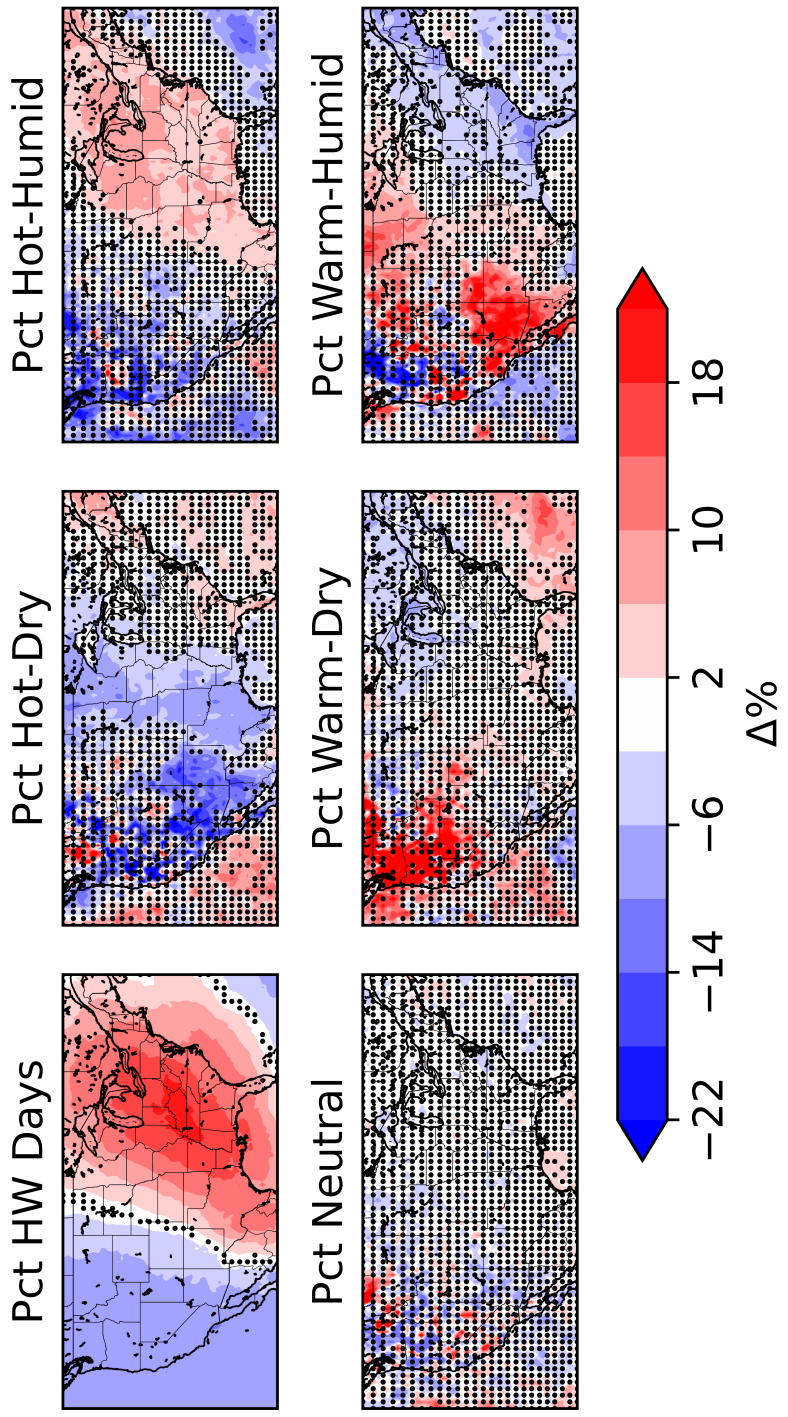

Figure 3.6: As in Fig. 3.5, but for Regime 5 minus all regimes.

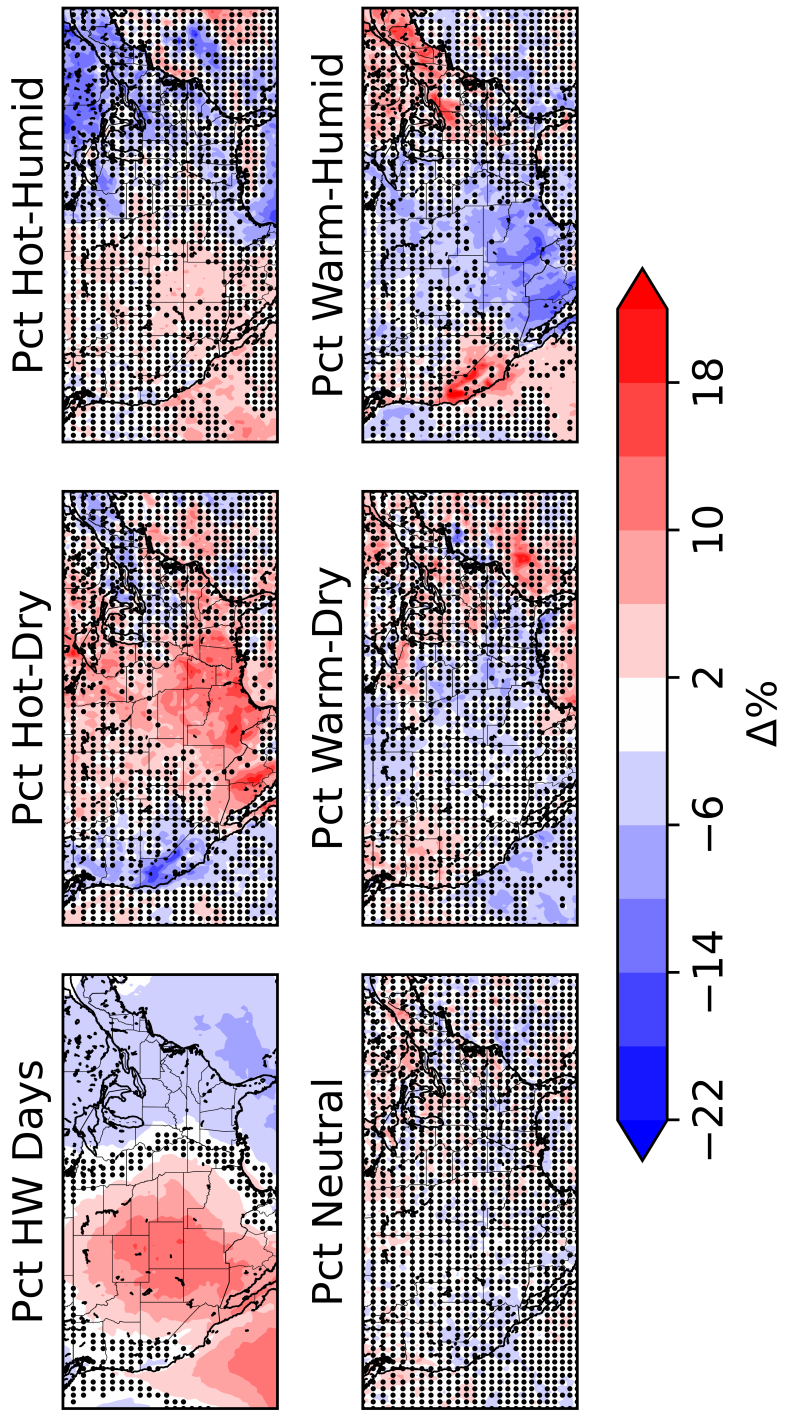

Figure 3.7: As in Fig. 3.5, but for Regime 6 minus all regimes.

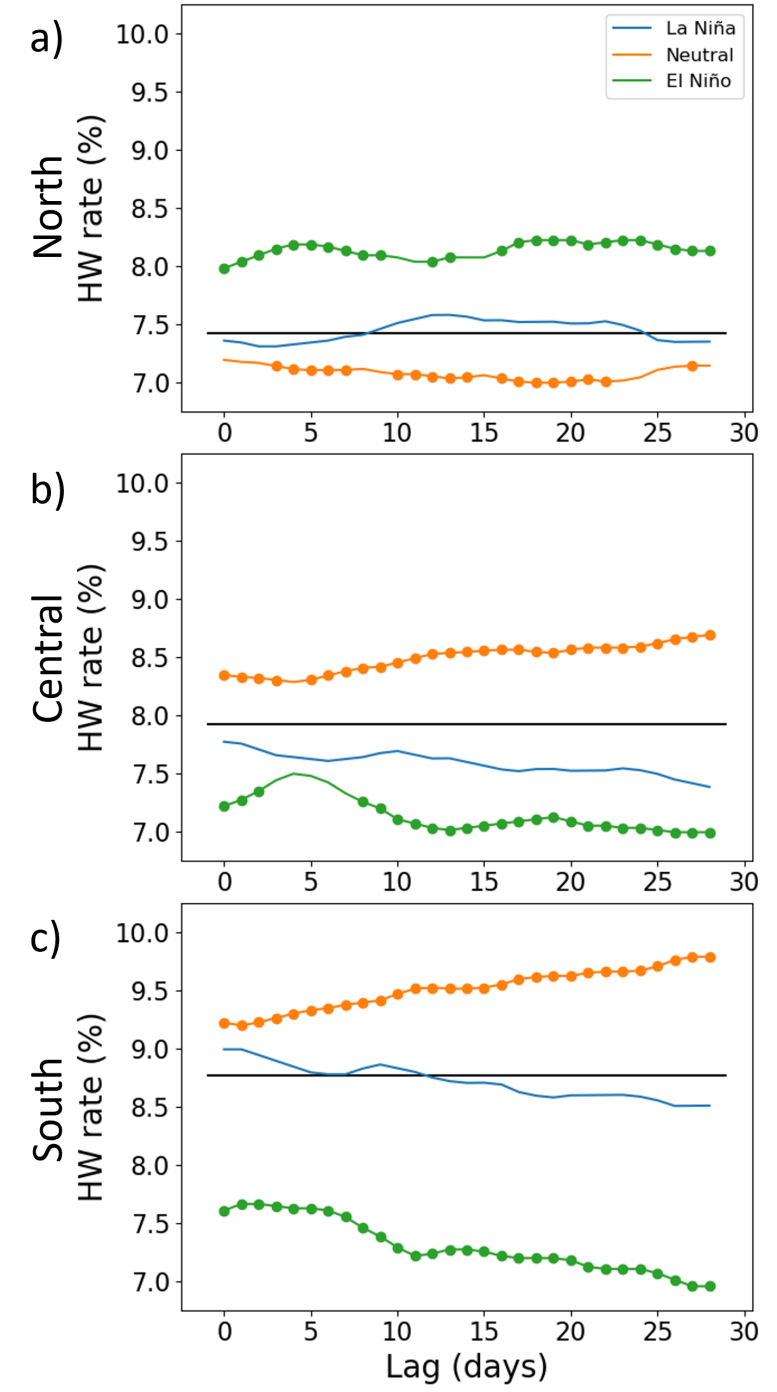

Figure 3.8: Heat Wave rate by ENSO phase and lead time at the a) Northern, b) Central, and c) Southern USGP location. Dots indicate where the heat wave rate is statistically significantly different from the baseline rate at the 95% confidence level, which is indicated by the black horizontal line.

3.3.3.1 ENSO

In the southern USGP there is not significant variation in heat wave frequency by lead time within a given ENSO phase, however what variation there is suggests divergence from the baseline rate as lead time increases (Fig. 3.8). Heat waves occur slightly more frequently than average during neutral conditions, with heat waves during La Niña occurring at rates near average and El Niño occurring less frequently. By day 28 heat waves occur at roughly 9.75% for neutral conditions compared to the mean rate of around 8.75%, while La Niña heat wave frequency is around 8.5% at 28 days lead time and El Niño heat wave frequency is approximately 7% at 28 days lead time. In the Central USGP the mean heat wave rate is lower than in the Southern USGP at around 7.9%, with neutral conditions producing heat waves at around 8.75% of days, La Niña at about 7.5%, and El Niño producing heat waves on around 7% by day 28. This is similar to what the Southern USGP experiences but at a slightly reduced heat wave frequency. However, in the Northern USGP El Niño produces heat waves most frequently at around 8% of all days compared to the local mean of 7.4%, La Niña is generally near the local mean, while neutral conditions produce heat waves around 7.2% of all days.

Including the atmospheric regimes (Fig 3.9, in the Northern USGP Regime 2 consistently has a HW rate between 15 and 20% at all lead times and ENSO phases and is the most frequent of all Regimes (Fig. 3.9a-c). Under El Niño conditions Regime 8 produces heat waves at around 15% of all lead times. Regime 6 also produces increased heat wave frequencies of around 10-15% for Neutral and El Niño conditions. Regime 3 almost completely suppresses heat wave conditions for all lead times regardless of ENSO phase, with Regimes 0, 1, and 4 all below 5% frequency, and Regime 7 below 5% frequency for Neutral and El Niño conditions. In the Central USGP Regime 6 is

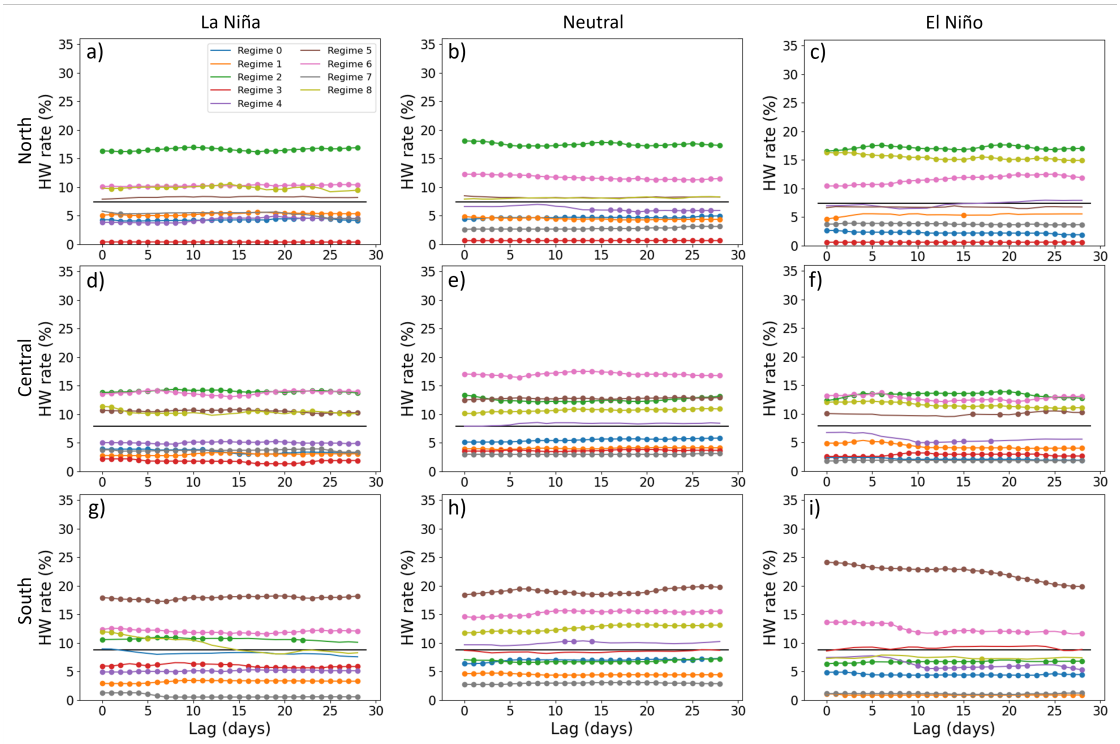

Figure 3.9: HW rate by ENSO phase (Left: La Niña, Central: Neutral, Right: El Niño), lead time, and Regime, at the a-c) Northern, d-f) Central, and g-i) Southern USGP location. Dots indicate where the heat wave rate is statistically significantly different at the 95% confidence level from the baseline rate, which is indicated by the black horizontal line.

associated with increased heat waves during Neutral ENSO conditions at around 17%, and is around 12-15% during La Niña and El Niño conditions (Fig. 3.9d-f). During Regime 2 heat waves occur at just under 15% regardless of ENSO phase, and Regime 8 is also associated with enhanced heat wave probabilites around 10-12%. Regimes 0, 1, 3, and 7 are generally associated with suppressed heat wave rates below 5%. In the Southern USGP heat waves occur most frequently when Regime 5 is in place with heat wave rates of 17-20% for La Niña and Neutral conditions and up to 25% for short lag El Niño conditions (Fig. 3.9g-i). Additionally, Regime 6 is produces up to 15% heat wave rates, particularly during Neutral ENSO conditions. Generally Regimes 4 and 7 are the most suppressive to heat waves, particularly during El Niño where heat wave rates are around 1%.

3.3.3.2 MJO

Breaking down the heat wave rates by MJO phase and lag time indicates that most phases at each locations have specific lag days where the heat wave rate is higher than the rest of the lead times (Fig. 3.10). In the Northern USGP Phase 3 is most frequent around 14-20 days lag time, with phase 4 being more frequent at 7-15 days, phase 5 at 5-15 days, and phase 6 during days 0-5 with all of these peaking around 11-12% frequency (Fig. 3.10)a. This progression is likely primarily representing the influence of 1-2 phases and then is an artifact of the MJO progressing through the phases over time. Similarly Phase 6 reaches a minimum heat wave rate at around days 20-25, Phase 7 from days 15-20, and Phase 8 from days 7-14, each reaching a minimum heat wave rate around 5-6%. The central plains displays a similar progression for the peak in heat wave rate, with Phase 1 at days 20-25 days, Phase 2 at days 17-22, phase 3 at days 15-20, Phases 4 and 5 around days 5-15 and Phase 6 at days 0-2 (Fig. 3.10)b.

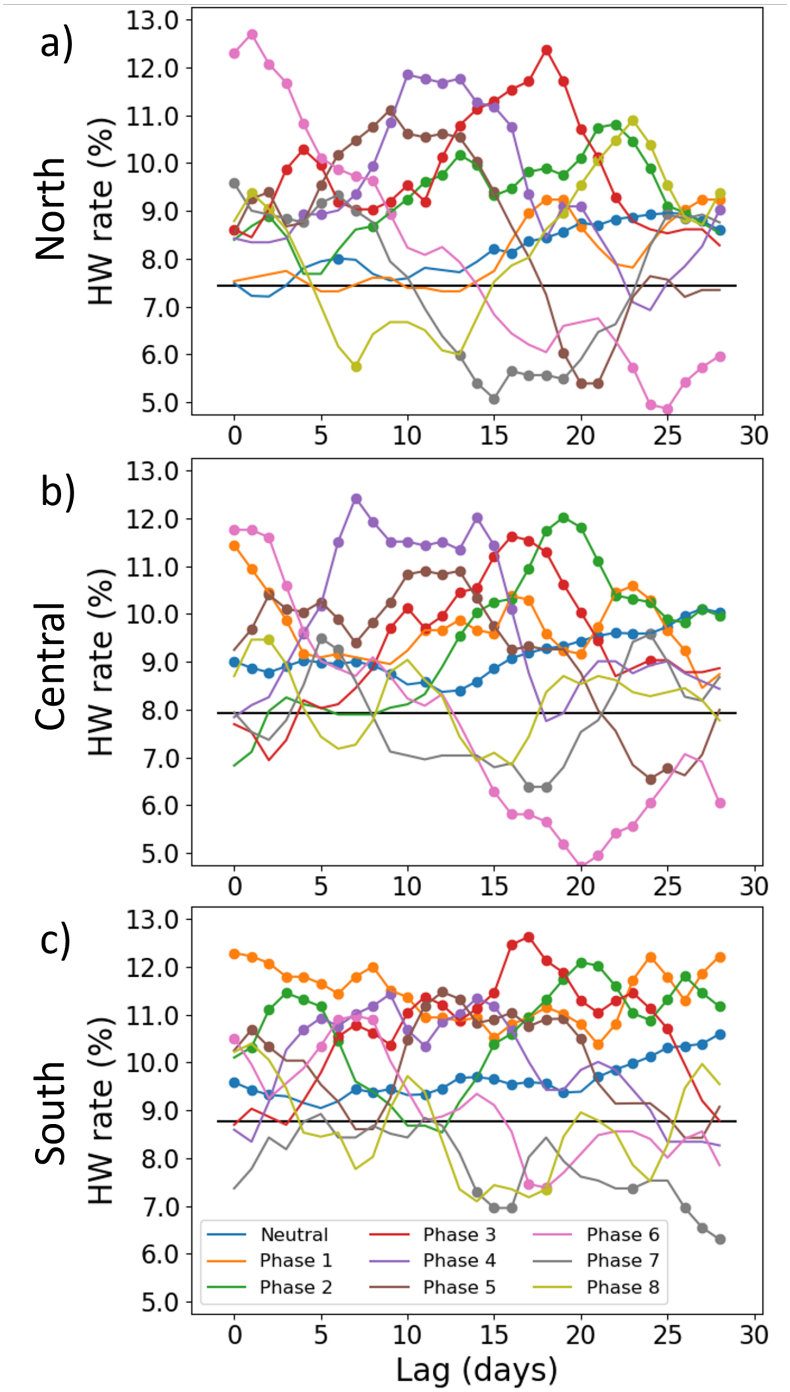

Figure 3.10: HW rate by MJO phase and lead time at the a) Northern, b) Central, and c) Southern USGP location. Dots indicate where the heat wave rate is statistically significantly different from the baseline rate at the 95% confidence level, which is indicated by the black horizontal line.

The peaks of each of these is around 11-12% with Phases 2, 3, and 4 having the largest peaks in the range of lag time 14-20 days. The only real lag times with suppressed heat wave activity is the progression of Phases 5-7, with Phase 6 having a minimum heat wave rate on 4.75% at day 20. In the Southern USGP Phase 1 is generally conducive to higher heat wave rates regardless of lag time, while phases 2-5 display a similar progression with shorter lag times as the phases increase starting from a peak in Phase 2 at around day 20, phase 3 around days 16-17, each of which have a heat wave rate of around 12% while phases 4 and 5 both peak around 11.5% lag 12-15, and phase 6 at about 11% at days 5-6 (Fig. 3.10)c. Phases 6-8 are all associated with suppressed heat wave rates after day 13, however there is only minimal lag between the 3 phases, each reaching a low of around 7% between days 12-18, with Phase 6 reaching the low at the later end and phase 8 at the earlier end of that range. Broadly speaking MJO Phases 2-6 are associated with enhanced heat wave rates 2-3 weeks after their occurrence, particularly with MJO phases 2 and 3 which tend to have the highest heat wave rates and sharpest heat wave rate maxima.

Further breaking each lag time into the specific regimes reveals that for the southern USGP Regime 5 has the highest heat wave rate regardless of MJO regime or lag time (Fig 3.11). However, there are still peaks in heat wave frequency. Regime 5 peaks at around lag 15-18 at phase 2 with a frequency of 30% and secondary peaks around lag 5 and lag 28. Progressing through phases 3-5 the peak remains around 30% but now is spread between days 10-25 for phase 3, 10-20 for phase 4, and then days 10-12 for phase 5 before peaking at nearly 35% at lag 7 following MJO phase 6. Regimes 6 and 8 show similar progressions but with peaks similarly around 20%, with Regime 6 reaching 25% around lag 25 days in Phase 3 and lag 15 days in Phase 4, and lag 7-9 days in Phase 6. For the Central USGP (Fig. B.7) Regime 5 has a heat wave frequency of around

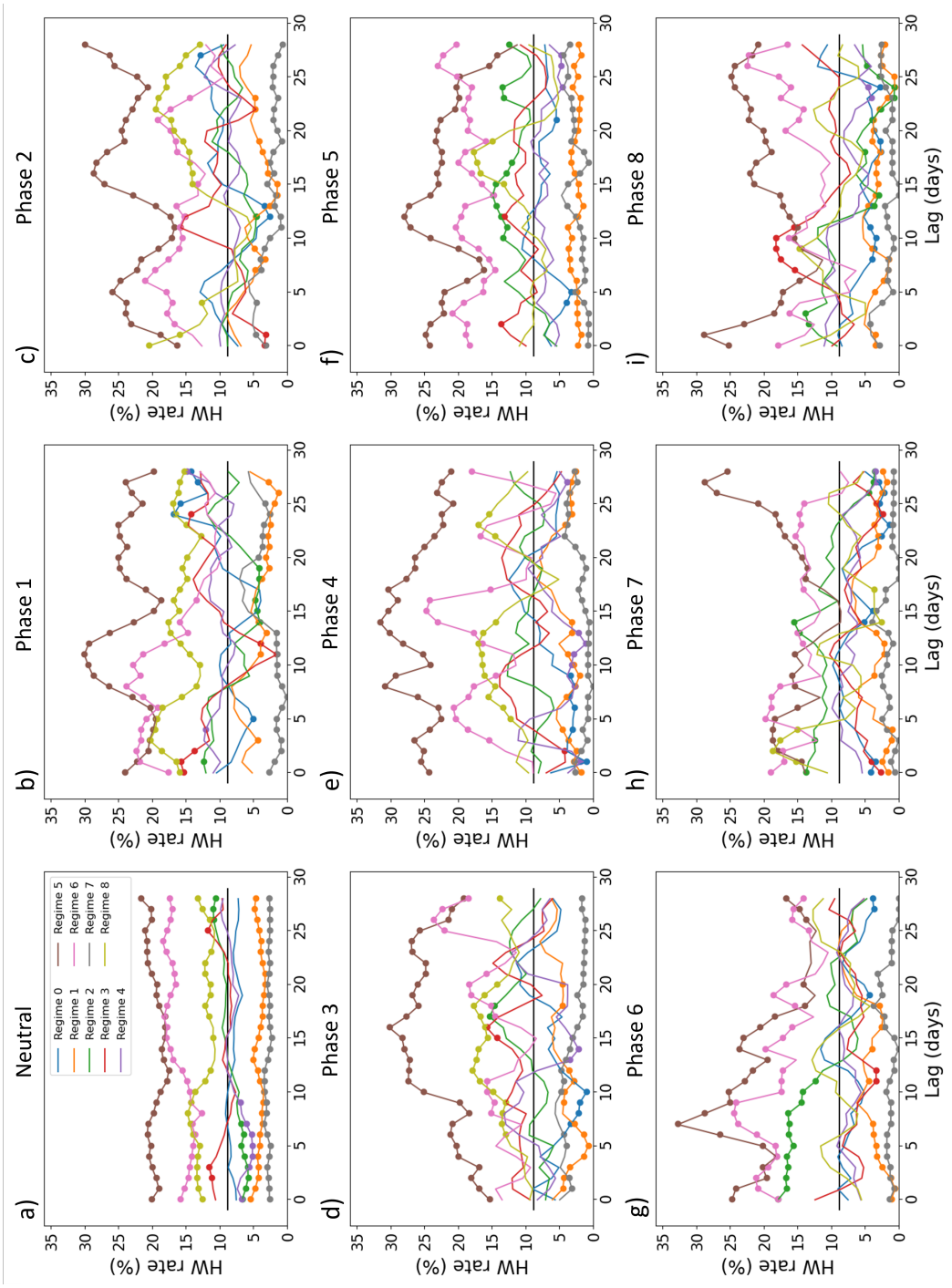

Figure 3.11: HW frequency for each MJO phase by regime and lead time at the Southern USGP location. Dots indicate where the heat wave rate is statistically significantly different at the 95% confidence level from the baseline rate, which is indicated by the black horizontal line.

3% during phase 1 at 20-25 lag days, which becomes an isolated peak in phases 3 and 4 at around 25% at days 15 then 7. Regime 5 generally has elevated heat wave rates of around 15-25% during MJO Phase 5. However, Regime 6 has a couple peaks in heat wave rate during phase 7 of >20% at days 16 and 23, which progress earlier to lag day 10 in Phases 8 and 1, and days 5-6 in Phase 2. Additionally Regimes 2 and 8 demonstrates a slight peak of around 15% during phase 2 around lag day 20 and which becomes generally elevated heat wave probabilities of around 15-20% for Phases 3-5 before a peak of 25% for lag days 0-10 in Phase 6. For Phases 7-8 Regime 2 is generally associate with elevated probabilities particularly at lag times less than 10 days, while Regime 8 is near normal heat wave rates. In the Northern USGP (Fig. B.8) there is a strong peak in heat wave frequencies (>15%) associated with Regime 2 after about lag day 15 during MJO phase 2. This peak moves earlier and stronger through MJO phase 6, with a peak of around 30% at lag day 15 during Phase 3, between days 3 and 11 during Phase 4, and a peak around 25-30% at lag time 0-1 and 8-10 for Phase 5. During phase 6 there is a 35% heat wave rate associated with Regime 2 at lag days 0-2 during phase 6. Generally Regime 2 is associated with enhanced heat wave frequencies in the Northern USGP. Additionally Regimes 5 and 8 are associated with enhanced heat wave rates during Phases 1-4 for Regime 5 and Phases 2-7 for Regime 8.

3.3.3.3 Joint Impact of MJO and ENSO

Combining the MJO and ENSO phase allows to break down the heat wave rates even more (Fig. 3.12). Generally speaking, the heat wave rates are between 2 and 16% with a few minor exceptions for the entire domain and all phases of ENSO and MJO. The only combination that exceeds the 16% rate is for MJO Phase 6 during La Niña where it reaches 19% for lag 1 in the Central USGP and 17% in the Northern USGP.

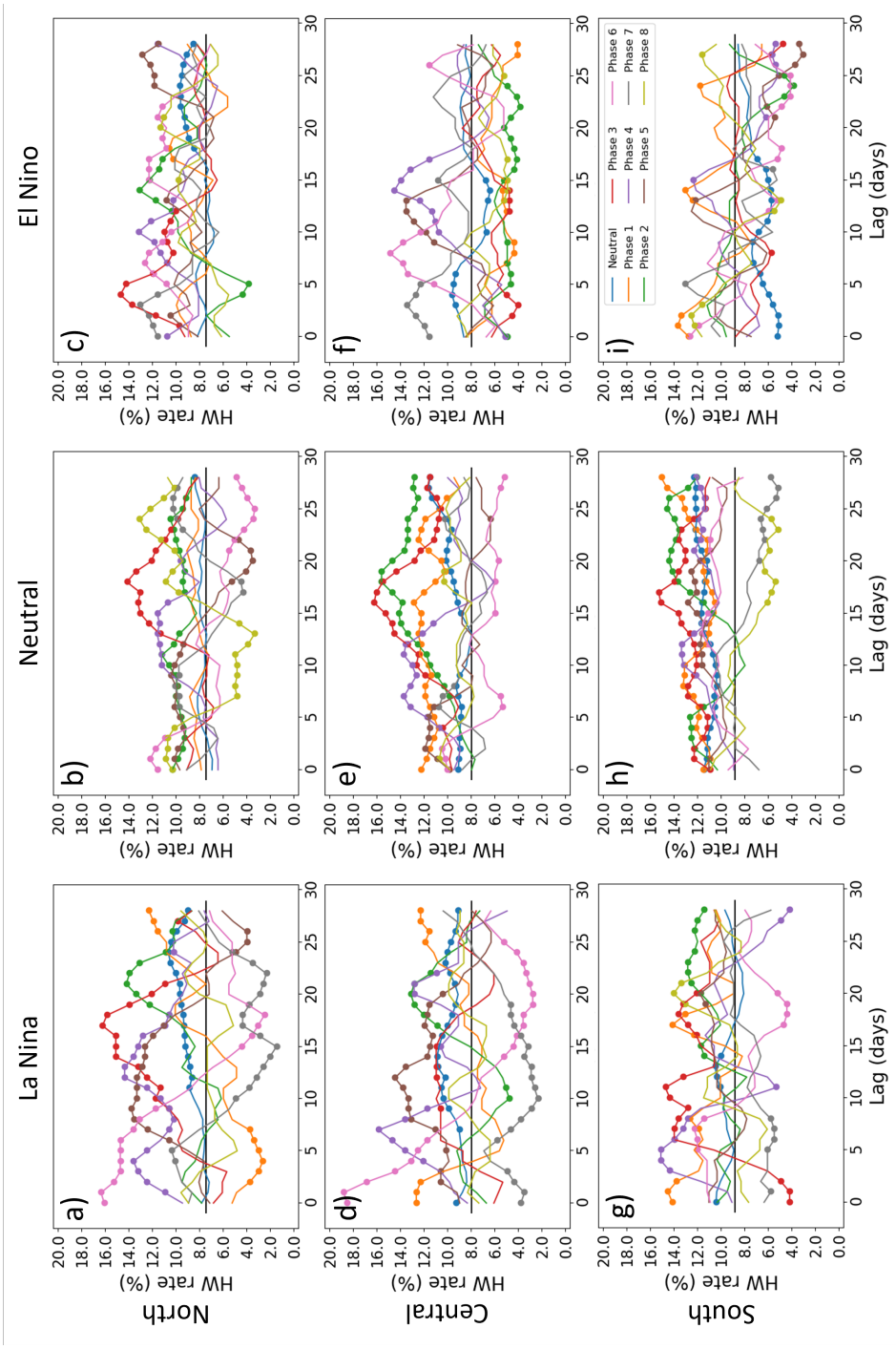

Figure 3.12: HW frequency by ENSO and MJO phase and lead time at the a-c) Northern, d-f) Central, and g-i) Southern USGP locations for the a,d,g) La Niña, b,e,h) Neutral, and c,f,i) El Niño phases of ENSO. Dots indicate where the heat wave rate is statistically significantly different at the 95% confidence level from the baseline rate, which is indicated by the black horizontal line.

As with the MJO, there tends to be a progression of the timing on each peak in heat wave rates from lower numbered MJO phases to higher numbered MJO phases as the lag time is reduced. However, MJO phases vary in the timing and magnitudes of their frequencies across ENSO phase in each region. For example, MJO Phase 3 has a peak between days 15 and 20 for La Niña and Neutral ENSO conditions while the peak is between days 2 and 5 for El Niño conditions. In the central region Phases 2 and 3 have a peak of around 16% at around 17 days during ENSO neutral conditions but does not have an equivalent peak in other phases. Phases 6 and 7 have heat wave rates near 2% at various lead times during La Niña conditions while there are peaks in those phases during El Niño at under under 10 days lead times without having periods that are below 5% rates. In the Southern USGP all MJO Phases except for Phases 7 and 8 are generally higher than average heat wave rates without much variance by lead times compared to the other phases. El Niño conditions are generally near normal with most MJO phases not statistically significantly different from average, however MJO neutral is typically between 5 and 7% heat wave rates, which is lower than the 9% average. For La Niña most MJO Phases have 1-2 peaks around 14% while Phases 6 and 7 are generally near or below average hate wave rates.

Adding the regimes to the ENSO and MJO phases allows for much more differentiation in heat wave rates. Fig. 3.13 show the likelihood of a heat wave given a positive ENSO phase (El Niño), with each panel corresponding to a phase of the MJO, and each curve in a given panel representing the observed heat wave rate if a specific regime occurs a specific number of days after the ENSO-MJO phase combination is observed. In general, during El Niño Regime 5 is associated with the highest heat wave frequencies. During MJO phase 4, for example, from days 13 through 20 has historically exceeded 35% if Regime 5 occurs, peaking at just over 50% at day 16. A

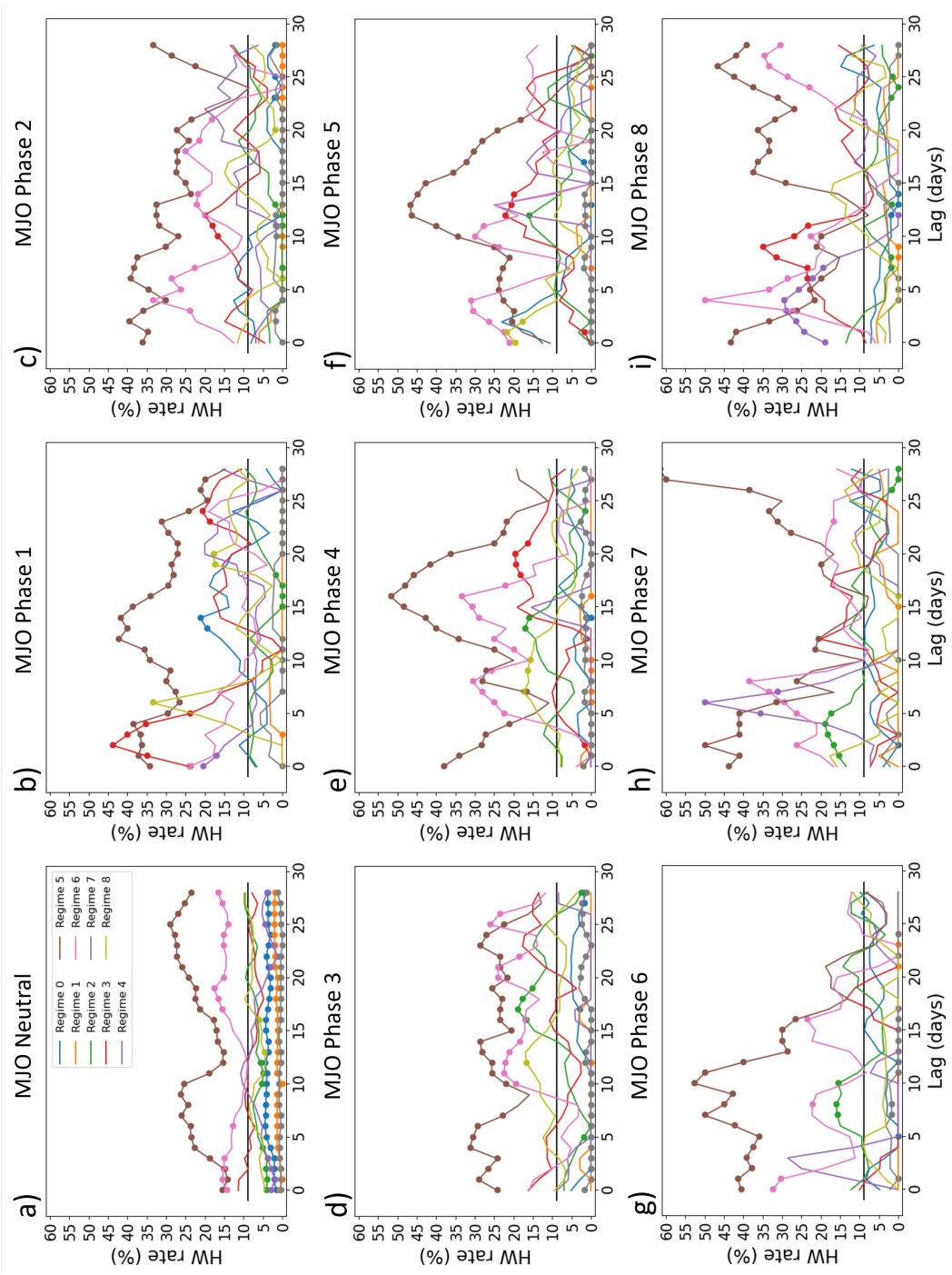

Figure 3.13: HW frequency by regime for El Niño by MJO phase and lead time at the Southern USGP location. Dots indicate where the heat wave rate is statistically significantly different at the 95% confidence level from the baseline rate, which is indicated by the black horizontal line.

similar peak occurs for MJO phase 5, 6, and 7 occurring around 4 days earlier as the phase progresses. Another peak occurs in MJO phases 7 and 8 at lead times greater than 20 days in MJO phase 7 and after day 15 in phase 8, with the highest values during MJO phase 7 occurring right around day 28 and peaking over 50% frequency, while the highest values in day 8 occur around day 25 with >45% frequency. Regime 6 is also has significant peaks in heat wave frequency, however outside of these peaks the values are not significantly different from climatology. Generally, these peaks in HW frequency associated with Regime 6 occur at similar times to those in Regime 5, but with the timing off by a couple days. During MJO phase 1 there is a peak that occurs around day 3 that reaches 45%, and progressing into phases 2-4 there is a generally elevated heat wave rate around 30%. However, this elevated rate disappears after week 3 in MJO phase 4 with that cutoff occurring earlier of the next few phases. A peak at around 50% does occur around day 5 during MJO phase 8. Otherwise, Regimes 0, 1, and 7 are typically associated with very low heat wave rates at or below 5%, often with no observed heat waves.

For ENSO neutral (Fig. 3.14) most MJO phases exhibit slightly higher heat wave rates than climatology, with MJO phase 7 being the only phase with heat wave rates consistently less frequent than climatology. As with El Niño Regimes 5 and 6 are frequently associated with peaks in HW rate, although typically these peaks are around 30% frequency with a couple peaks to about 40%, e.g. Regime 5 around day 10 for MJO phase 1, and day 15 for MJO phase 3. However, unlike the positive phase, several additional regimes have increased heat wave rates. For example, Regime 8 has a peak around 25% after day 15 for MJO phase 2, which remains in place although often progressing into shorter lag times as the MJO phases progress to higher values, with a second peak appearing during phase 4 that exhibits a similar earlier propagation to

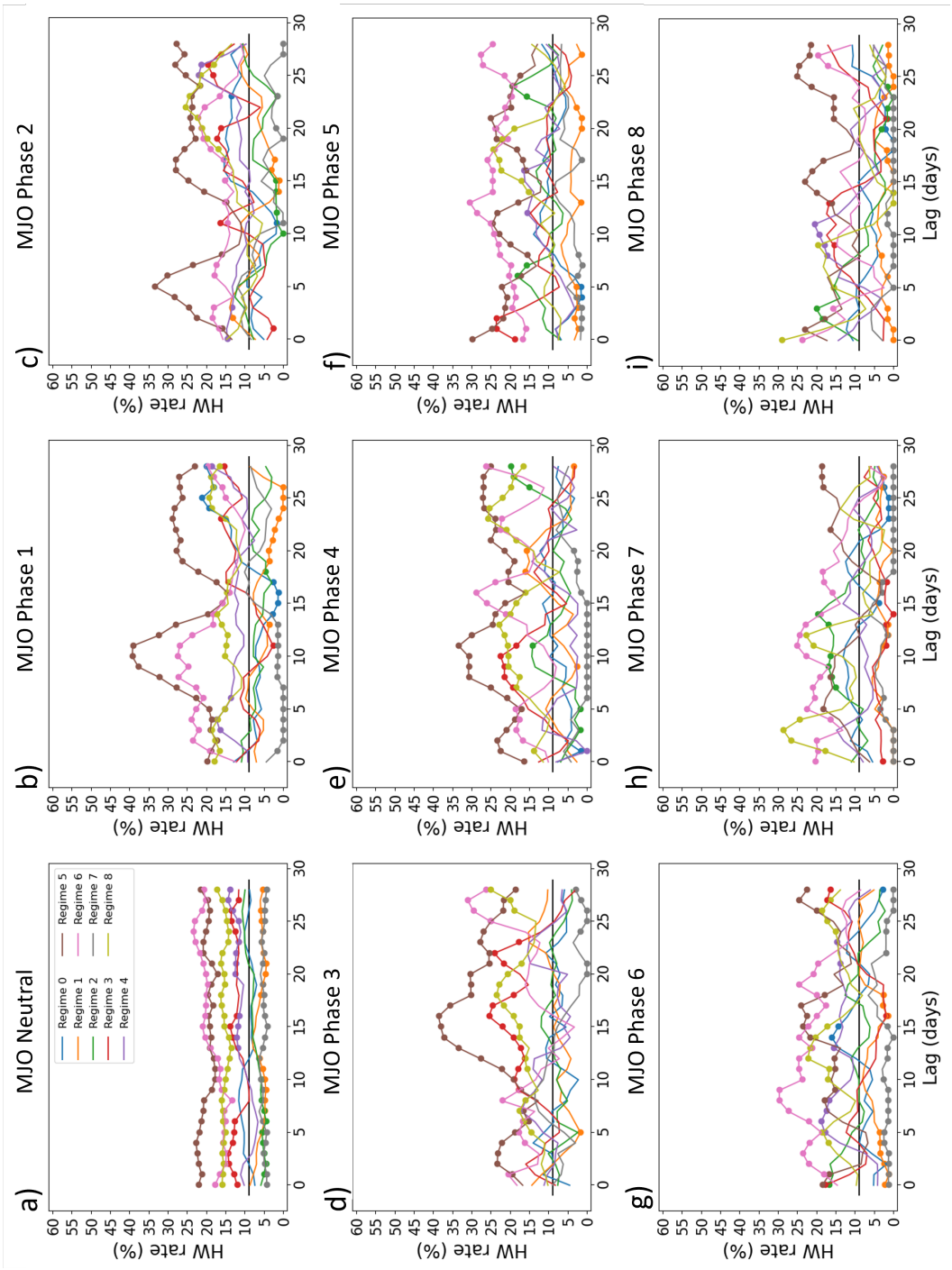

Figure 3.14: HW frequency for Neutral ENSO phase by MJO phase and lead time at the Southern USGP location. Dots indicate where the heat wave rate is statistically significantly different at the 95% confidence level from the baseline rate, which is indicated by the black horizontal line.

shorter lag times as the phases progress. While previously shown that Regime 4 is often associated with suppressed heatwave activity, HW rates peak during MJO phase 2 at around 20% for days >18, 25% for days 15-23 after MJO phase 3, and around days 5-10 after MJO phase 4. Other periods Regime 4 is still associated with suppressed heat wave activity but this is often not statistically significantly different from climatology. Regime 2 is also associated with enhanced heat wave rates from days 5-15 following MJO phase 7 and prior to day 5 following MJO phase 8.

For La Niña, MJO phase 1 is the primary phase with enhanced heat wave rates at about 14%, while MJO phase 3 is suppressed at just around 4% baseline rates (Fig. 3.15). As with other ENSO phases, Regime 5 is typically associated with enhanced heat wave rates, although for all MJO phases except 3-5 there are periods of near normal heat wave rates, mostly at short lead times, except for Regime 6 where there is a peak in HW rates around day 7 at around 45% frequency. Regimes 2, 6, 8 also have notable peaks in heat wave frequency. Regime 2 has peaks at both in the first week and the 4th week during MJO phase 1, shifting to the first and third weeks in phase 2. By phase 3 and 4 there are peaks around the third week at around 30% which then progresses into the first and second weeks for MJO phases 6 and 5 respectively, while a peak appears in the third week after MJO phase 7, that becomes week two with phase 8. Regime 6 has a spike around day 21 after MJO phase 8 at around 40% frequency which shows up around days 5-12 after MJO phases 1-2, and days 5-6 after MJO phase 3. Regime 8 has a peak around week 4 in MJO phase 8 that becomes a peak around 45% frequency following MJO phase 1.

For the Central and Northern USGP, the results are similar, but with some specific details such as the exact regimes, MJO phases, and the peak heat wave rates differing. One notable detail for the Central USGP (Fig. B.9) during El Niño Regimes 2, 3,

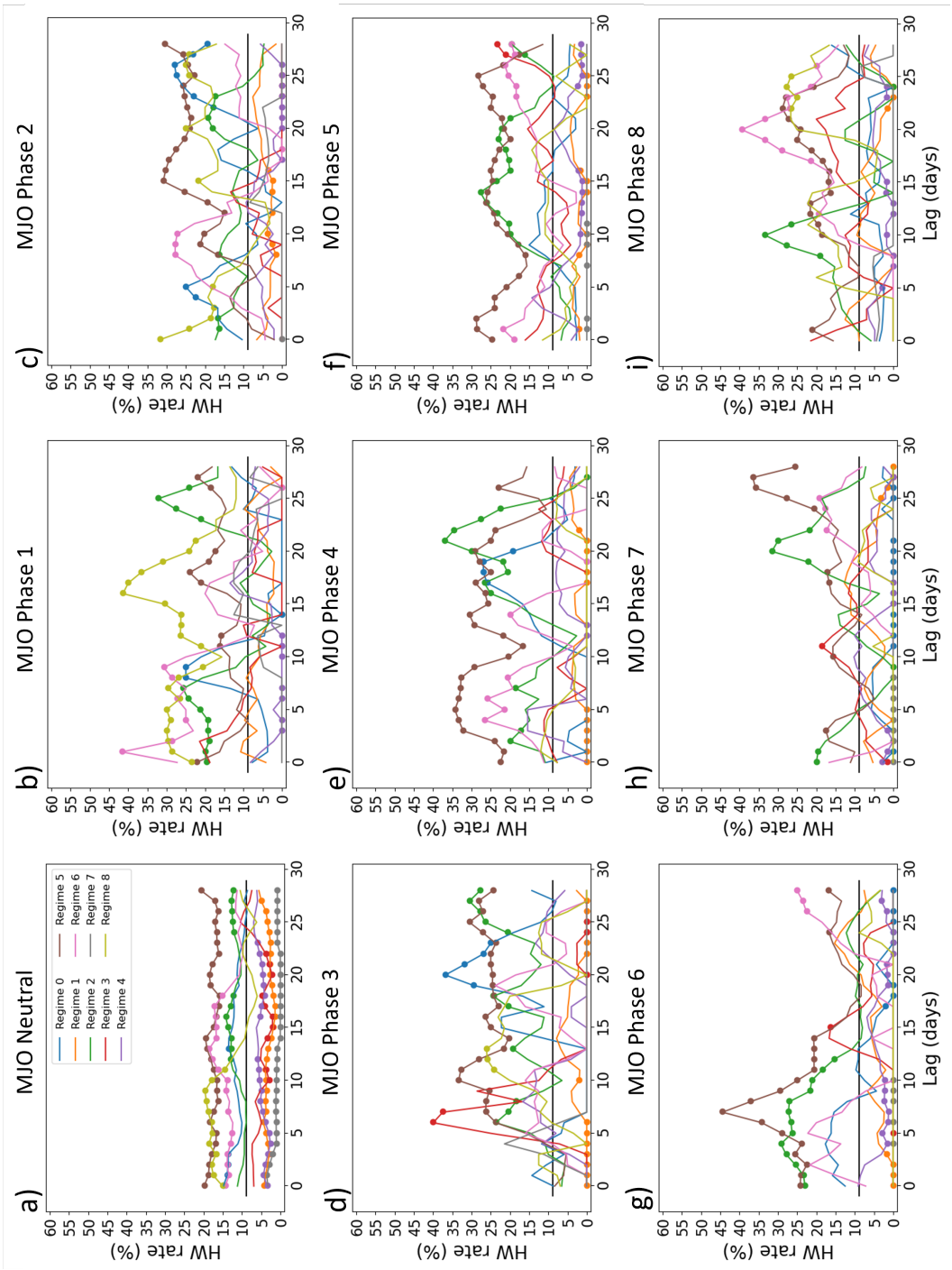

Figure 3.15: HW frequency for La Niña by MJO Phase and lead time at the Southern USGP location. Dots indicate where the heat wave rate is statistically significantly different at the 95% confidence level from the baseline rate, which is indicated by the black horizontal line.

5, and 6 all have peaks around lag days 14-15 around 25% and then Regimes 2 and 6 progress earlier through Phases 5 and 6, with Regime 2 increasing 40% heat wave frequency during Phase 6 at lag day 7. For the Central USGP during ENSO Neutral (Fig. B.10) Regime 5 has a peak of around 35% heat wave frequency from days 20-25 during MJO Phase 1 which progresses earlier through MJO Phase 5 with slightly decreasing frequencies occurring as the MJO Phases progress. However, Regime 5 is not the only regime with enhanced heat wave probabilities, as Phases 2, 6, and 8 all have periods of enhanced heat wave rates. For La Niña in the Central USGP (Fig. B.11) Regimes 2, 5, and 8 all have heat wave frequencies of around 30% near lag day 20 during MJO Phase 2, and all progress earlier in Phase 3 to around days 10-15, however Phase 8 is not statistically significantly different from the local average heat wave frequency. By phase 4 the heat wave frequencies are peaking around day 5 for Regimes 2 and 5 at just under 25%, Then for Phases 5 and 6 Regimes 2 and 5 have a peak around 15-20 days that moves to around days 0-10 by Phase 6. Overall the data is messy during La Niña for the Central USGP. At the Northern USGP location during El Niño conditions (Fig. B.12) Regime 2 is the predominant Regime associated with enhanced heat waves, with Regime 8 getting an honorable mention. At Phase 2 Regimes 2 and 8 both peak around days 10-20 at 35% and 25% respectively, and progress earlier in Phase 3 to around lag day 5. For Neutral ENSO conditions in the Northern USGP (Fig. B.13) Regime 2 is the predominate regime associated with higher heat wave rates peaking around 40% at lag 1 during MJO Phase 6, with elevated heat wave rates associated with Regime 6 during Phases 1-4, and a wave associated with Regime 8 found in Phases 3-8. Finally, for La Niña in the Northern UGSP (Fig. B.14) There are periods where each of Regimes 2, 6, and 8 have enhanced heat wave frequencies, with Regime 2 being the most prominent, peaking as high as 55% rates at

lag day 15 following Phase 3. However, Regime 8 also reaches frequencies as high as 45% at lag days 8 and 3 for Phases 6 and 7 respectively.

Maps of heat wave rates for several selected ENSO Phase, MJO Phase, Regime, and Lag time combinations are shown in Fig 3.16 to provide further spatial context for some of the higher heat wave rates seen in this section. It is clear that each of the MJO, Regime, lag combinations has variation in impact by ENSO phase. The first example, MJO 3, Regime 2, Lag 15 has higher heat wave rates focused in the Northern USGP, but the heat wave rates are highest for La Niña, and lowest for El Niño. The second example, MJO 4, Regime 5, Lag 16 has much higher heat wave rates over the Eastern CONUS than the Western CONUS, particularly during El Niño conditions. Finally, MJO 7, Regime 6, Lag 17, the heat wave rates are highest just east of the Rocky Mountains in western and central portions of the USGP, particularly during El Niño conditions. However, there are also elevated heat wave rates over the western half of the United States during El Niño conditions, while for La Niña and ENSO Neutral conditions there is a maximum in heat wave rates located in the Southwestern US and Northwestern Mexico. Each of these heat wave rates patterns correspond to the location of positive geopotential anomalies in their respective regimes.

Overall, these analyses show that by combining the MJO and ENSO phases with the 500 mb atmospheric regime, it is possible to find periods where the observed heat wave frequencies are as much as 6 time higher than the overall climatological average. Without the aid of numerical models predicting the atmospheric regime at these lead time, however, the best use is to look backward for the ENSO and MJO phases to identify the probabilities for now or near term heat wave activity. If an accurate model of 500 mb patterns can be used, then this data can be used to identify forecasts of opportunity at lead times of 3-4 weeks or more. The next section will evaluate the

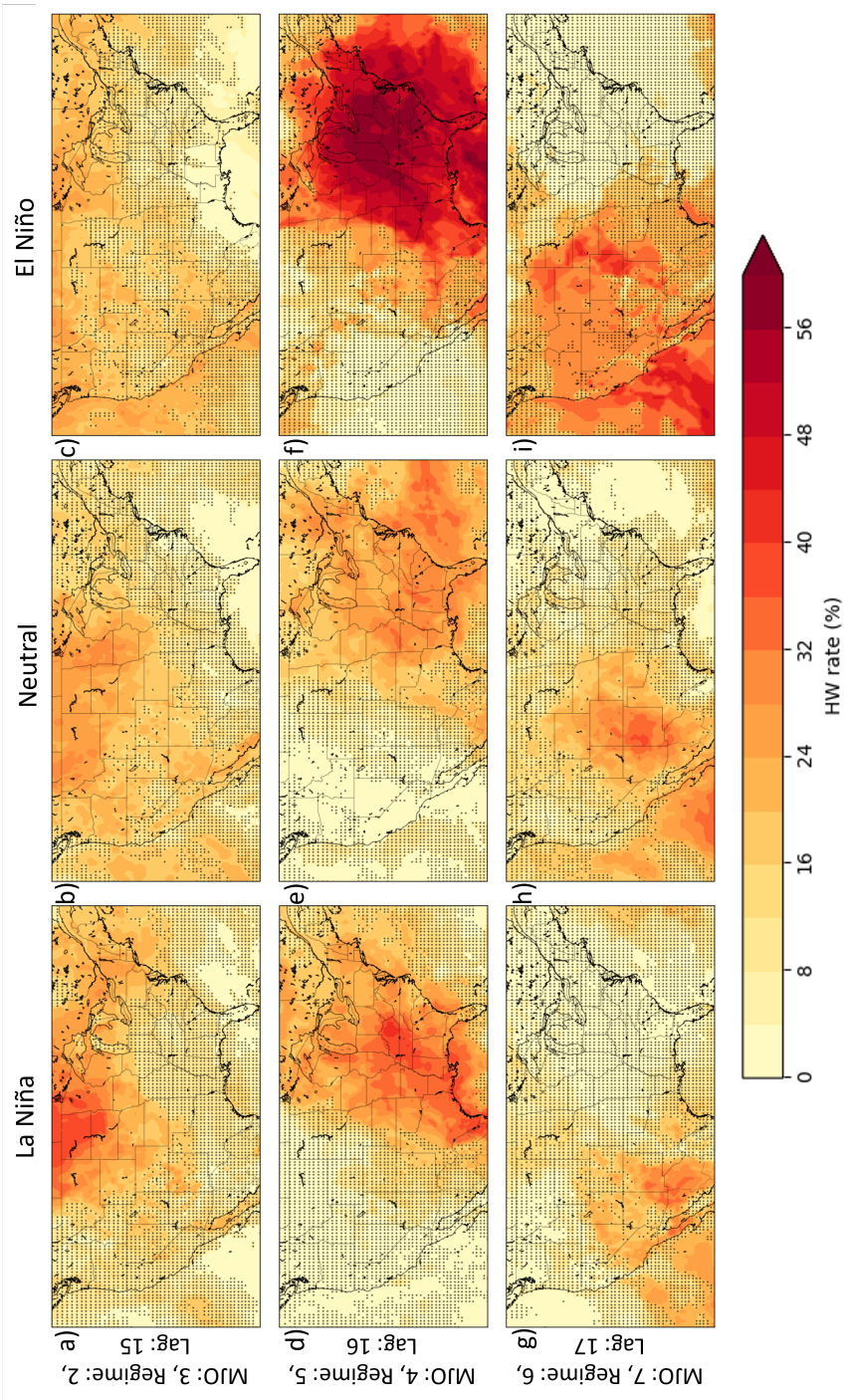

Figure 3.16: Heat wave rates for selected ENSO Phase, MJO Phase, regime, and lag combinations. a-c) MJO Phase 3, Regime 2, Lag 15, d-f) MJO Phase 4, Regime 5, Lag 16, and g-i) MJO Phase 7, Regime 6, Lag 17 for ENSO Phase a,d,g) La Niña, b,e,h) Neutral, and c,f,i) El Niño. Dots indicate where the heat wave rate is not statistically significantly different from the baseline rate at the 95% confidence level.

the accuracy of the ECMWF S2S model for the purpose of predicting these 500 mb patterns.

3.3.4 Model Verification

3.3.4.1 Regime Prediction

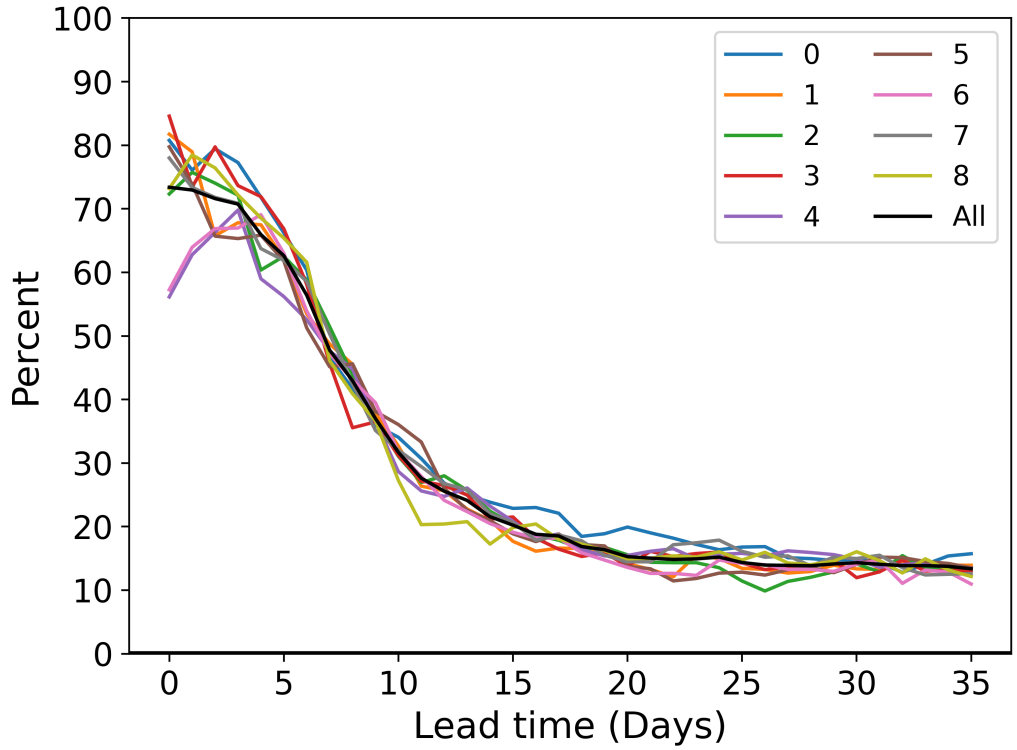

Figure 3.17: Observed probability of the ECMWF S2S model correctly predicting the 500 mb atmospheric regime by lead time as verified by ERA5 reanalysis.

On average, the ECMWF model is able to predict with around 75% accuracy the correct atmospheric regime at day 1, and drops to about 50% by day 7 (Fig. 3.17). By around day 14 the accuracy is at around 20%, and levels off around 15% by day 20. Generally all regimes are similar accuracy after the first week, where Regimes 4 and 6 are between 55 and 60% at day 1 before peaking at around 65 to 70% at

day 4. This lower accuracy is likely due to each regime being either a generally weak pattern or being roughly the midpoint between 2 other regimes. This problem is likely exacerbated due to the model climatology used to detrend and standardize the data being over a different time frame and more generally just a different dataset compared to the that the model was trained on. Overall, at short term lead times it is likely that the ECMWF could provide valuable information regarding the regime, but at lead times at or near the S2S time frame it is unlikely that the information provided by the model is particularly useful.

3.3.4.2 Regime Succession

To ensure that the ECMWF model is accurately representing the transitions between regimes, Fig. 3.18 shows the probability that the model will predict a given regime at each lead time after predicting each regime. Each panel represents a given day 0 regime, and each line represents the probability that a regime will be predicted at a given lead time minus the observed frequency of each regime at a given lead time, so a positive value indicates the model is overpredicting the occurrence of a regime and negative indicates an underprediction by the model. The main thing to notice is that Regime 4 is consistently underforecast after all regimes, with Regime 4 being particularly unlikely to occur following another Regime 4 day at short lead times, suggesting that Regime 4 is unstable in the ECMWF S2S model, as even when it is predicting Regime 4, it is moving out of regime 4 too quickly. All other regimes are generally within +- 5% of their observed rates, however unless the specific regime was the day 0 regime, they are typically at around 15% frequency. This means that, for example, Regime 2 is predicted at around half to two-thirds the observed rate following Regimes 1 and 5-8, and regimes such as regimes 1 are over predicted by one-third to

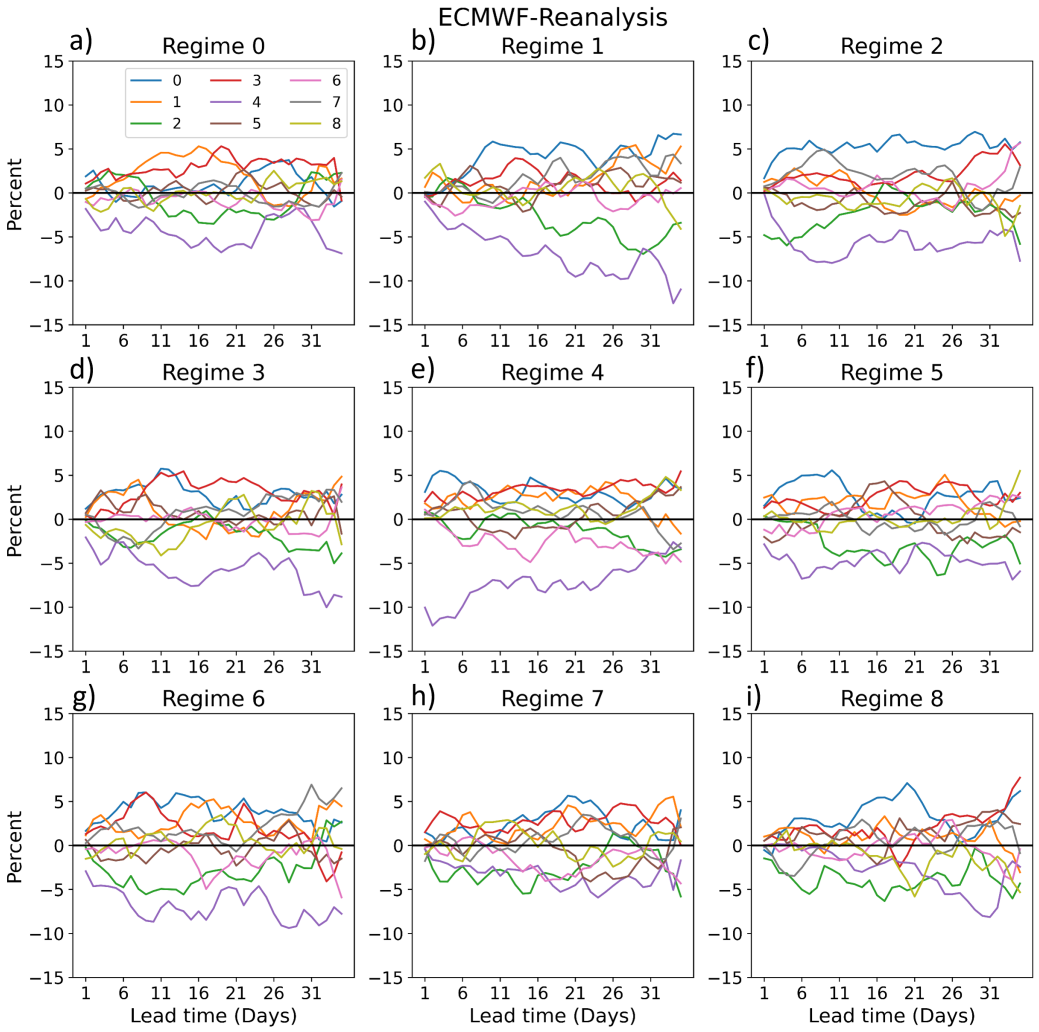

Figure 3.18: Difference in frequency of each regime occurring at each lag time up to day 28 following each day 0 regime between ECMWF S2S model forecasts and ERA5 reanalysis. ECMWF S2S model minus ERA5 reanalysis.

one-half of their observed rate following several regimes. Generally most regimes are within 1-2% or one-tenth of the observed frequency, of the observed frequency.

3.3.5 Prediction

As previously mentioned, the heat wave frequency statistics previously calculated have a lag between the ENSO/MJO phase and the atmospheric regime. Strictly speaking, those are using the current regime combined with the ENSO and MJO phase combination at a specific number of days in the past. However, if we were able to start from the ENSO/MJO phase and predict the atmospheric regime, we could forecast the likelihood of a heat wave at each given location as this is the same problem, just working from the other end. The S2S model discussed in the previous section does exhibit some skill in predicting atmospheric regimes at lead times out to at least 35 days. The question we seek to answer is whether this skill is useful enough to identify potential heat waves at 3+ weeks when combined with the historical heat wave rates.

For this discussion, a simple model combining the regimes computed from the ECMWF 500 mb geopotential height forecasts and the annual climatology of heat wave rates for each ENSO/MJO/Regime/Lag combination discussed in section 3.3.3.3 is evaluated. Simply put, for each model run, the ENSO and MJO phases at model initialization time are determined. Then the 500 mb atmospheric regime is calculated for each ensemble member for each forecast lead time. Then, using the climatology data as a lookup table, the historical heat wave rate given the day 0 ENSO/MJO, and the Regime at the specific lead time (which is the lag) is found and is considered the ensemble members' heat wave probability forecast for each lead time. The result will be an average of several maps like those shown in Fig. 3.16 which may be used to forecast locations more likely to experience a heat wave.

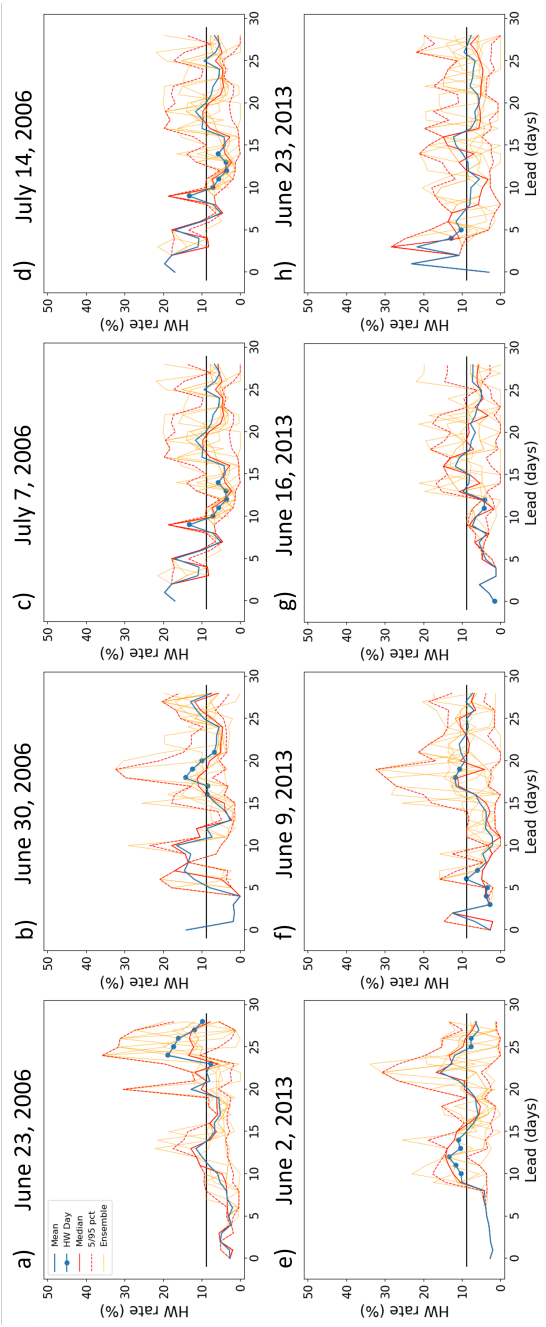

Figure 3.19: Selected examples of a heat wave model combining heat wave climatology and ECMWF S2S model forecasts initialized from the date indicated. Orange lines indicate the probabilities associated with each ensemble member Regime forecast, dashed red lines are the 95th and 5th percentile of ensemble members, the solid red line is the 50th percentile of the ensemble members, the blue line is the ensemble mean, and blue dots on the ensemble mean line indicate heat wave days. All panels are for the Southern USGP location.

Selected cases at the Southern USGP location suggest that even with the lower model accuracy beyond about 2 weeks at predicting the atmospheric regime there can be signals in the ensemble that can hint at enhanced likelihood of heat wave occurrence (Fig. 3.19). Typically, even when there is enhanced heat wave likelihood, only a few members will suggest it, but the peak in the 95th and 5th percentile ensemble member and/or mean ensemble member probabilities will be increased relative to surrounding dates. Two examples are provided here from 23 June 2006 and 2 June 2013. These are admittedly the best examples of the 21st century, however it shows that there is potential with further refinement. Areas of refinement that can be made immediately is breaking the heat wave rate statistics down by season, and bias correcting the model regime output prediction. However, for seasonality this may reduce the sample size to a point where significant noise is introduced. For the regime predictions, in theory the ensemble should provide a flow dependent distribution, but the biases will still be present. The individual members could be bias corrected, but that might reduce the amount of flow specific information. Sample size bias may be slightly reduced by accounting for the probability of a heat wave within a certain radius and period of longer than a day, but this information is correlated and will have an effective sample size significantly smaller than an uncorrelated sample of the same size.

3.3.6 Discussion

Several sources of predictability for WBGT heat waves in the USGP are presented in this study. As discussed in section 3.1 heat waves tend to occur under high pressure (Perkins 2015). Section 3.3.2 demonstrates that this pattern largely holds true for WBGT heat waves across North America. This result is expected, especially since high pressure typically is associated with light winds and increased solar radiation due to reduced cloud cover, both of which increase WBGT.

By organizing the atmosphere into regimes, it becomes apparent that some regimes favor heat waves while others suppress them. While it is common to use 4-5 atmospheric regimes over North America (Lee et al. 2019, 2023; Millin et al. 2022), 9 are kept here as there are physical differences relevant to heat wave forecasting that appear with 9 regimes that increase predictability both as far as distinguishing heat wave rates and distinguishing heat wave types. As an example, at the southern location, the two most favorable regimes (5 and 6) are supportive of heat waves of different types, specifically hot-dry and warm-humid. However, if only 4 regimes are created Regimes 5 and 6 partially or completely combined with less favorable regimes that reduces the maximum heat wave rate from 19% to just 13%, which is more than half of the difference between the regime rate and the climatological rate of 8.77% (not shown). This is partly due to Regimes 5, 6, and 7 all representing Rossby Wave trains that are 1/4 out of phase from each other which place the Southern USGP location variously under southwesterly dry air advection, southerly humid air advection (both supportive of heat waves), and northerly cool air advection (suppressive to heat waves), which may get combined together or with other regimes.

The impact of ENSO on heat wave rates has been discussed in the literature previously (Ropelewski and Halpert 1986; Kenyon and Hegerl 2008; Koster et al. 2009; Behera et al. 2013; Hoerling et al. 2013, 2014; Loikith and Broccoli 2014; Seager et al. 2014; Lopez et al. 2019; Luo and Lau 2020). This study shows that La Niña has historically produced a higher WBGT heat wave rate than El Niño in the Southern and Central USGP, while the opposite is true in the Northern USGP. It has been well documented that temperatures in the Southern USGP are warmer under La Niña than El Niño conditions (Ropelewski and Halpert 1986; Kenyon and Hegerl 2008; Koster et al. 2009; Hoerling et al. 2013, 2014; Seager et al. 2014; Lopez et al. 2019), and some significant heat waves such as the 2011-12 southern great plains heat wave have been

associated with La Niña (Hoerling et al. 2014). This puts the WBGT heat wave rates in line with the known air temperature variability within ENSO. Of note, it has been suggested that transitions from El Niño to La Niña are supportive of heat waves in the USGP (Luo and Lau 2020). Our results suggest that neutral conditions are the most supportive of heat wave occurrence in the Central and Southern USGP, and could be related to this transition. However, this is uncertain due to the observed suppression of heat waves in La Niña to El Niño transition (Behera et al. 2013; Loikith and Broccoli 2014), which could offset some or all of any increase in heat wave rates from the El Niño to La Niña transition.

Combining the ENSO phase with the MJO phase and atmospheric regime is shown to have significant predictive skill. Peak heat wave rates for Phases 3-6 are often around twice the baseline rates, particularly during La Niña. This is in agreement with the findings from Wang et al. (2023) where they saw the frequency of hot-dry extremes increase by similar magnitudes. For each ENSO and MJO phase combination, the observed heat wave frequency for the occurrence of each atmospheric regime up to 28 days later is shown. Some combinations suggest that for certain ENSO/MJO phase combinations, the occurrence of certain regimes between 2 and 4 weeks later have historically resulted in heat wave rates in excess of 50%. Without knowledge of a future regime this would be applied by taking the current atmospheric regime and take the MJO/ENSO phase from l days prior. However, from a forecasting perspective, the use of a dynamical model to forecast the atmospheric regime would open up a lot of opportunity if it is accurate enough to be useful. In such case the historical climatology could be combined with the observations and model output in order to provide lead time of 3 weeks or more for some heat waves.

However, a number of studies have found that both for temperature anomalies (Tian et al. 2017; Vitart et al. 2019; Lin and Mo 2022; Domeisen et al. 2023) and

atmospheric regimes (Büeler et al. 2021) dynamical and probabilistic forecasts have little predictive skill beyond 2-4 weeks. In fact, 3.3.4 suggests that the ECMWF S2S model is only able to predict the regime above even 25% accuracy out to 2 weeks, and is begins to level out around 15% around 3 weeks lead time. This doesn't necessarily mean that there isn't useful information in the model distribution, but it will likely have a lot of noise. Further, with biases in the frequency of some regimes, events under those regimes may be significantly misrepresented. It may be possible to bias correct the ensemble output to better represent the relative frequency of regime occurrence, but without a significant increase in the convergence of forecasts on the correct regime or similar regimes a model mean solution will likely only be useful for up to 2-3 weeks. However, information may still be gleaned from the range of ensemble solutions, where there may be an increase in members suggesting high frequency of heat waves based on the climatology or a decrease in low heat wave outlook scenarios. A rudimentary model does suggest that this may be true, however there are many false alarms and missed events as well.

3.3.7 Conclusions

This chapter discusses several sources of predictability for WBGT heat waves in the USGP by analyzing the historical heat wave rates associated with the relevant predictor. One such predictor is 500 mb atmospheric regimes, where several patterns correlate with heat wave occurrence. Regimes 5 and 6 resemble Rossby wave trains with high pressure over the USGP and are generally conducive to heat waves, particularly in the Southern and Central USGP. Regime 2 has anomalously high pressure over Canada and the Northern USGP and is associated with higher heat wave rates over the Northern USGP. Generally, positive 500mb geopotential anomalies are associated with positive WBGT heat wave rate anomalies. The 500 mb geopotential height anomalies

also correlate with heat wave type in some instances. For example, Regime 5 is typically associated with warm-humid heat waves, while Regime 6 is typically associated with hot-dry heat waves. However, using the Regimes as the sole predictor for 28 days lead time only provides weak anomalies, that while statistically significant, are not necessarily large enough to be useful.

Another source of predictability is the ENSO phase. Generally, WBGT heat wave rates are higher during La Niña than El Niño in the Southern and Central USGP, but higher for El Niño in the Northern USGP. Combining ENSO with the 500 mb atmospheric Regimes shows that it is possible in some cases to identify some forecasts of opportunity resulting from variation in heat wave rates for a regime by ENSO phase. For example, Regime 8 in the Northern USGP is near normal heat wave rates (around 8%) during La Niña and Neutral conditions, but is nearly double that during El Niño conditions at >15%. On the other end of the spectrum, In the Southern USGP, Regime 1 is typically around 5% heat wave rates, but during El Niño it is nearly 0%, and similar behaviour is seen in Regime 0 in the Central USGP. Several other regimes provide a few extra percent difference from their average rates depending on the ENSO phase as well.

A third source of predictability is the MJO phase. Each phase typically is associated with enhanced heat wave probabilities at a certain lead time, with phases 2 and 3 being in the 2-3 week lead time and phases 4 and 5 in the 1-2 week lead time across the domain. Combining with the 500 mb atmospheric regimes, certain forecasts of opportunity become clear, particularly for regimes that are already associated with high or near normal heat wave rates. For example, in the Southern USGP Regime 5 has several phases with with lead times of >14 days where the historical heat wave rates exceed 30%, Regime 6 may reach nearly 25% and Regime 8, which is near normal, has some periods with higher heat wave probabilities (e.g. about 20% from 20-25 days

lag during phase 2). In the Northern USGP there is an associated peak in Regime 2, following the same pattern of appearing at longer lag times in MJO phase 2 and becoming earlier as the MJO phases increase, which is consistent with the increase in heat wave rates under regime 2 in the northern USGP. As with the heat wave rates for specific regimes, the USGP experiences a combination of the northern and central USGP conditions.

Combining the three predictors, the MJO, ENSO, and the 500 mb atmospheric regime, compounds the predictability of each predictor. For certain combinations of these predictors and lag times the observed WBGT heat wave rate has exceeded 50% even for lag of up to 20 days, providing clear forecasts of opportunity. For example, in the Southern USGP during El Niño conditions and MJO phases 4-6, Regime 5 has peak heat wave rates between days 10-20 depending on MJO phase between 50 and 55%, and up to 60% at day 28 during MJO phase 7. During La Niña the peaks tend to be smaller, but more regimes have peaks. Regime 8 has a maximum heat wave rate of 40-45% around days 16-17 after MJO phase 1 while regimes 2, 5, and 6 all have notable periods under certain phases as well. The key takeaway is that while each predictor on its own has had various levels of success at discriminating between heat waves, combining all three allows for significantly more discrimination between high probability and low probability heat wave cases.

One challenge presented in the study, however, is that in order for the regime component to be useful in heat wave forecasting, it is necessary to be able to accurately forecast the regime in advance. Unfortunately, skill in models at predicting the regime decreases rapidly, to just 25% accuracy after 2 weeks and 10-15% accuracy by 3 weeks. While it may be possible to use these models to constrain the results, potential forecasts of opportunity will be damped by uncertainty in the regime.

Chapter 4

Discussion and Conclusions

This dissertation discusses WBGT heat wave climatology, trends, and sources of predictability, with a hypothesis that they will behave in similar ways to temperature based heat waves due to the high correlation between WBGT and temperature. Because WBGT incorporates factors other than temperature there could be differences in prediction which should largely be associated with events that have high humidity with relatively normal temperatures. However, previous work has not analyzed WBGT heat waves in the USGP. Understanding the behaviour of WBGT heat waves will help a variety of planners, emergency managers, health care facilities, and those maintaining infrastructure to be able to best respond to those events most likely to cause disruption and negative human health impacts.

In this study heat waves are defined using WBGT in the USGP, and analyzes the daily and annual climatology and trends in WBGT and the associated heat waves for two different methods of calculating WBGT from ERA5 reanalysis, as well as analyzing several sources of predictability for the prediction of WBGT heat waves in the USGP. Previous studies, particularly in the USGP, focus on defining extreme heat and heat waves using temperature or a more basic humid-heat approach. A few key takeaways are highlighted in the following paragraphs.

WBGT calculated from Dimicelli T_{bg} and NWS T_{nwb} has a smaller diurnal cycle than WBGT calculated from Liljegren WBGT. As a result Liljegren WBGT suggests a higher heat risk during the day than Dimicelli WBGT, however this study does not

compare either to direct observations of WBGT so no claim is made as to which is more accurate in the USGP. Otherwise, the two formulations perform similarly. This result will allow those using modeled WBGT to monitor heat stress to be aware of potential caveats associated with the model they are using.

The maximum WBGT heat risk throughout the year occurs in July and August, with higher risks further south and east, where summertime WBGTs regularly extend into the moderate category or higher. This is in line with the overall hypothesis of this work, as this is when temperature is typically highest in the USGP. During these months with the highest heat risk, it is advisable that high intensity outdoor work be scheduled to occur outside of the warmest parts of the day when at all possible, and to pay attention to forecasts and reschedule or postpone work when a heat wave is anticipated.

During DJF and portions of the transition seasons of SON and MAM the heat risk categories have historically been in the no risk category across the domain. However, WBGT is increasing faster during these periods than during the warm season which could result in more risks occurring outside of the months that are shown in this study should those trends continue. As discussed in chapter 2 similar behavior occurs in temperature trends. During the warm season, the higher risks that an area sees are becoming more frequent while the no risk categories have become less frequent since 1960.

WBGT heat waves are more common in the southern and eastern portions of the USGP. Using mean WBGT to define heat waves rather than maximum WBGT results in longer heat waves and more heat wave days. Additionally, the trend in the number of heat waves and heat waves days is generally positive and strongest in mean and minimum WBGT definitions, which has been seen previously with temperature (Perkins 2015; Oswald 2018). Understanding the characteristics of heat waves and their trends

will help emergency managers know what to expect when a heat wave is in the forecast for their area, and how often to expect a heat wave.

Dividing the atmosphere into multiple regimes based on detrended 500 mb geopotential height standardized anomalies shows regimes that place positive anomalies over a region are typically more likely to produce a WBGT heat wave than those that do not. In the USGP Regimes 2, 5, and 6 are the primary regimes associated with WBGT heat waves, with Regime 2 having positive geopotential anomalies over the Northern USGP, while Regimes 5 and 6 are associated with positive geopotential anomalies over the Southern USGP. This is in agreement with studies based on temperature based heat waves, which have shown that heat waves are typically associated with high pressure, particularly blocking highs (e.g. Perkins 2015). Conversely, negative geopotential anomalies are typically associated with reduced WBGT heat wave rates, for example Regimes 0, 1, 3, and 7. Our Regimes 0 and 3 are the same regimes as the Arctic High and Alaskan Ridge from Millin et al. (2022), which accounted for 80% of cold snaps in the USGP in their study, with WCR (our Regime 7) accounting for the remaining 20%. Further, certain regimes are conducive to different types of heat waves, with Regimes 5 and 6, which have positive geopotential anomalies over the Central and Southern USGP producing different types of heat waves. Regimes 5 and 6 are both resemble Rossby wave trains over North America, but Regime 5 locates the positive anomalies largely east of the USGP, which supports surface advection of humid air from the Gulf of Mexico into the USGP leading to warm-humid heat waves, while Regime 6 locates the positive geopotential anomalies over and west of the USGP, which supports advection of hot, dry air from the deserts of Mexico and the Southwestern United States leading to hot-dry heat waves. Because Regime 5 heat waves are often driven by moisture, many events may be missed by temperature based heat wave analysis, but may still be identified when using other humid-heat based heat wave analysis.

Teleconnections with the tropics in the form of the MJO and ENSO provide sources of heat wave predictability. During El Niño conditions there tend to be fewer heat waves in the sourthern and central USGP, and more heat waves in the northern USGP, while La Niña tends to produce more heat waves in the southern and central USGP but fewer heat waves in the northern USGP, which is in line with the typical understanding of ENSO impacts on temperature For the MJO it is common for phases 3-6 to produce heat waves around 2-3 weeks after the phase occurs, with phases 3-4 occurring at lead times closer to 3 weeks while phases 5-6 closer to 2 weeks in advance. Generally the impact of the MJO phase or ENSO phase alone will only increase or decrease heat wave rates by a factor of 1.5 times the baseline rate, which varies from 7 to 9% across the domain. It is likely that the progression of maximum heat wave probabilities to shorter lag times as the phase number of the MJO increases is an artifact of specific phases creating the conditions for enhanced heat wave probabilities and then the MJO phase progressing eastward (which have higher numbers).

Combining the regimes at various lag times following the ENSO phase or MJO phase allows for much more spread in the heat wave rate, with rates up to 30%, which is more than 3 times the baseline rate. Combining the ENSO phases and MJO phases with each other and with the atmospheric regimes further increases these peak rates to more than 50% in some cases, or more than 10 times the baseline rates. Generally, peak heat wave rates occur with Regimes 5 and 6, Regime 2 in the North, and all three in the central as those are generally associated with enhanced heat wave rates in isolation, as well as regimes such as Regime 8, which has near normal heat wave rates but has specific combinations of MJO and ENSO phases that are associated with higher than normal heat wave rates at certain lag times. These combinations that have higher WBGT heat wave rates will provide forecasts of opportunity that will benefit anyone who has an interest in heat wave forecasts. They will assist forecasters

in identifying certain periods with extreme heat at lead times of two or more weeks; and emergency managers, medical facilities, and anyone scheduling outdoor work will be able to prepare further in advance with higher confidence when these forecasts of opportunity arise.

A limitation for forecasting purposes is that because the future atmospheric regimes are unknown, incorporating the regime requires a forecast of the regime. However, the model analyzed in this study, the ECMWF S2S model, is unable to forecast the correct regime with high accuracy at extended lead times. The model may reasonably be used to constrain the regimes for the first 1-2 weeks, but after that may not be reliable enough to take full advantage of the enhanced discrimination in heat wave probabilities provided by incorporating regimes beyond this time. It is possible that this accuracy is diminished in part due to the processing of the model output to put into the K-Means model. Since the model climatology is used to standardize the model output, differences may arise, particularly for days that are not highly correlated with a single regime. Without factoring the regimes into the historical heat wave rates, the maximum forecasts are still around 2x the baseline heatwave rates, which still provides a forecast of opportunity at lead times > 2 weeks, but not nearly as confident as a forecast that includes the atmospheric regimes. Therefore, it should be of high importance to improve the ability to correctly forecast the atmospheric regimes at > 2 weeks to take full advantage of the predictability provided by incorporating the regimes. Additionally, the statistical model to predict WBGT heat wave occurrences presented in section 3.3.5 needs refinement. Some refinements could include further breaking down the heat wave rates by season, bias correcting forecast ensemble regime counts, averaging over a several day and several grid point area, or incorporating more sophisticated machine learning elements. However, it is possible that in some cases these refinements may introduce problems with sample size.

As heat waves have different impacts during the summer and winter, future work may need to reevaluate the use of the term heat wave for events during the winter. These winter warm periods will typically be perceived as mild conditions due to the much colder climatological temperatures during this period, and are much less likely to directly lead to negative human health outcomes. As such, it may be confusing to some to continue using the term heat wave for cold season events. Further, It may be of interest in future work to isolate the seasonality of WBGT heat wave characteristics and predictive skill in order to ensure that they are properly evaluating those events most likely to negatively impact human health. For example, with WBGT increasing faster during the winter than the summer, despite generally lower wintertime heat wave rates, the wintertime heat waves could be influencing the trend in heat wave characteristics, particularly in the Northern USGP where the wintertime WBGT trends are largest.

Overall, this study extends our understanding of extreme heat and heat waves to WBGT and discusses several sources of predictability for WBGT heat waves. Broadly speaking WBGT climatology and heat wave extremes and predictive skill are in agreement with those seen for temperature. Extreme heat is generally increasing in frequency across the USGP and WBGT is increasing fastest in winter, as well as with minimum and mean WBGT heat wave days and WBGT heat wave frequency. Using a combination of atmospheric regime, MJO phase, and ENSO phase, it is possible to identify forecasts of opportunity where a heat wave is considerably more likely to occur than on a typical day. During Regime 5, the dominant heat wave type in the Southern USGP is warm-humid, which may help provide an example of a case where WBGT captures the full impact of what causes heat better than temperature alone. However, there is difficulty in accurately forecasting the atmospheric regimes beyond 2 weeks, which may limit the ability to take full advantage of the atmospheric regimes. Despite this, there

is still potentially useful predictability beyond 2 weeks associated with the ENSO and MJO.

Reference List

Ahn, Y., C. Tuholske, and R. M. Parks, 2024: Comparing Approximated Heat Stress Measures Across the United States. *GeoHealth*, **8 (1)**, 1–18, https://doi.org/10.1029/2023GH000923.

Ahn, Y., C. K. Uejio, J. Rennie, and L. Schmit, 2022: Verifying Experimental Wet Bulb Globe Temperature Hindcasts Across the United States. *GeoHealth*, **6 (4)**, 1–19, https://doi.org/10.1029/2021GH000527.

Anderson, G. B., and M. L. Bell, 2011: Heat waves in the United States: Mortality risk during heat waves and effect modification by heat wave characteristics in 43 U.S. communities. *Environmental Health Perspectives*, **119 (2)**, 210–218, https://doi.org/10.1289/ehp.1002313.

Barnston, A. G., M. Chelliah, and S. B. Goldenberg, 1997: Documentation of a Highly ENSO-Related SST Region in the Equatorial Pacific. *Atmosphere-Ocean*, **35 (3)**, 367–383.

Behera, S., J. V. Ratnam, Y. Masumoto, and T. Yamagata, 2013: Origin of extreme summers in Europe: The Indo-Pacific connection. *Climate Dynamics*, **41 (3-4)**, 663–676, https://doi.org/10.1007/s00382-012-1524-8.

Bekryaev, R. V., I. V. Polyakov, and V. A. Alexeev, 2010: Role of polar amplification in long-term surface air temperature variations and modern arctic warming. *Journal of Climate*, **23 (14)**, 3888–3906, https://doi.org/10.1175/2010JCLI3297.1.

Brock, F. V., K. C. Crawford, R. L. Elliott, G. W. Cuperus, S. J. Stadler, H. L. Johnson, and M. D. Eilts, 1995: The Oklahoma Mesonet: A Technical Overview. *Journal of Atmospheric and Oceanic Technology*, **12 (2)**, 5–19.

Büeler, D., L. Ferranti, L. Magnusson, J. F. Quinting, and C. M. Grams, 2021: Year-round sub-seasonal forecast skill for Atlantic–European weather regimes. *Quarterly Journal of the Royal Meteorological Society*, **147 (741)**, 4283–4309, https://doi.org/10.1002/qj.4178.

Buzan, J. R., K. Oleson, and M. Huber, 2015: Implementation and comparison of a suite of heat stress metrics within the Community Land Model version 4.5. *Geoscientific Model Development*, **8 (2)**, 151–170, https://doi.org/10.5194/gmd-8-151-2015.

Collins, M., and Coauthors, 2013: *Long-term Climate Change: Projections, Commitments and Irreversibility, Climate Change 2013: The Physical Science Basis. Contribution of Working Group I to the Fifth Assessment Report of the Intergovernmental Panel on Climate Change*. Cambridge University Press, 1029–1136 pp.

Departments of Army and Air Force, 2003: Heat Stress Control and Heat Casualty Management. *Tech Bull Med 507 air force Pamphlet*, **48e152(I)**.

Dimiceli, V. E., S. F. Piltz, and S. A. Amburn, 2011: Estimation of Black Globe Temperature for Calculation of the Wet Bulb Globe Temperature Index. *Proceedings of the World Congress on Engineering and Computer Science*, San Francisco, CA, USA, Vol. II, URL https://www.weather.gov/media/tsa/pdf/WBGTpaper2.pdf.

Domeisen, D. I., and Coauthors, 2023: Prediction and projection of heatwaves. *Nature Reviews Earth and Environment*, **4 (1)**, 36–50, https://doi.org/10.1038/s43017-022-00371-z.

Epstein, Y., and D. S. Moran, 2006: Thermal comfort and the heat stress indices. *Industrial Health*, **44 (3)**, 388–398, https://doi.org/10.2486/indhealth.44.388.

García-Herrera, R., J. M. Garrido-Perez, and C. Ordóñez, 2022: Modulation of European air quality by Euro-Atlantic weather regimes. *Atmospheric Research*, **277 (March)**, https://doi.org/10.1016/j.atmosres.2022.106292.

Garrido-Perez, J. M., C. Ordóñez, D. Barriopedro, R. García-Herrera, and D. Paredes, 2020: Impact of weather regimes on wind power variability in western Europe. *Applied Energy*, **264 (August 2019)**, 114 731, https://doi.org/10.1016/j.apenergy.2020.114731, URL https://doi.org/10.1016/j.apenergy.2020.114731.

Grundstein, A., C. Williams, M. Phan, and E. Cooper, 2015: Regional heat safety thresholds for athletics in the contiguous United States. *Applied Geography*, **56**, 55–60, https://doi.org/10.1016/j.apgeog.2014.10.014, URL http://dx.doi.org/10.1016/j.apgeog.2014.10.014.

Hajat, S., R. S. Kovats, R. W. Atkinson, and A. Haines, 2002: Impact of hot temperatures on death in London: a time series approach. *Journal of Epidemiology and Community Health*, **56**, 367.

Heo, S., M. L. Bell, and J.-T. Lee, 2019: Comparison of health risks by heat wave definition: Applicability of wet-bulb globe temperature for heat wave criteria. *Environmental Research*, **168 (1)**, https://doi.org/https://doi.org/10.1016/j.envres.2018.09.032, URL https://www.sciencedirect.com/science/article/abs/pii/S0013935118305188.

Hersbach, H., and Coauthors, 2018: ERA5 hourly data on single levels from 1959 to present. Copernicus Climate Change Service (C3S) Climate Data Store (CDS)., https://doi.org/10.24381/cds.adbb2d47.

Hoerling, M., J. Eischeid, A. Kumar, R. Leung, A. Mariotti, K. Mo, S. Schubert, and R. Seager, 2014: Causes and predictability of the 2012 great plains drought. *Bulletin of the American Meteorological Society*, **95 (2)**, 269–282, https://doi.org/10.1175/BAMS-D-13-00055.1.

Hoerling, M., and Coauthors, 2013: Anatomy of an extreme event. *Journal of Climate*, **26 (9)**, 2811–2832, https://doi.org/10.1175/JCLI-D-12-00270.1.

Hunter, C. H., and C. O. Minyard, 1999: ESTIMATING WET BULB GLOBE TEMPERATURE USING STANDARD METEOROLOGICAL MEASUREMENTS. *Proceedings of the Conference: 2nd Conference on Environmental Applications*, Long Beach, CA, USA, 7.

Hyatt, O. M., B. Lemke, and T. Kjellstrom, 2010: Regional maps of occupational heat exposure: past, present, and potential future. *Global Health Action*, **3 (1)**, 5715, https://doi.org/10.3402/gha.v3i0.5715.

Karl, T. R., and R. W. Knight, 1997: The 1995 Chicago Heat Wave: How Likely Is a Recurrence? *Bulletin of the American Meteorological Society*, **78 (6)**, 1107–1119, https://doi.org/10.1175/1520-0477(1997)078⟨1107:TCHWHL⟩2.0.CO;2.

Kenyon, J., and G. C. Hegerl, 2008: Influence of modes of climate variability on global temperature extremes. *Journal of Climate*, **21 (15)**, 3872–3889, https://doi.org/10.1175/2008JCLI2125.1.

Knutson, T. R., and J. J. Ploshay, 2016: Detection of anthropogenic influence on a summertime heat stress index. *Climatic Change*, **138 (1-2)**, 25–39, https://doi.org/10.1007/s10584-016-1708-z, URL http://dx.doi.org/10.1007/s10584-016-1708-z.

Kong, Q., and M. Huber, 2022: Explicit Calculations of Wet-Bulb Globe Temperature Compared With Approximations and Why It Matters for Labor Productivity Earth ' s Future. *Earth's Future*, **10**, 1–21, https://doi.org/10.1029/2021EF002334.

Koster, R. D., Z. Guo, R. Yang, P. A. Dirmeyer, K. Mitchell, and M. J. Puma, 2009: On the nature of soil moisture in land surface models. *Journal of Climate*, **22 (16)**, 4322–4335, https://doi.org/10.1175/2009JCLI2832.1.

Krishnamurthy, R., R. K. Newsom, D. Chand, and W. J. Shaw, 2021: Boundary Layer Climatology at ARM Southern Great Plains. Tech. Rep. January, Pacific Northwest National Laboratory, 101 pp.

Kunkel, K. E., S. A. Changnon, B. C. Reinke, and R. W. Arritt, 1996: The July 1995 heat wave in the midwest: A climatic perspective and critical weather factors. *Bulletin of the American Meteorological Society*, **77 (7)**, 1507–1518, https://doi.org/10.1175/1520-0477(1996)077⟨1507:TJHWIT⟩2.0.CO;2.

Lee, S. H., J. C. Furtado, and A. J. Charlton-Perez, 2019: Wintertime North American Weather Regimes and the Arctic Stratospheric Polar Vortex. *Geophysical Research Letters*, **46 (24)**, 14 892–14 900, https://doi.org/10.1029/2019GL085592.

Lee, S. H., M. K. Tippett, and L. M. Polvani, 2023: A New Year-Round Weather Regime Classification for North America. *Journal of Climate*, **36 (20)**, 7091–7108, https://doi.org/10.1175/JCLI-D-23-0214.1.

Lee, Y. Y., and R. Grotjahn, 2019: Evidence of Specific MJO Phase Occurrence with Summertime California Central Valley Extreme Hot Weather. *Advances in Atmospheric Sciences*, **36 (6)**, 589–602, https://doi.org/10.1007/s00376-019-8167-1.

Lesk, C., W. Anderson, A. Rigden, O. Coast, J. Jägermeyr, and S. Mcdermid, 2022: Compound heat and moisture extreme impacts on global crop yields under climate change. *Nature Reviews Earth and Environment*, **3 (December)**, https://doi.org/10.1038/s43017-022-00368-8.

Li, C., X. Zhang, F. Zwiers, Y. Fang, and A. M. Michalak, 2017: Recent Very Hot Summers in Northern Hemispheric Land Areas Measured by Wet Bulb Globe Temperature Will Be the Norm Within 20 Years. *Earth's Future*, **5 (12)**, 1203–1216, https://doi.org/10.1002/2017EF000639.

Li, D., J. Yuan, and R. E. Kopp, 2020: Escalating global exposure to compound heat-humidity extremes with warming. *Environmental Research Letters*, **15 (6)**, https://doi.org/10.1088/1748-9326/ab7d04.

Liljegren, J. C., R. A. Carhart, P. Lawday, S. Tschopp, and R. Sharp, 2008: Modeling the wet bulb globe temperature using standard meteorological measurements. *Journal of Occupational and Environmental Hygiene*, **5 (10)**, 645–655, https://doi.org/10.1080/15459620802310770.

Lin, H., and R. Mo, 2022: The 2021 Western North American Heatwave and Its Subseasonal Predictions. *Geophysical Research Letters*, **49**, 1–10, https://doi.org/10.1029/2021GL097036.

Loikith, P. C., and A. J. Broccoli, 2014: The influence of recurrent modes of climate variability on the occurrence of winter and summer extreme temperatures over North America. *Journal of Climate*, **27 (4)**, 1600–1618, https://doi.org/10.1175/JCLI-D-13-00068.1.

Lopez, H., S. K. Lee, S. Dong, G. Goni, B. Kirtman, R. Atlas, and A. Kumar, 2019: East Asian Monsoon as a Modulator of U.S. Great Plains Heat Waves. *Journal of Geophysical Research: Atmospheres*, **124 (12)**, 6342–6358, https://doi.org/10.1029/2018JD030151.

Luo, M., and N. C. Lau, 2020: Summer heat extremes in northern continents linked to developing ENSO events. *Environmental Research Letters*, **15 (7)**, https://doi.org/10.1088/1748-9326/ab7d07.

Madden, R. A., and P. R. Julian, 1971: Detection of a 40-50 Day Oscillation in the Zonal Wind in the Tropical Pacific. *Journal of the Atmospheric Sciences*, **28 (5)**, 32, https://doi.org/https://doi.org/10.1175/1520-0469(1971)028⟨0702:DOADOI⟩2.0.CO;2.

Madden, R. A., and P. R. Julian, 1972: Description of Global-Scale Circulation Cells in the Tropics with a 40-50 Day Period. *Journal of the Atmospheric Sciences*, **29 (6)**, 1109–1123.

Matthew, W. T., W. R. Santee, and L. G. Berglund, 2001: Solar Load Inputs for Usariem Thermal Strain Models and the Solar Radiation-Sensitive Components of the Wbgt Index. Tech. Rep. June, U.S. Army Research Institute of Environmental Medicine, Natick, MA. URL https://apps.dtic.mil/sti/citations/ADA392480.

McAllister, C., A. Stephens, and S. M. Milrad, 2022: The Heat Is On: Observations and Trends of Heat Stress Metrics during Florida Summers. *Journal of Applied Meteorology and Climatology*, **61 (3)**, 277–296, https://doi.org/10.1175/JAMC-D-21-0113.1.

McPherson, R. A., and Coauthors, 2007: Statewide monitoring of the mesoscale environment: A technical update on the Oklahoma Mesonet. *Journal of Atmospheric and Oceanic Technology*, **24 (3)**, 301–321, https://doi.org/10.1175/JTECH1976.1.

Meehl, G. A., J. M. Arblaster, and G. Branstator, 2012: Mechanisms contributing to the warming hole and the consequent U.S. East-west differential of heat extremes. *Journal of Climate*, **25 (18)**, 6394–6408, https://doi.org/10.1175/JCLI-D-11-00655.1.

Meehl, G. A., and C. Tebaldi, 2004: More intense, more frequent, and longer lasting heat waves in the 21st century. *Science*, **305 (5686)**, 994–997, https://doi.org/10.1126/science.1098704.

Millin, O. T., J. C. Furtado, and J. B. Basara, 2022: Characteristics, Evolution, and Formation of Cold Air Outbreaks in the Great Plains of the United States. *Journal of Climate*, **35 (14)**, 4585–4602, https://doi.org/10.1175/JCLI-D-21-0772.1.

Moon, J. Y., B. Wang, and K. J. Ha, 2011: ENSO regulation of MJO teleconnection. *Climate Dynamics*, **37 (5)**, 1133–1149, https://doi.org/10.1007/s00382-010-0902-3.

Mora, C., and Coauthors, 2017: Global risk of deadly heat. *Nature Climate Change*, **7 (July)**, https://doi.org/10.1038/NCLIMATE3322.

Nissan, H., K. Burkart, E. C. de Perez, M. Van Aalst, and S. Mason, 2017: Defining and predicting heat waves in Bangladesh. *Journal of Applied Meteorology and Climatology*, **56 (10)**, 2653–2670, https://doi.org/10.1175/JAMC-D-17-0035.1.

Oklahoma Mesonet, 2016: Wet Bulb Globe Temperature Category Work / Rest and Water Intake. Tech. rep., Oklahoma Climatological Survey, Norman, OK, 1–2 pp. URL http://www.mesonet.org/images/site/WBGT_Mesonet_Work_Rest_Info.May2016.pdf.

Ortizbeviá, M. J., E. Sánchezgómez, and F. J. Alvarez-García, 2011: North Atlantic atmospheric regimes and winter extremes in the Iberian peninsula. *Natural Hazards and Earth System Science*, **11 (3)**, 971–980, https://doi.org/10.5194/nhess-11-971-2011.

OSHA, 2017: OSHA Technical Manual, Section III: Chapter 4. Vol. 2013, OSHA, URL https://www.osha.gov/otm/section-3-health-hazards/chapter-4.

Oswald, E. M., 2018: An analysis of the prevalence of heat waves in the United States between 1948 and 2015. *Journal of Applied Meteorology and Climatology*, **57 (7)**, 1535–1549, https://doi.org/10.1175/JAMC-D-17-0274.1.

Parsons, K., 2006: Heat stress standard ISO 7243 and its global application. *Industrial Health*, **44 (3)**, 368–379, https://doi.org/10.2486/indhealth.44.368.

Patel, T., S. P. Mullen, and W. R. Santee, 2013: Comparison of methods for estimating Wet-Bulb Globe Temperature index from standard meteorological measurements. *Military Medicine*, **178 (8)**, 926–933, https://doi.org/10.7205/MILMED-D-13-00117.

Peng, R. D., J. F. Bobb, C. Tebaldi, L. McDaniel, M. L. Bell, and F. Dominici, 2011: Toward a quantitative estimate of future heat wave mortality under global climate change. *Environmental Health Perspectives*, **119 (5)**, 701–706, https://doi.org/10.1289/ehp.1002430.

Perkins, S. E., 2015: A review on the scientific understanding of heatwaves-Their measurement, driving mechanisms, and changes at the global scale. *Atmospheric Research*, **164-165**, 242–267, https://doi.org/10.1016/j.atmosres.2015.05.014, URL http://dx.doi.org/10.1016/j.atmosres.2015.05.014.

Perkins-Kirkpatrick, S. E., and P. B. Gibson, 2017: Changes in regional heatwave characteristics as a function of increasing global temperature. *Scientific Reports*, **7 (1)**, 1–12, https://doi.org/10.1038/s41598-017-12520-2, URL http://dx.doi.org/10.1038/s41598-017-12520-2.

Rennie, J. J., M. A. Palecki, S. P. Heuser, and H. J. Diamond, 2021: Developing and validating heat exposure products using the U.S. climate reference network. *Journal of Applied Meteorology and Climatology*, **60 (4)**, 543–558, https://doi.org/10.1175/JAMC-D-20-0282.1.

Robinson, P. J., 2001: On the definition of a heat wave. *Journal of Applied Meteorology*, **40 (4)**, 762–775, https://doi.org/10.1175/1520-0450(2001)040⟨0762:OTDOAH⟩2.0.CO;2.

Ropelewski, C. F., and M. S. Halpert, 1986: North American Precipitation and Temperature Patterns Associated with the El Nino/Southern Oscillation (ENSO). *Monthly Weather Review*, **114**, 2352–2362.

Schreck, C. J., J. M. Cordeira, and D. Margolin, 2013: Which MJO events affect north american temperatures? *Monthly Weather Review*, **141 (11)**, 3840–3850, https://doi.org/10.1175/MWR-D-13-00118.1.

Seager, R., L. Goddard, J. Nakamura, N. Henderson, and D. E. Lee, 2014: Dynamical causes of the 2010/11 Texas-northern Mexico drought. *Journal of Hydrometeorology*, **15 (1)**, 39–68, https://doi.org/10.1175/JHM-D-13-024.1.

Sherwood, S. C., and M. Huber, 2010: An adaptability limit to climate change due to heat stress. *Proceedings of the National Academy of Sciences of the United States of America*, **107 (21)**, 9552–9555, https://doi.org/10.1073/pnas.0913352107.

Smith, T. T., B. F. Zaitchik, and J. M. Gohlke, 2013: Heat waves in the United States: Definitions, patterns and trends. *Climatic Change*, **118 (3-4)**, 811–825, https://doi.org/10.1007/s10584-012-0659-2.

Spangler, K. R., S. Liang, and G. A. Wellenius, 2022: Wet-Bulb Globe Temperature , Universal Thermal Climate Index , and Other Heat Metrics for US Counties , 2000 – 2020. *Scientific Data*, **9**, 1–9, https://doi.org/10.1038/s41597-022-01405-3.

Steadman, R. G., 1979: The assessment of sultriness. Part II: effects of wind, extra radiation and barometric pressure on apparent temperature. *Journal of Applied Meteorology*, **18 (7)**, 874–885, https://doi.org/10.1175/1520-0450(1979)018⟨0874:TAOSPI⟩2.0.CO;2.

Steadman, R. G., 1984: A Universal Scale of Apparent Temperature. *Journal of Climate and Applied Meteorology*, **23**, 1674–1687.

Tan, J., Y. Zheng, G. Song, L. S. Kalkstein, A. J. Kalkstein, and X. Tang, 2007: Heat wave impacts on mortality in Shanghai, 1998 and 2003. *International Journal of Biometeorology*, **51 (3)**, 193–200, https://doi.org/10.1007/s00484-006-0058-3.

Teng, H., G. Branstator, G. A. Meehl, and W. M. Washington, 2016: Projected intensification of subseasonal temperature variability and heat waves in the Great Plains. *Geophysical Research Letters*, **43 (5)**, 2165–2173, https://doi.org/10.1002/2015GL067574.

Teng, H., G. Branstator, H. Wang, G. A. Meehl, and W. M. Washington, 2013: Probability of US heat waves affected by a subseasonal planetary wave pattern. *Nature Geoscience*, **6 (12)**, 1056–1061, https://doi.org/10.1038/ngeo1988.

Tian, D., E. F. Wood, and X. Yuan, 2017: CFSv2-based sub-seasonal precipitation and temperature forecast skill over the contiguous United States. *Hydrology and Earth System Sciences*, **21**, 1477–1490, https://doi.org/10.5194/hess-21-1477-2017.

Van Der Wiel, K., H. C. Bloomfield, R. W. Lee, L. P. Stoop, R. Blackport, J. A. Screen, and F. M. Selten, 2019: The influence of weather regimes on European renewable energy production and demand. *Environmental Research Letters*, **14 (9)**, https://doi.org/10.1088/1748-9326/ab38d3.

Vecellio, D. J., S. Tony Wolf, R. M. Cottle, and W. Larry Kenney, 2022: Evaluating the 35C wet-bulb temperature adaptability threshold for young, healthy subjects (PSU HEAT Project). *Journal of Applied Physiology*, **132 (2)**, 340–345, https://doi.org/10.1152/japplphysiol.00738.2021.

Vitart, F., and A. W. Robertson, 2018: The sub-seasonal to seasonal prediction project (S2S) and the prediction of extreme events. *npj Climate and Atmospheric Science*, **1 (1)**, 1–7, https://doi.org/10.1038/s41612-018-0013-0, URL http://dx.doi.org/10.1038/s41612-018-0013-0.

Vitart, F., A. W. Robertson, and S2S Steering Group, 2015: Sub-seasonal to seasonal prediction: Linking weather and climate. *Seamless Prediction of the Earth System: From Minutes to Months*, G. Brunet, S. Jones, and P. M. Ruti, Eds., WMO-1156, World Meteorological Organization, 385–401.

Vitart, F., and Coauthors, 2017: The subseasonal to seasonal (S2S) prediction project database. *Bulletin of the American Meteorological Society*, **98 (1)**, 163–173, https://doi.org/10.1175/BAMS-D-16-0017.1.

Vitart, F., and Coauthors, 2019: *Sub-seasonal to Seasonal Prediction of Weather Extremes*. Elsevier, Ch. 17 pp.

Wang, J., M. Deflorio, and F. M. Ralph, 2023: Modulation of western U . S . compound precipitation and temperature extremes by compounding MJO and ENSO interaction. *preprint*.

Yaglou, C. P., and D. Minard, 1957: Control of heat casualties at military training centers. *A.M.A. archives of industrial health*, **16 (4)**, 302–316.

1 Appendix A

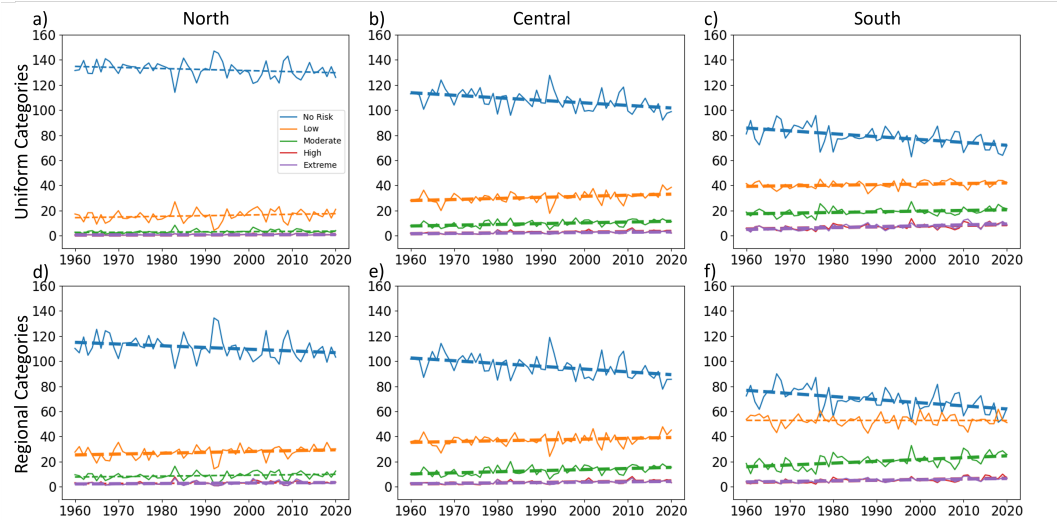

Figure A.1: Trend in number of MJJAS days with each daily maximum Liljegren WBGT category for uniform (a-c) and regional (d-f) categories for the northern (a,d), central (b,e), and southern (c,f) USGP. Dashed lines indicate the trend, with trends that are statistically significant at the 95% confidence level in bold.

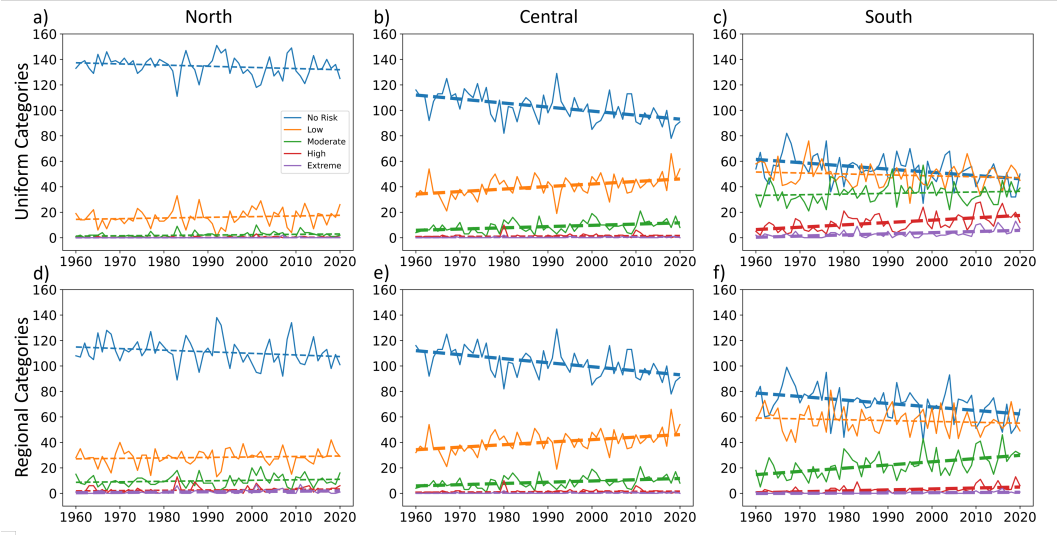

Figure A.2: Trend in number of MJJAS days with each daily maximum Dimiceli wet bulb globe temperature category for uniform (a-c) and regional (d-f) categories for the northern (a,d), central (b,e), and southern (c,f) USGP locations. Dashed lines indicate the trend, with trends that are statistically significant at the 95% confidence level in bold.

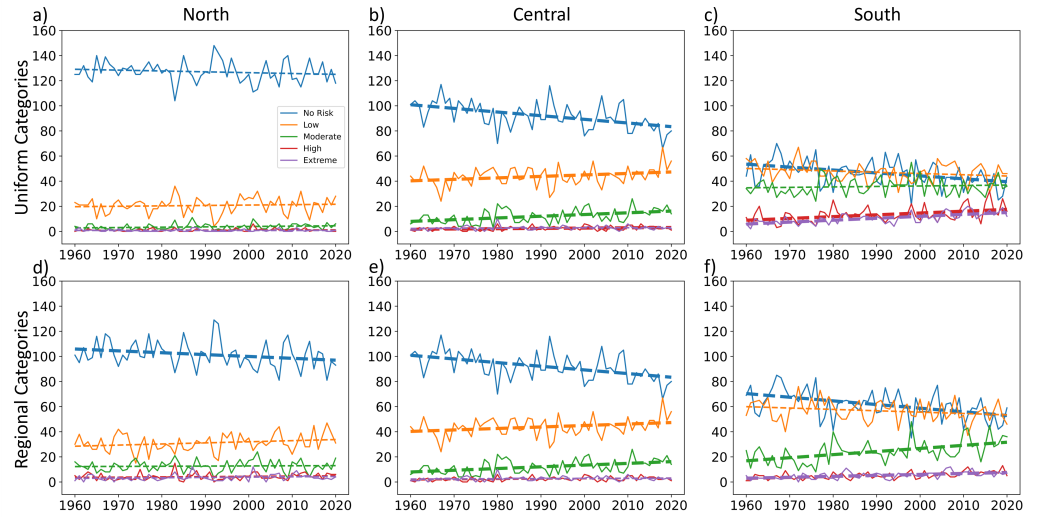

Figure A.3: Trend in number of MJJAS days with each daily maximum Liljegren WBGT category for uniform (a-c) and regional (d-f) categories for the northern (a,d), central (b,e), and southern (c,f) USGP. Dashed lines indicate the trend, with trends that are statistically significant at the 95% confidence level in bold.

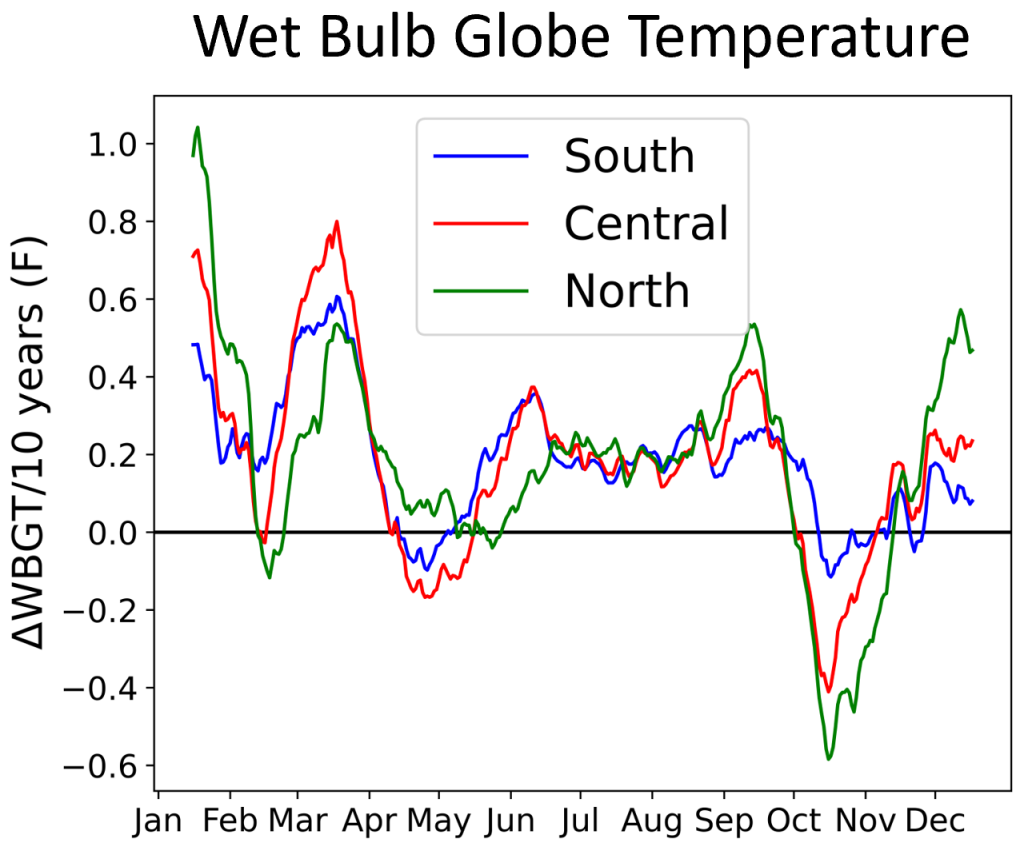

Figure A.4: Trend in 20 UTC Liljegren wet bulb globe temperature (WBGT) averaged across each subdomain.

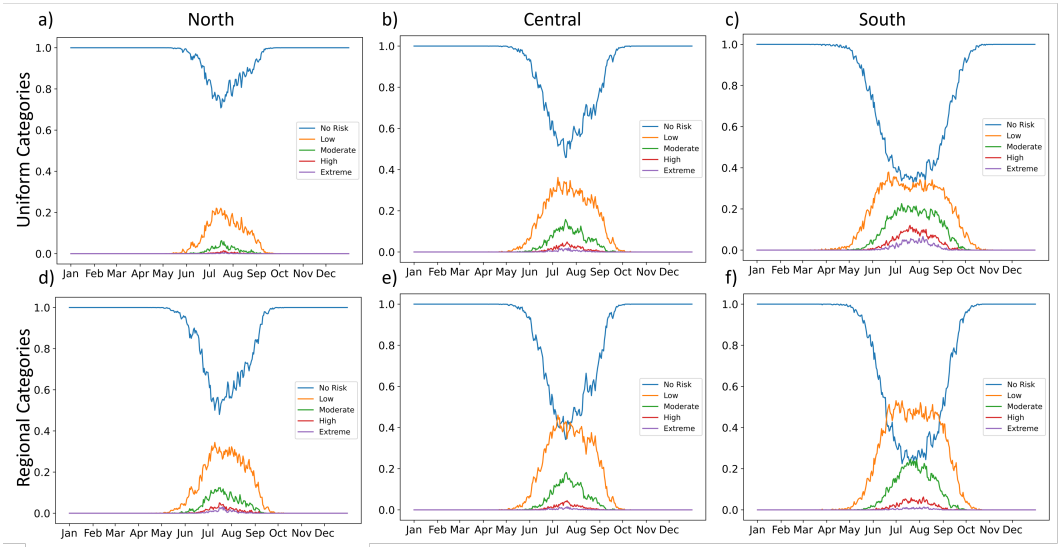

Figure A.5: Subdomain mean daily maximum Dimiceli wet bulb globe temperature category by relative frequency using a-c) uniform categories, d-f) regional categories, averaged over the a,d) northern, b,e) central, and c,f) southern USGP.

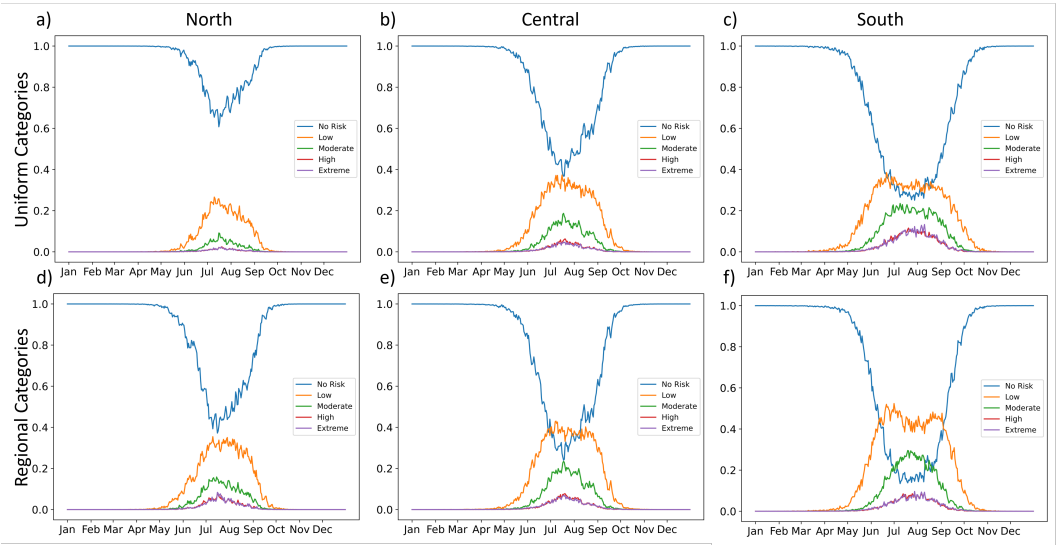

Figure A.6: Subdomain mean daily maximum Liljegren wet bulb globe temperature category by relative frequency using a-c) uniform categories, d-f) regional categories, averaged over the a,d) northern, b,e) central, and c,f) southern USGP.

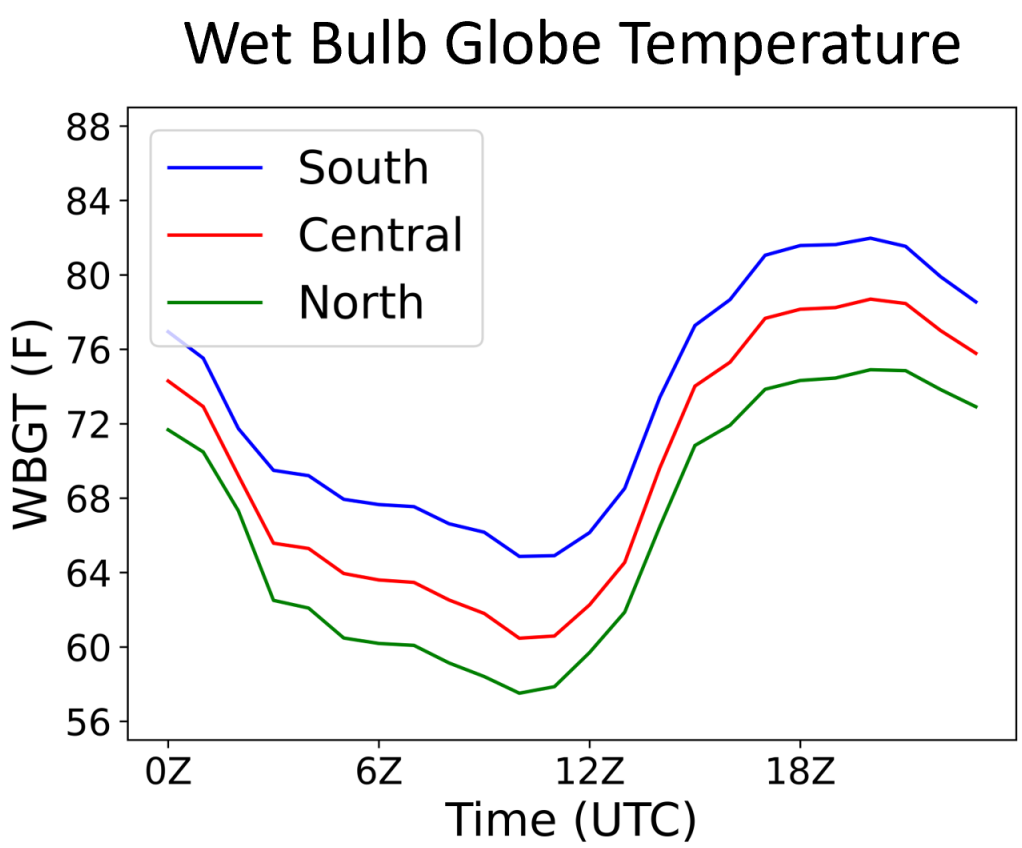

Figure A.7: July hourly mean of Liljegren wet bulb globe temperature (WBGT) representing the northern (green), central (red), and southern (blue) USGP subdomains.

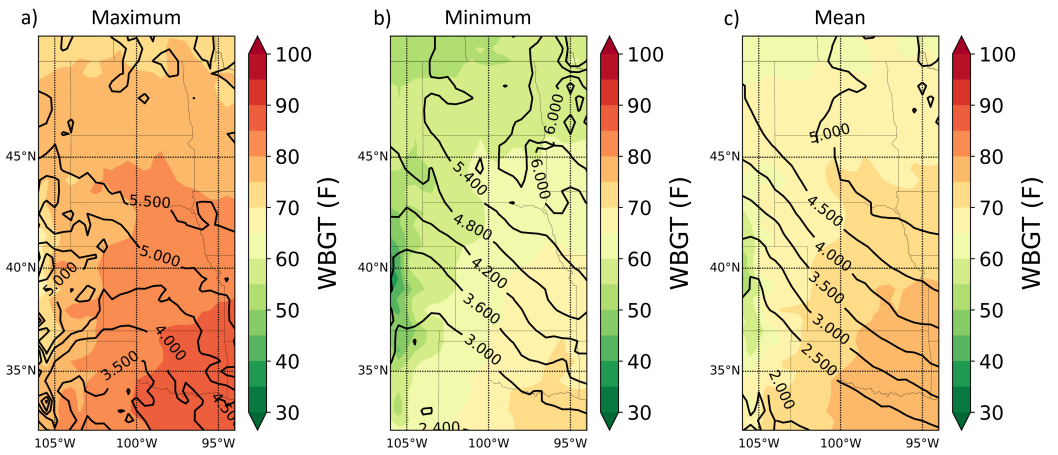

Figure A.8: Mean (filled contours) and Standard Deviation (contours) of July daily a) maximum, b) minimum, and c) mean Liljegren wet bulb globe temperature (WBGT).

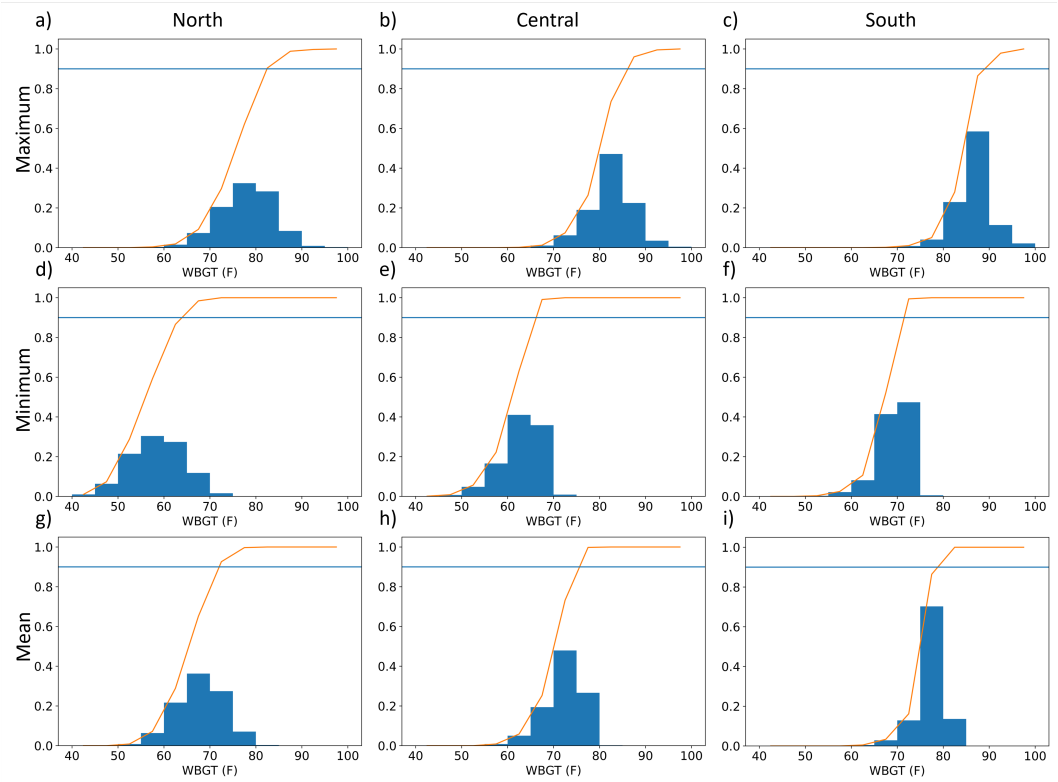

Figure A.9: Distribution of July daily a-c) maximum, d-f) minimum, and g-i) mean Liljegren wet bulb globe temperature (WBGT) for the a,d,g) Northern, b,e,h) Central, and c,f,i) Southern USGP. Cumulative distribution function in orange with the 90th percentile indicated by the blue horizontal line.

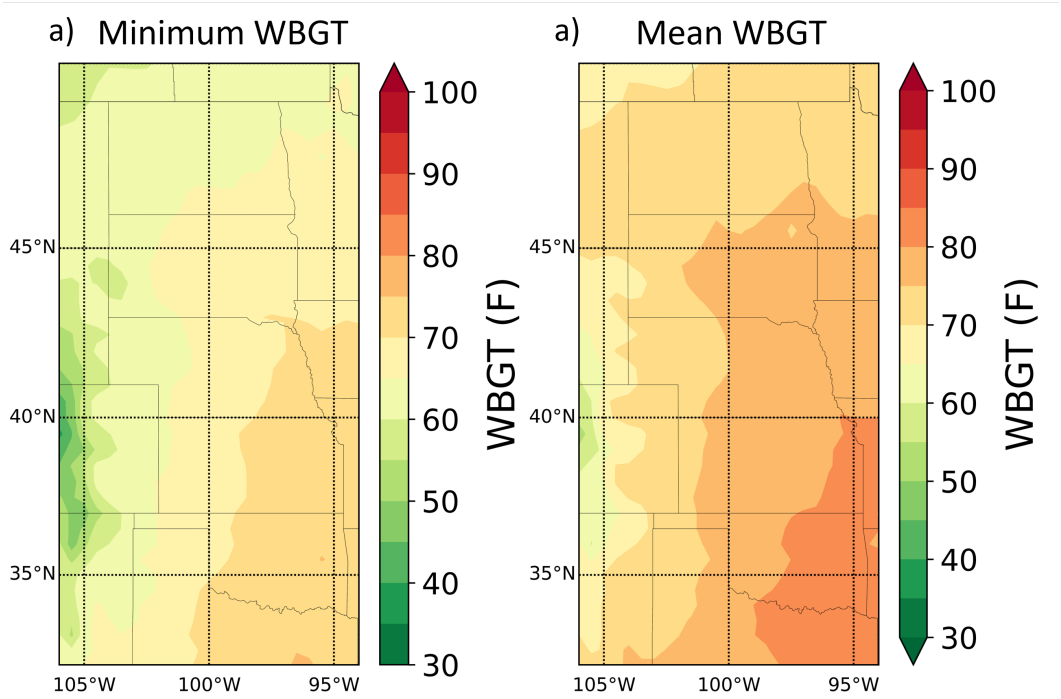

Figure A.10: July 16 31-day centered 90th percentile a) minimum Liljegren wet bulb globe temperature (WBGT), b) mean Liljegren WBGT.

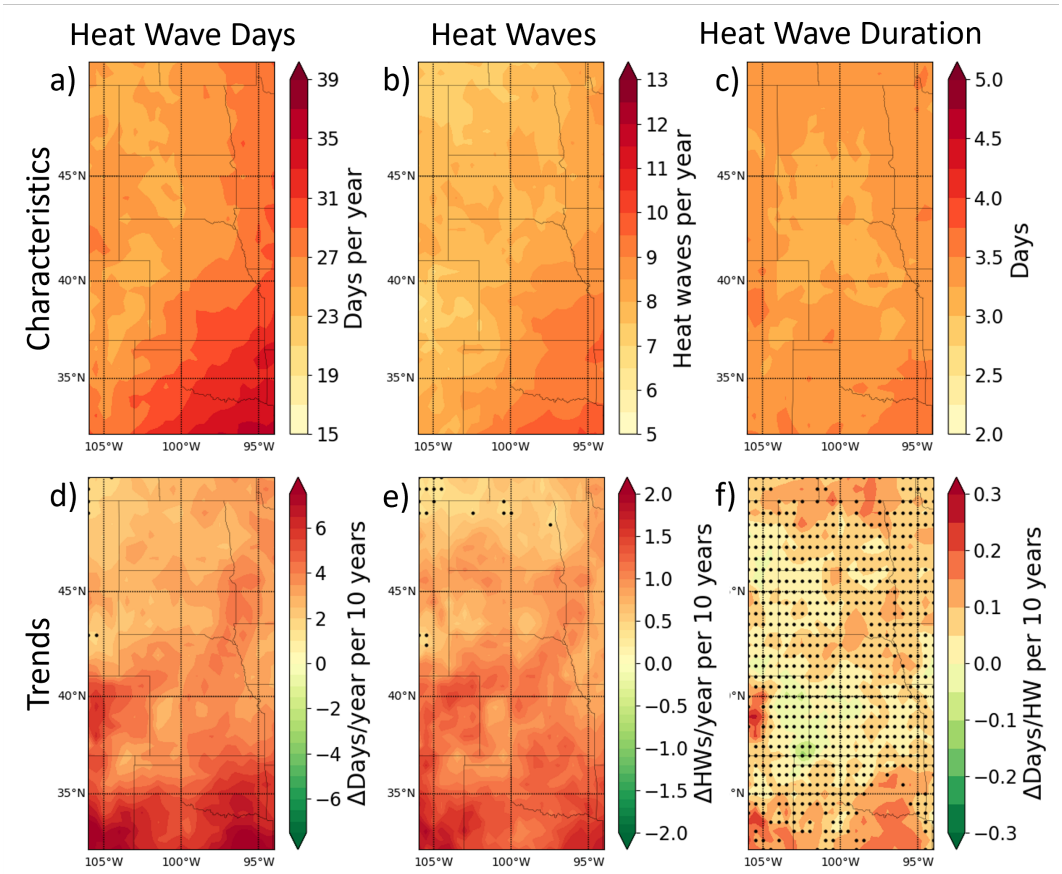

Figure A.11: Minimum a) number of heat wave days per year, b) heat waves per year, c) number of days per heat wave, and trend in d) number of heat wave days per year, e) heat waves per year, and f) number of days per heat wave. All panels use a heat wave definition based on minimum Liljegren WBGT. Black dots indicate trends that are not statistically significant at the 95% confidence level.

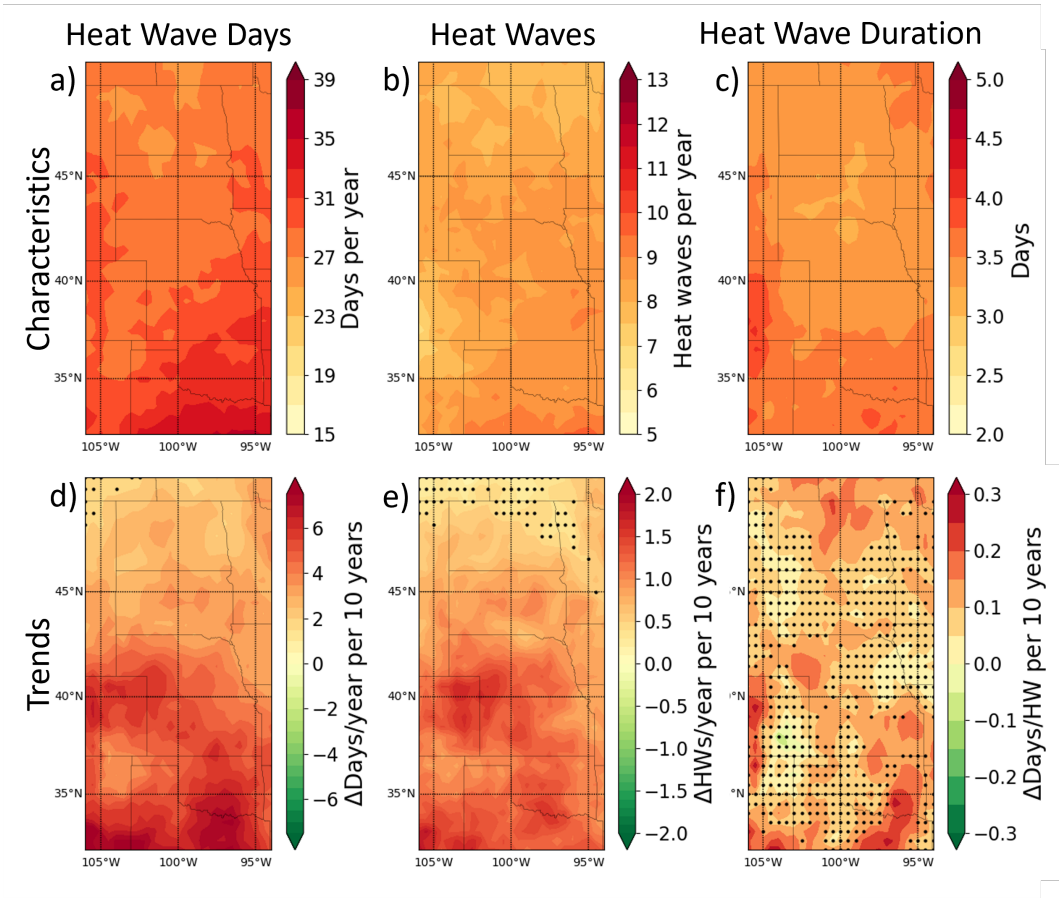

Figure A.12: Mean a) number of heat wave days per year, b) heat waves per year, c) number of days per heat wave, and trend in d) number of heat wave days per year, e) heat waves per year, and f) number of days per heat wave. All panels use a heat wave definition based on mean Liljegren WBGT. Black dots indicate trends that are not statistically significant at the 95% confidence level.

2 Appendix B

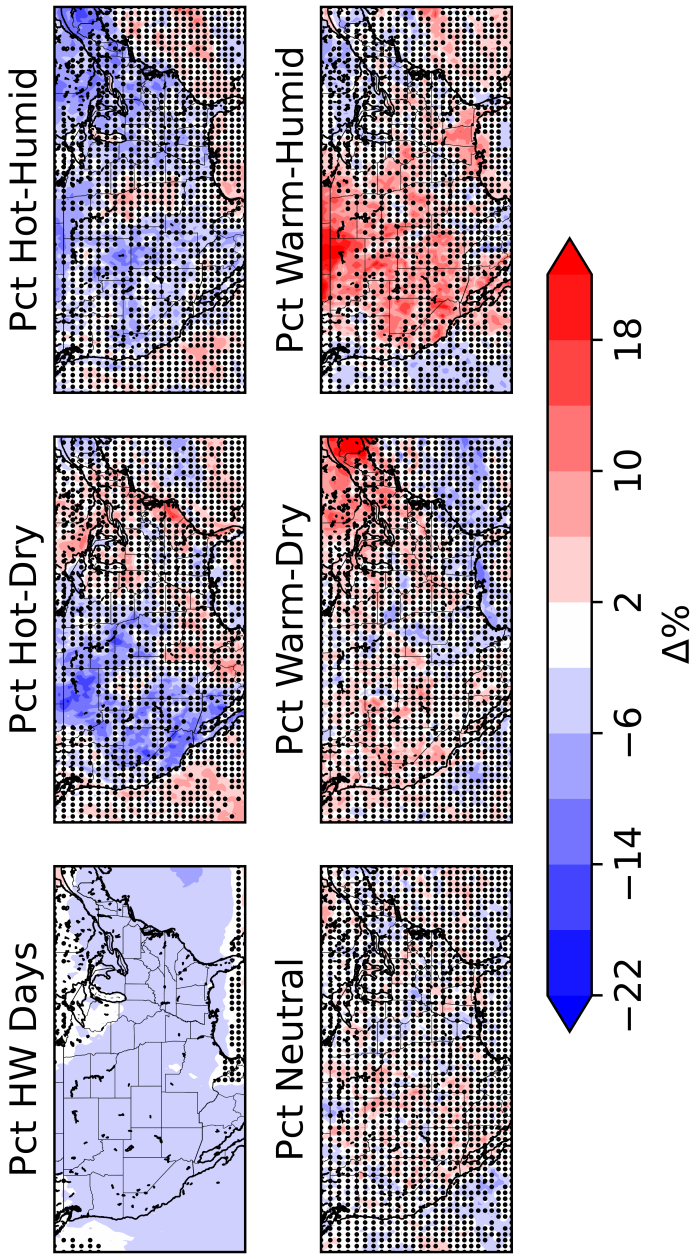

Figure B.1: a) Heat wave rate for Regime 0 minus all regimes, b) Percent of heat waves that are of type Hot-Dry for Regime 0 minus all regimes, c) Percentage of heat waves that are of type Hot-Humid minus all regimes, d) Percentage of heat waves that are of type Neutral minus all regimes, e) Percentage of heat waves that are of type Warm-Dry minus all regimes, f) Percentage of heat waves that are of type Warm-Humid minus all regimes. Dots indicate where the difference from the baseline heat wave rate is not statistically significant at the 95% confidence level.

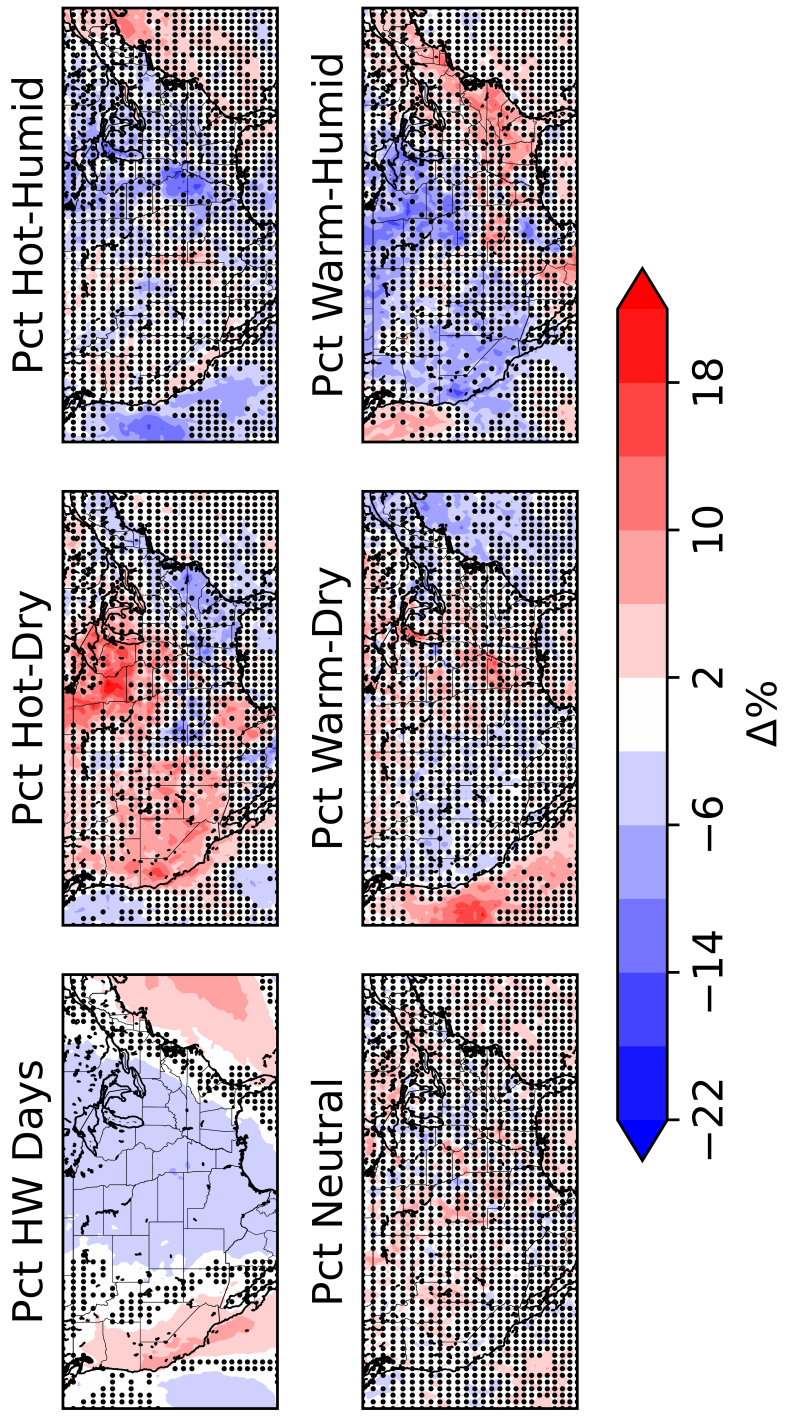

Figure B.2: As in B.1 but for Regime 1 minus all regimes.

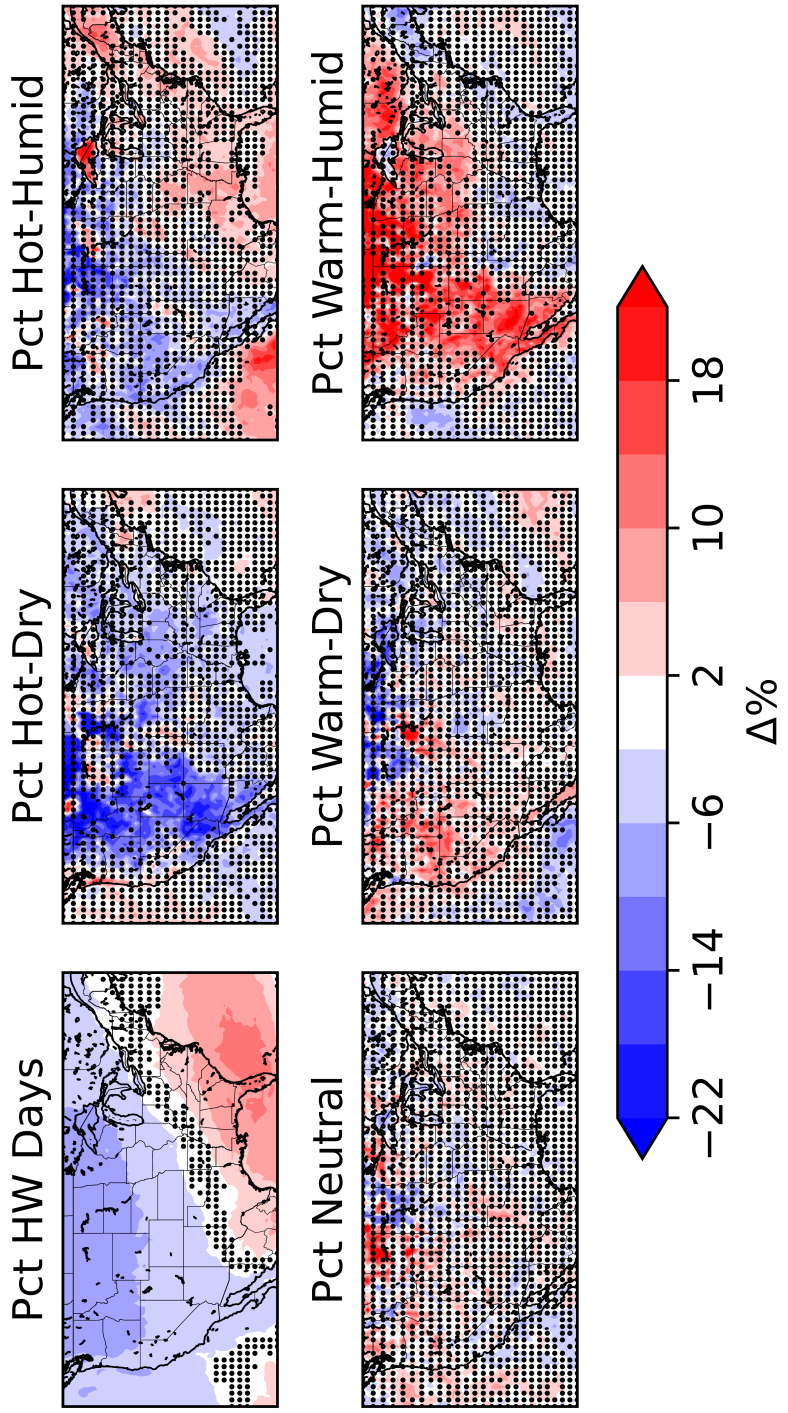

Figure B.3: As in B.1 but for Regime 3 minus all regimes.

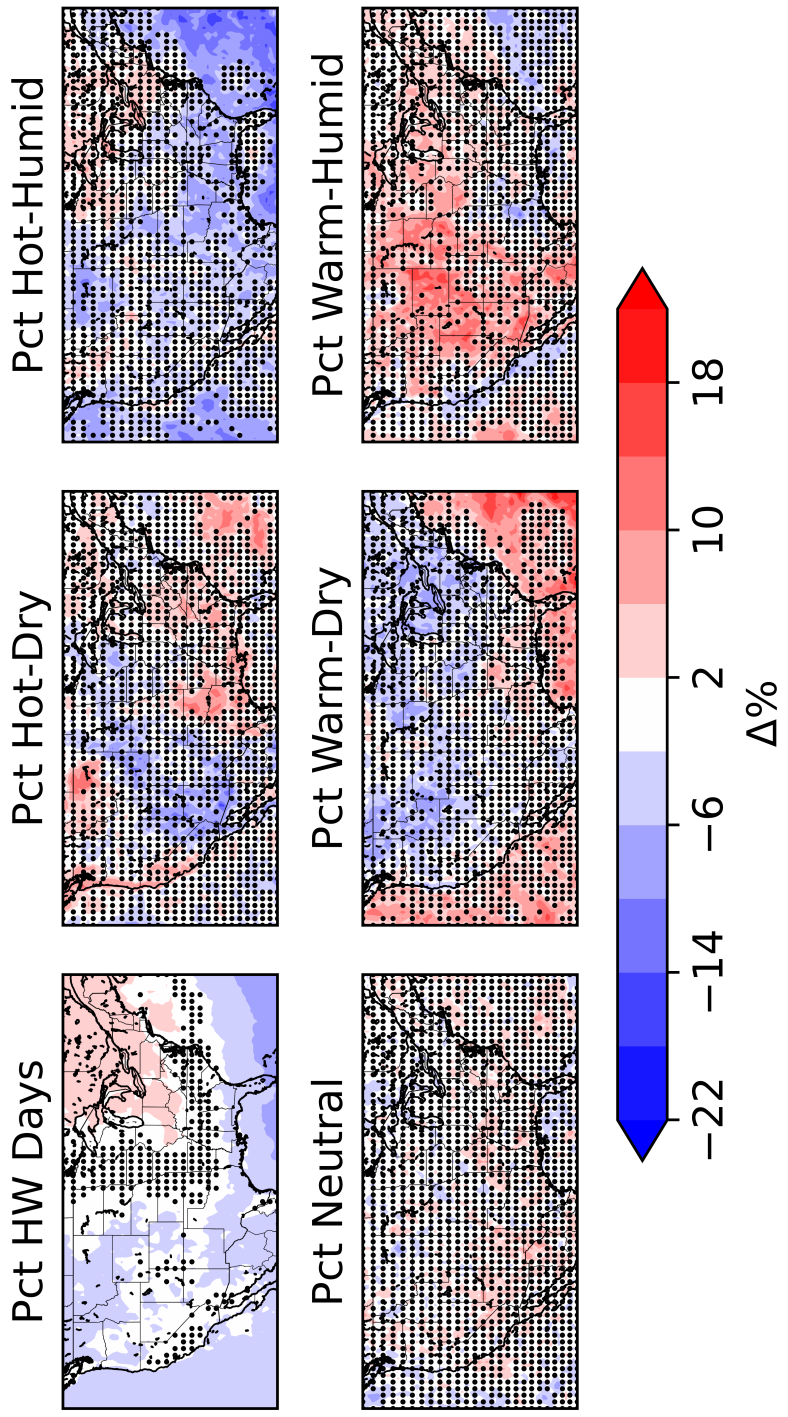

Figure B.4: As in B.1 but for Regime 4 minus all regimes.

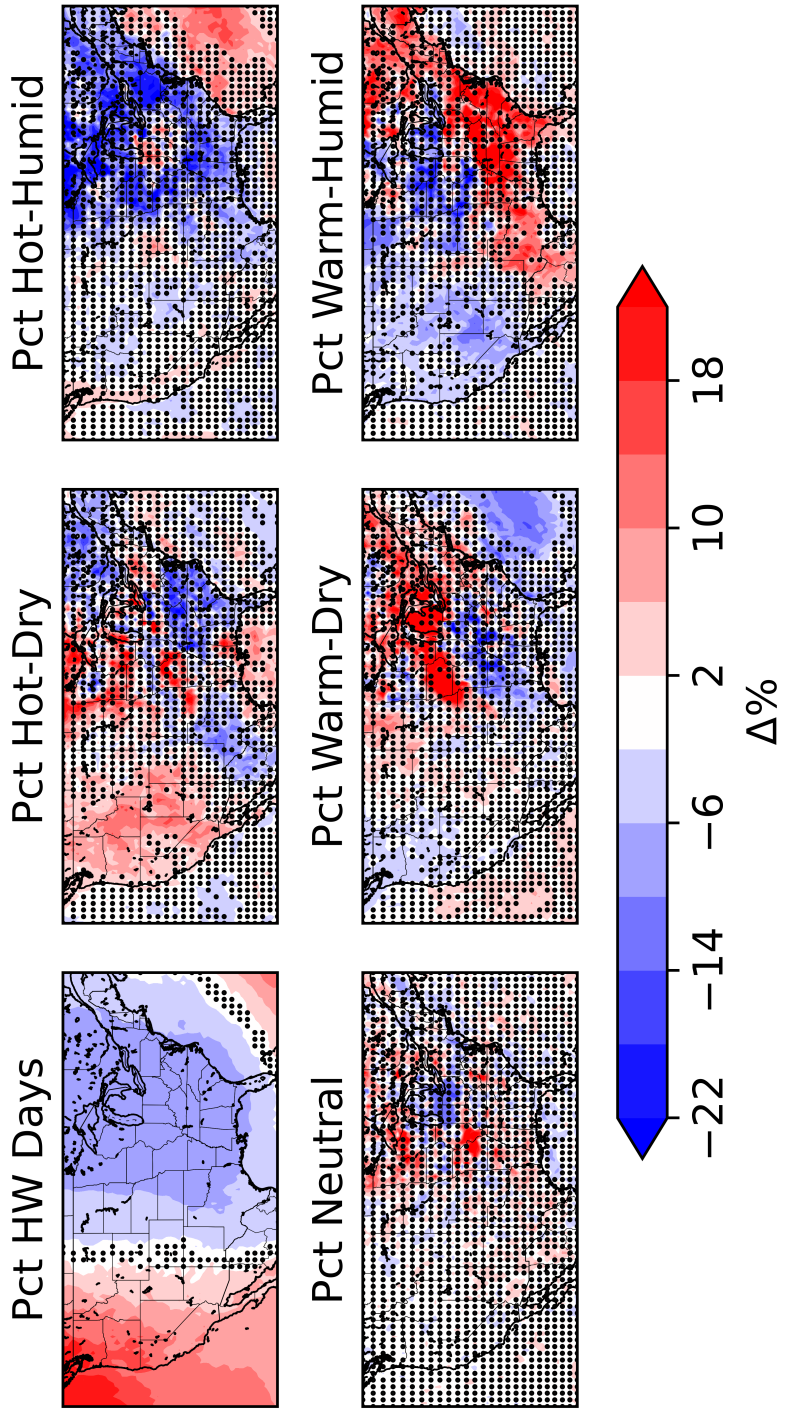

Figure B.5: As in B.1 but for Regime 7 minus all regimes.

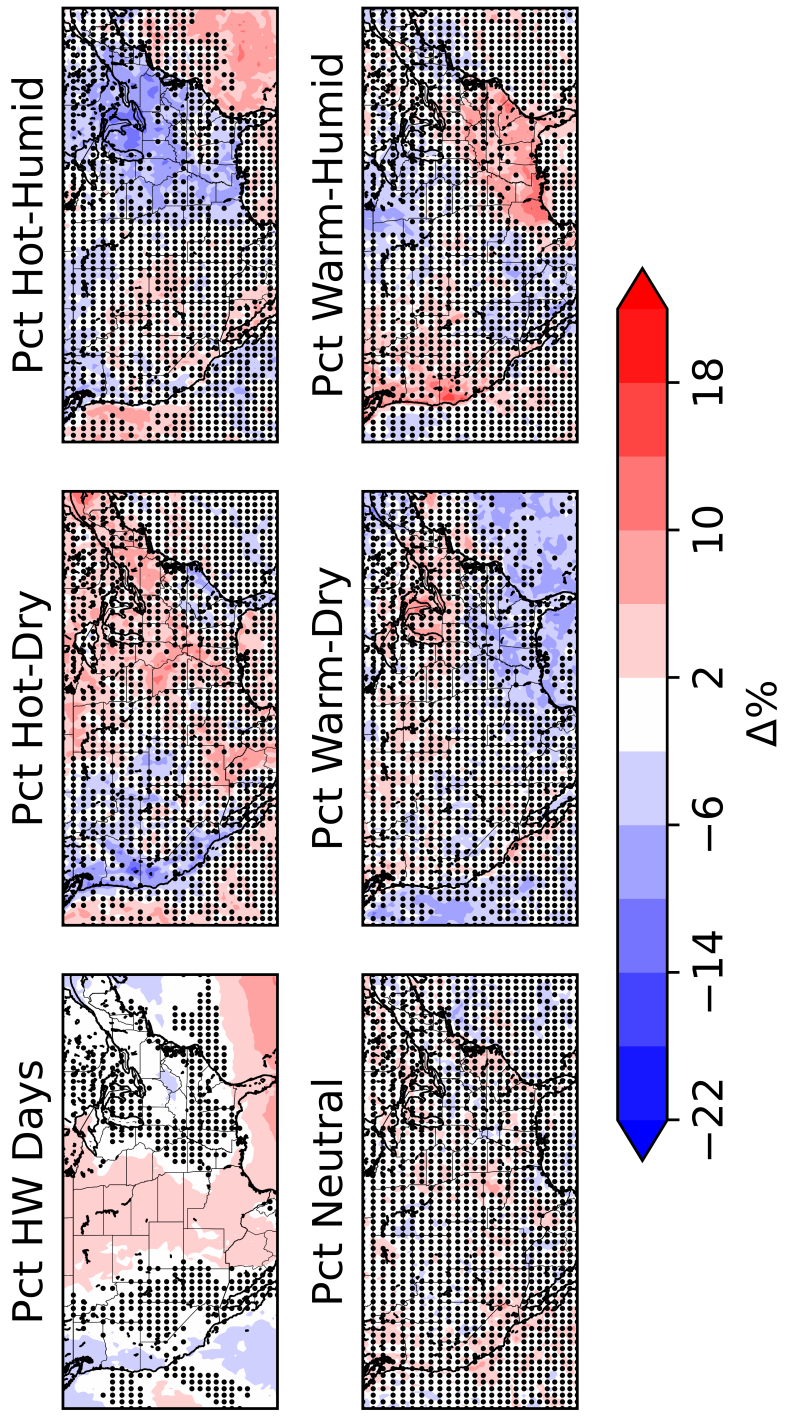

Figure B.6: As in B.1 but for Regime 8 minus all regimes.

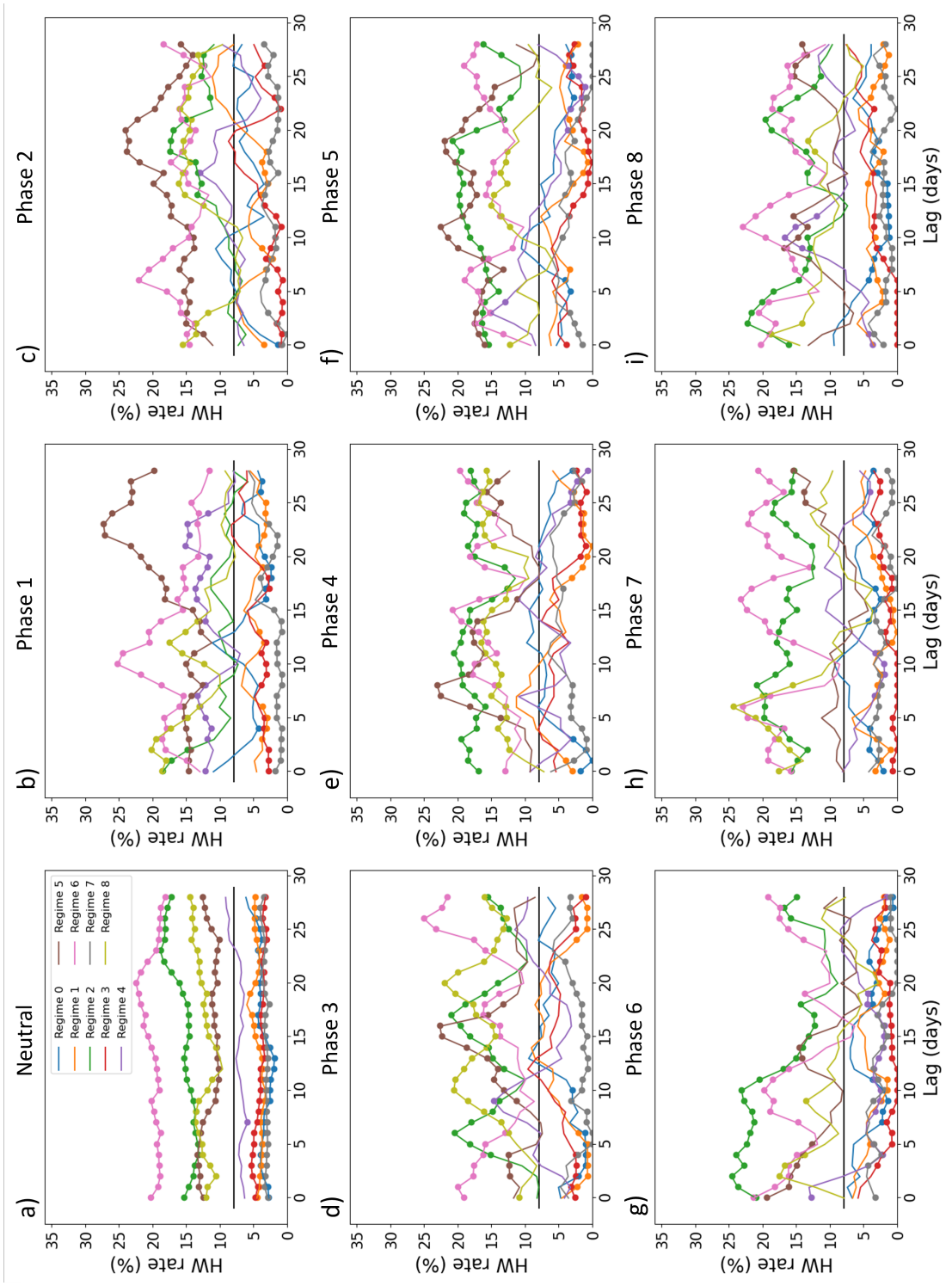

Figure B.7: HW rate for each MJO phase by regime and lead time at the Central USGP location.

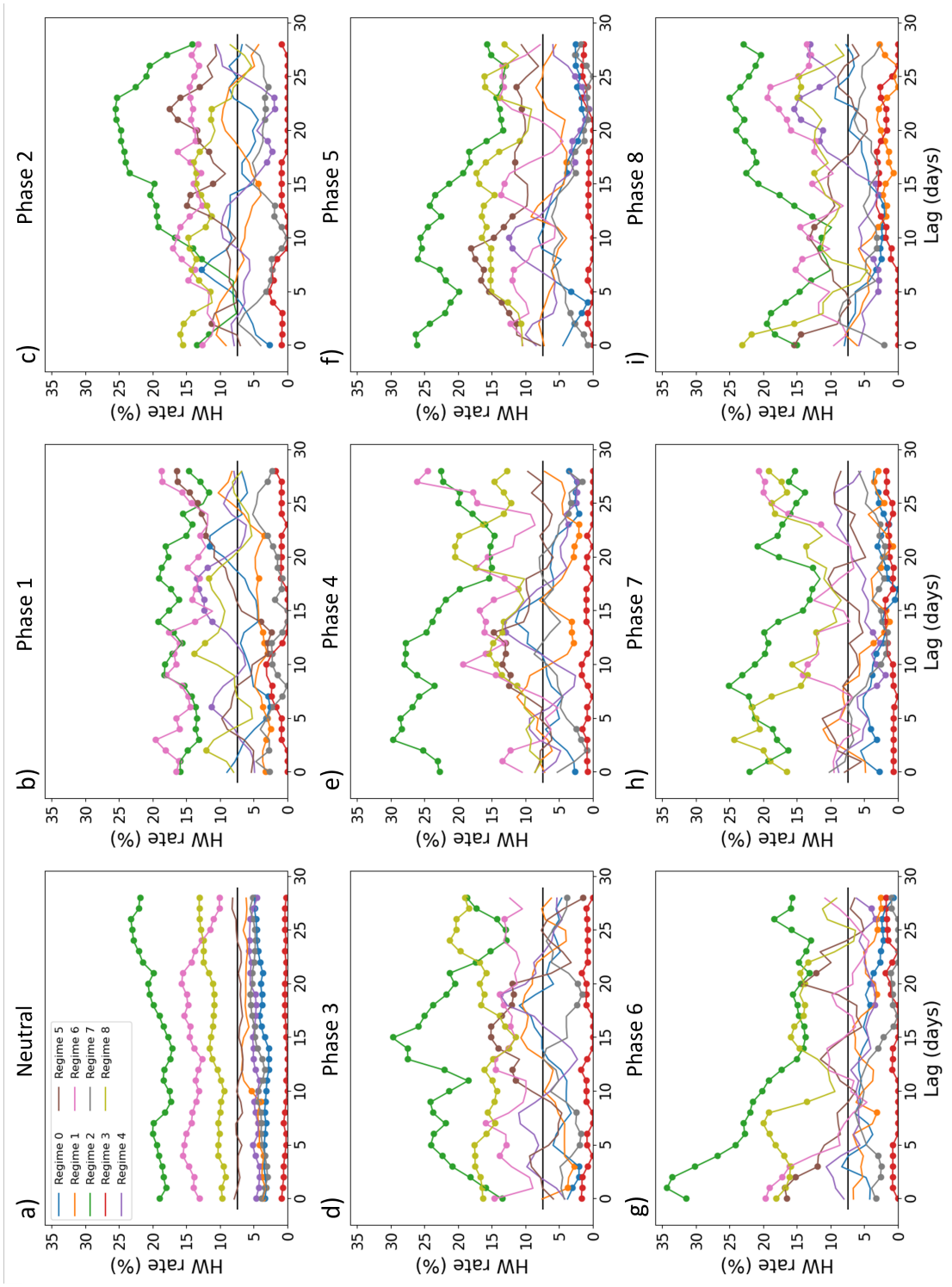

Figure B.8: HW rate for each MJO phase by regime and lead time at the Northern USGP location.

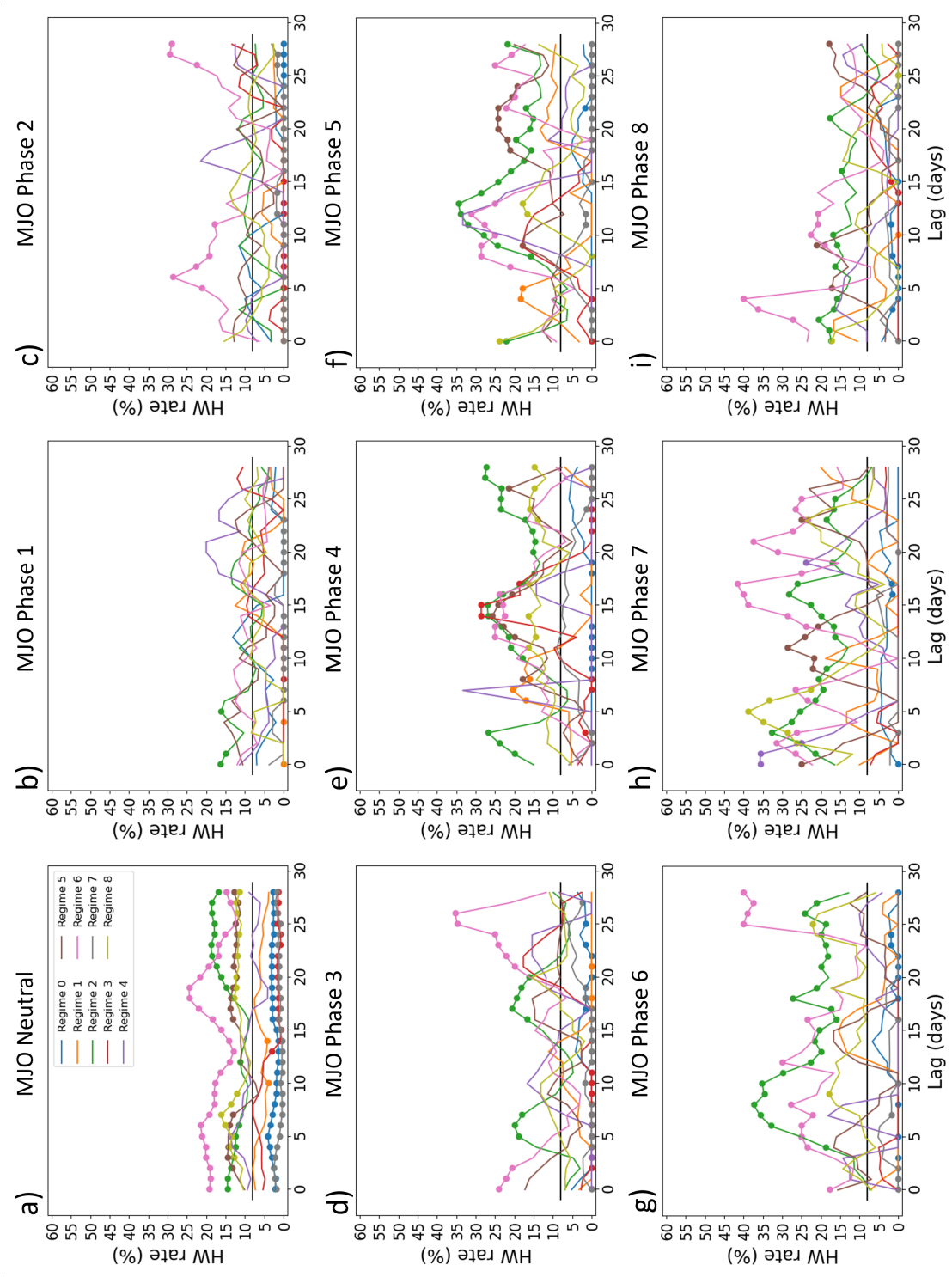

Figure B.9: HW rate for El Niño by MJO Phase and lead time at the Central USGP location.

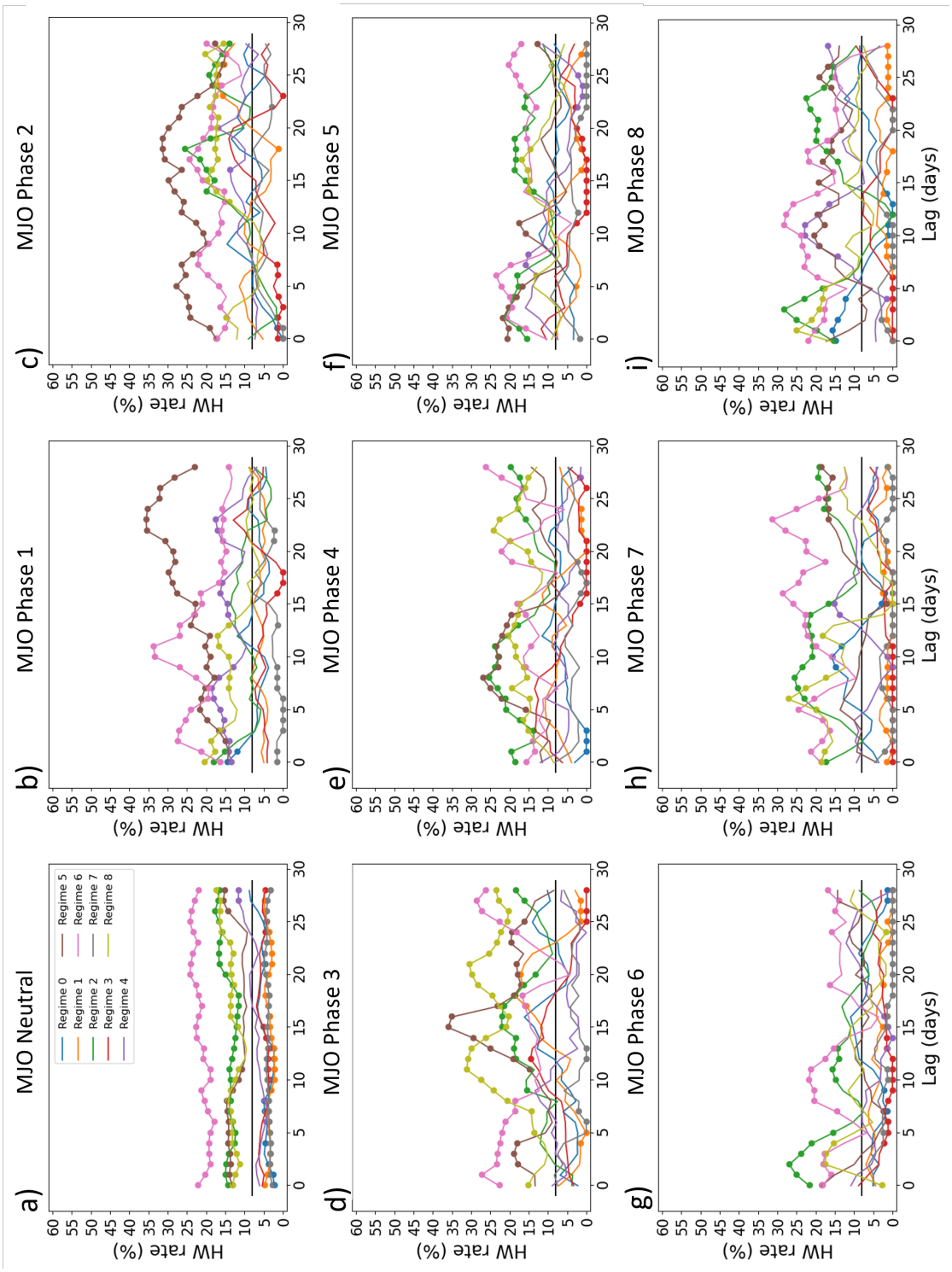

Figure B.10: HW rate for Neutral ENSO phase by MJO Phase and lead time at the Central USGP location.

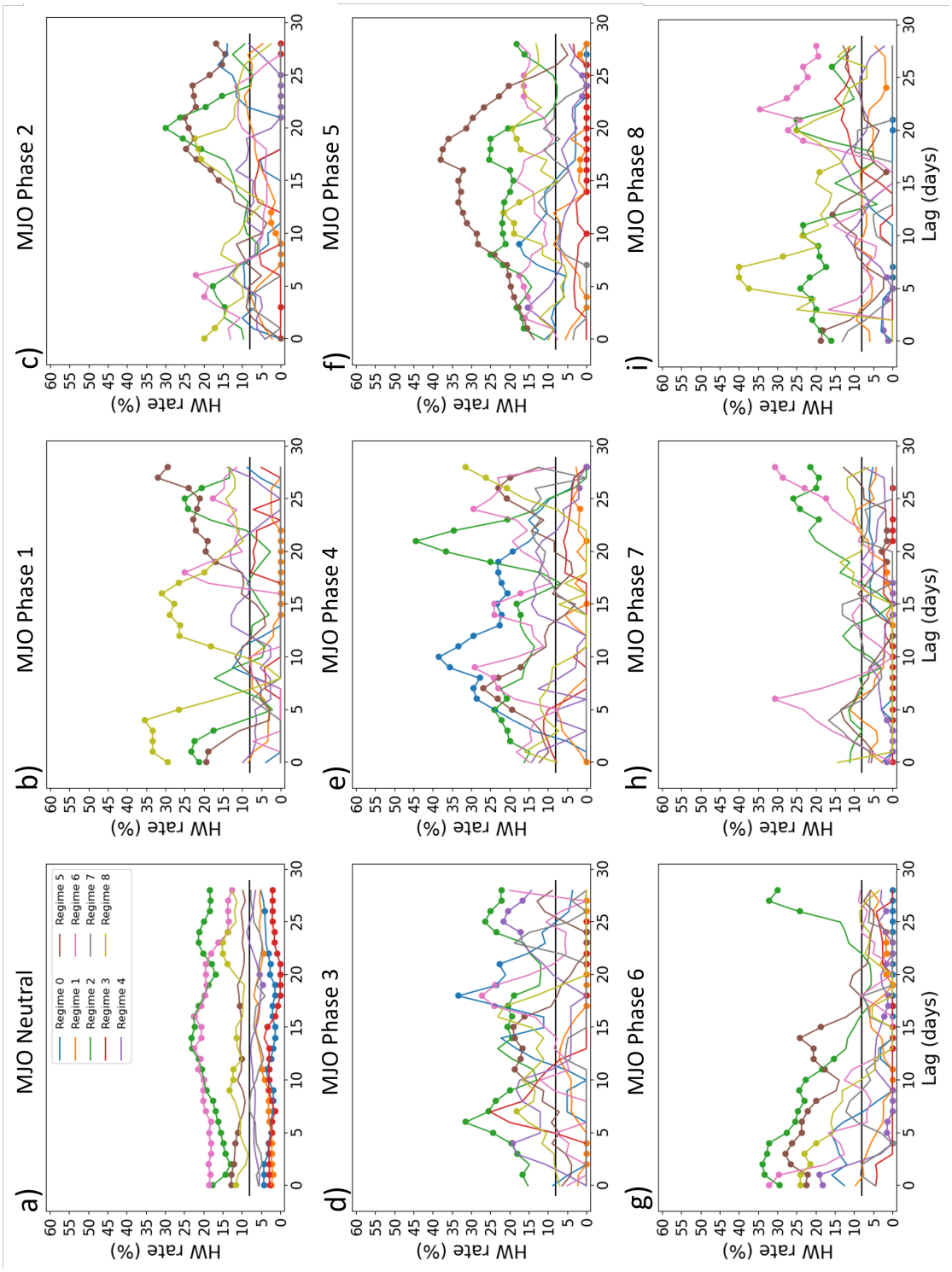

Figure B.11: HW rate for La Niña by MJO Phase and lead time at the Central USGP location.

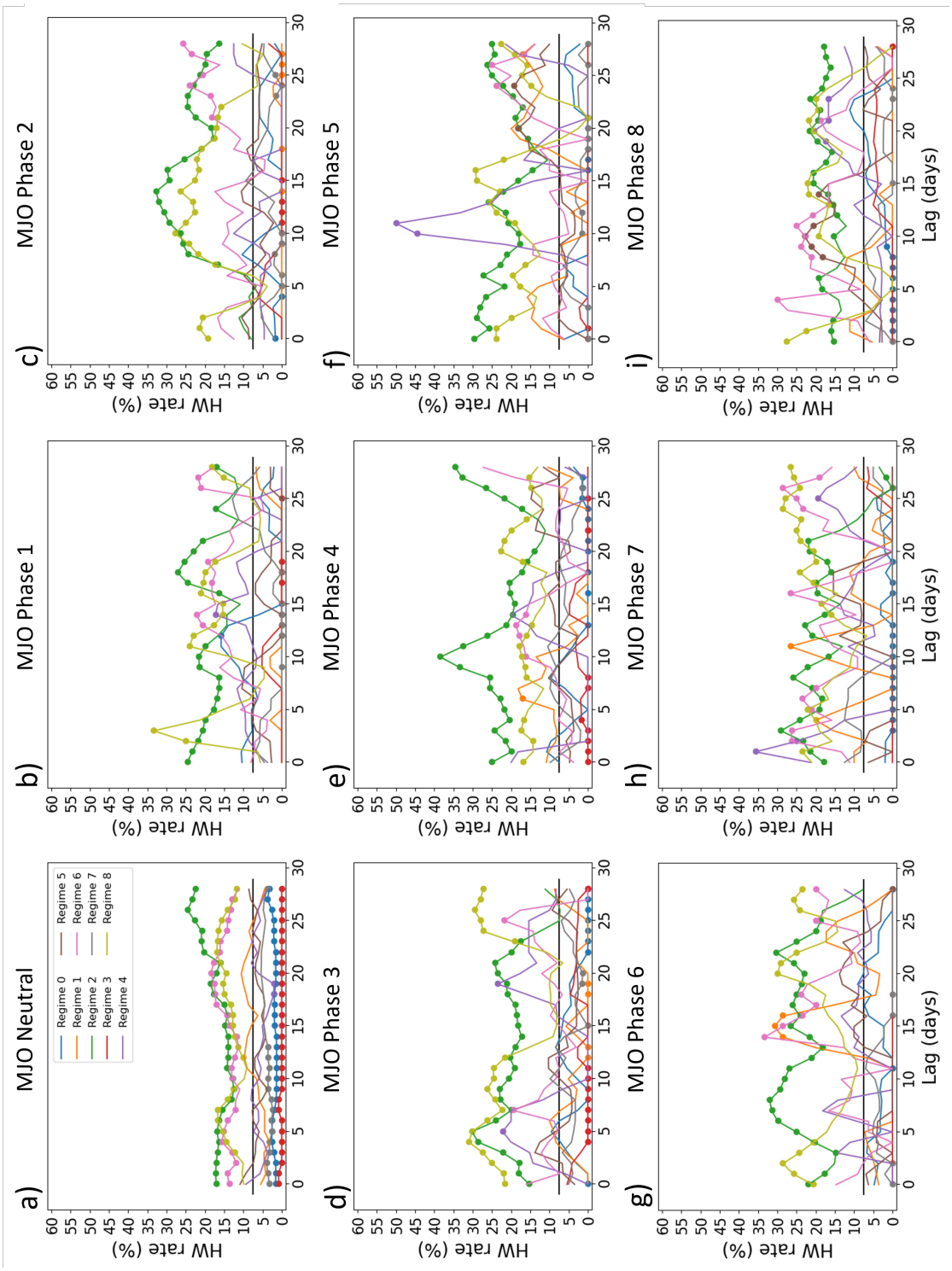

Figure B.12: HW rate for El Niño by MJO Phase and lead time at the Northern USGP location.

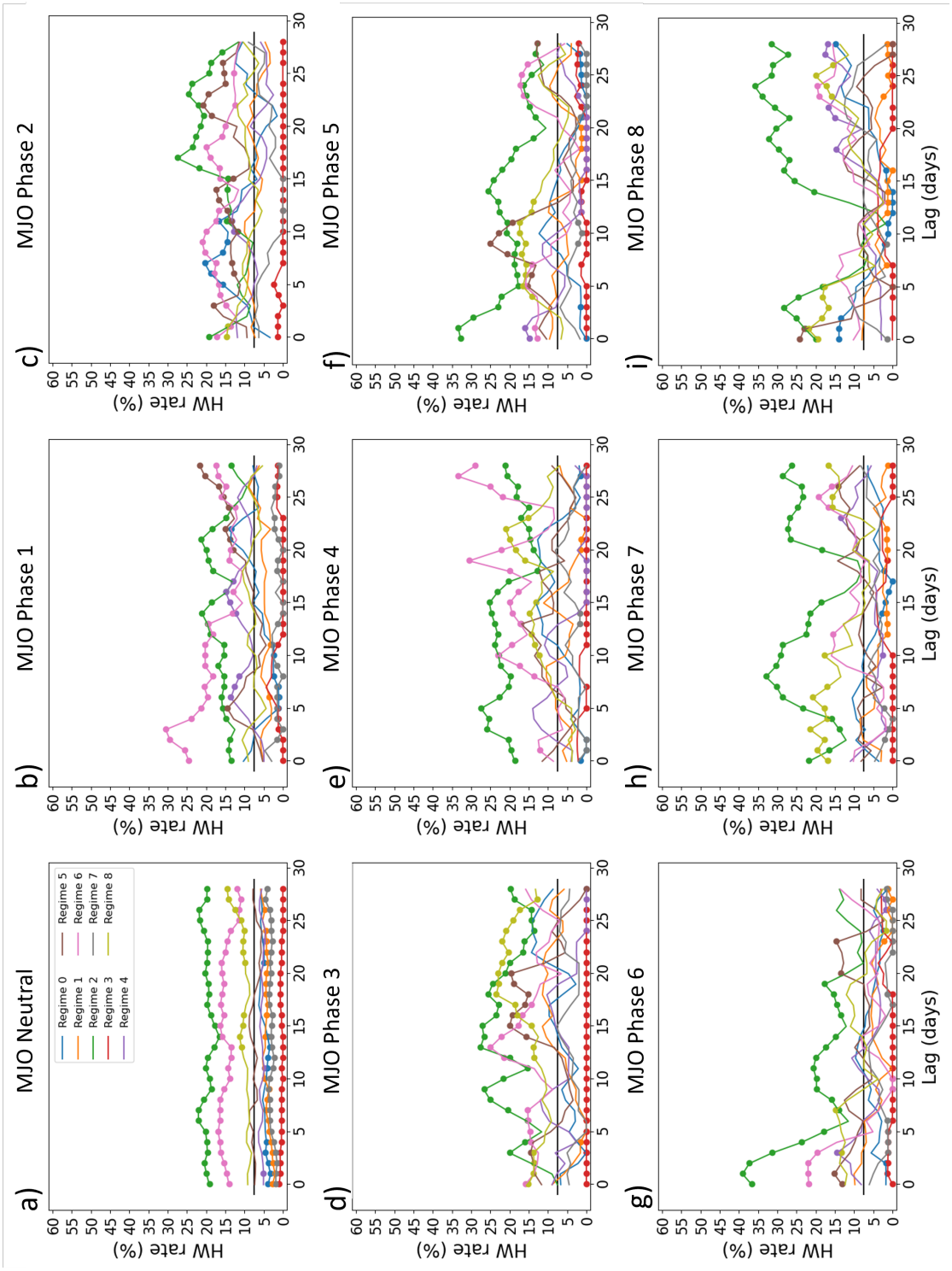

Figure B.13: HW rate for Neutral ENSO phase by MJO Phase and lead time at the Northern USGP location.

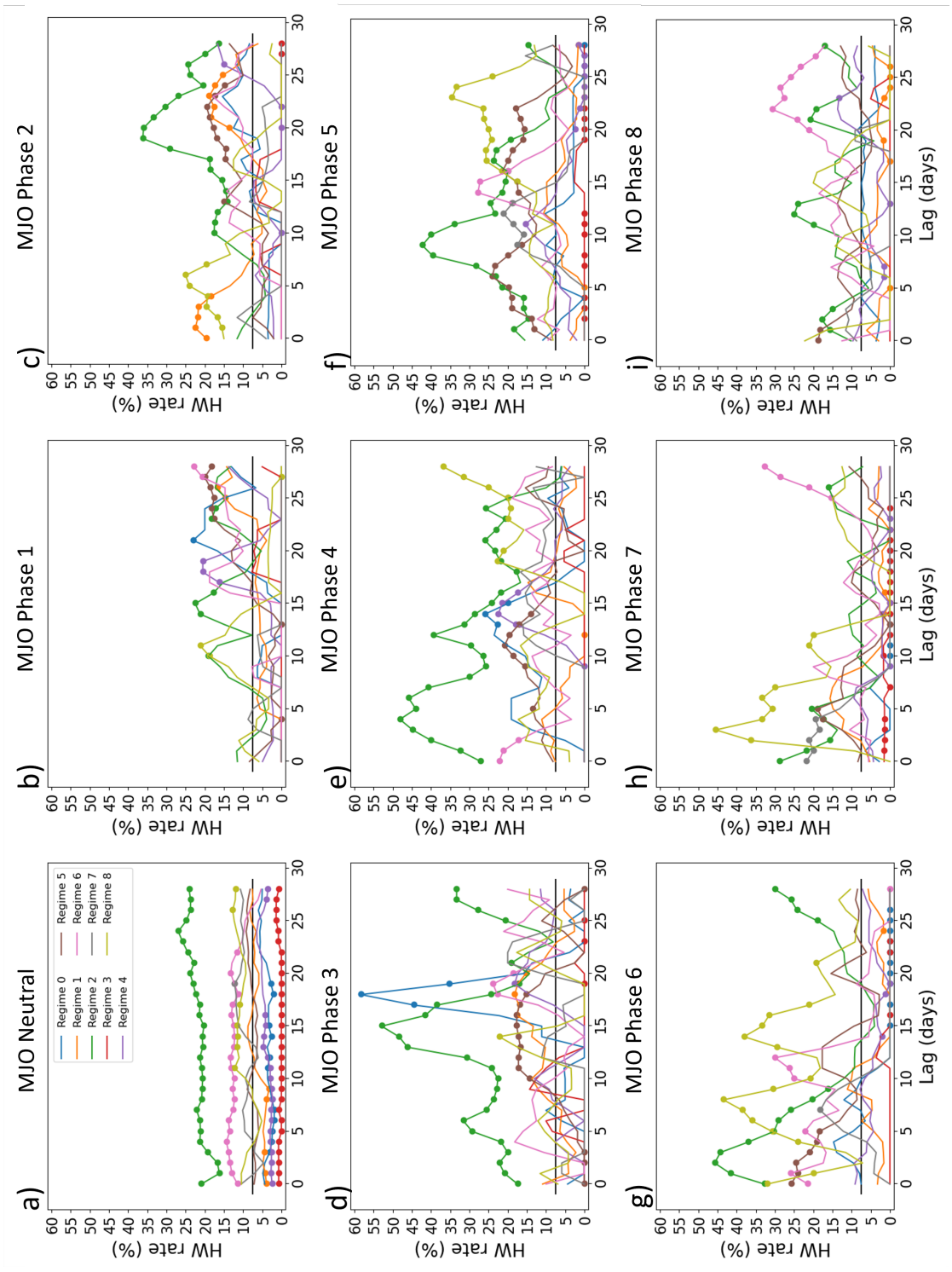

Figure B.14: HW rate for La Niña by MJO Phase and lead time at the Northern USGP location.

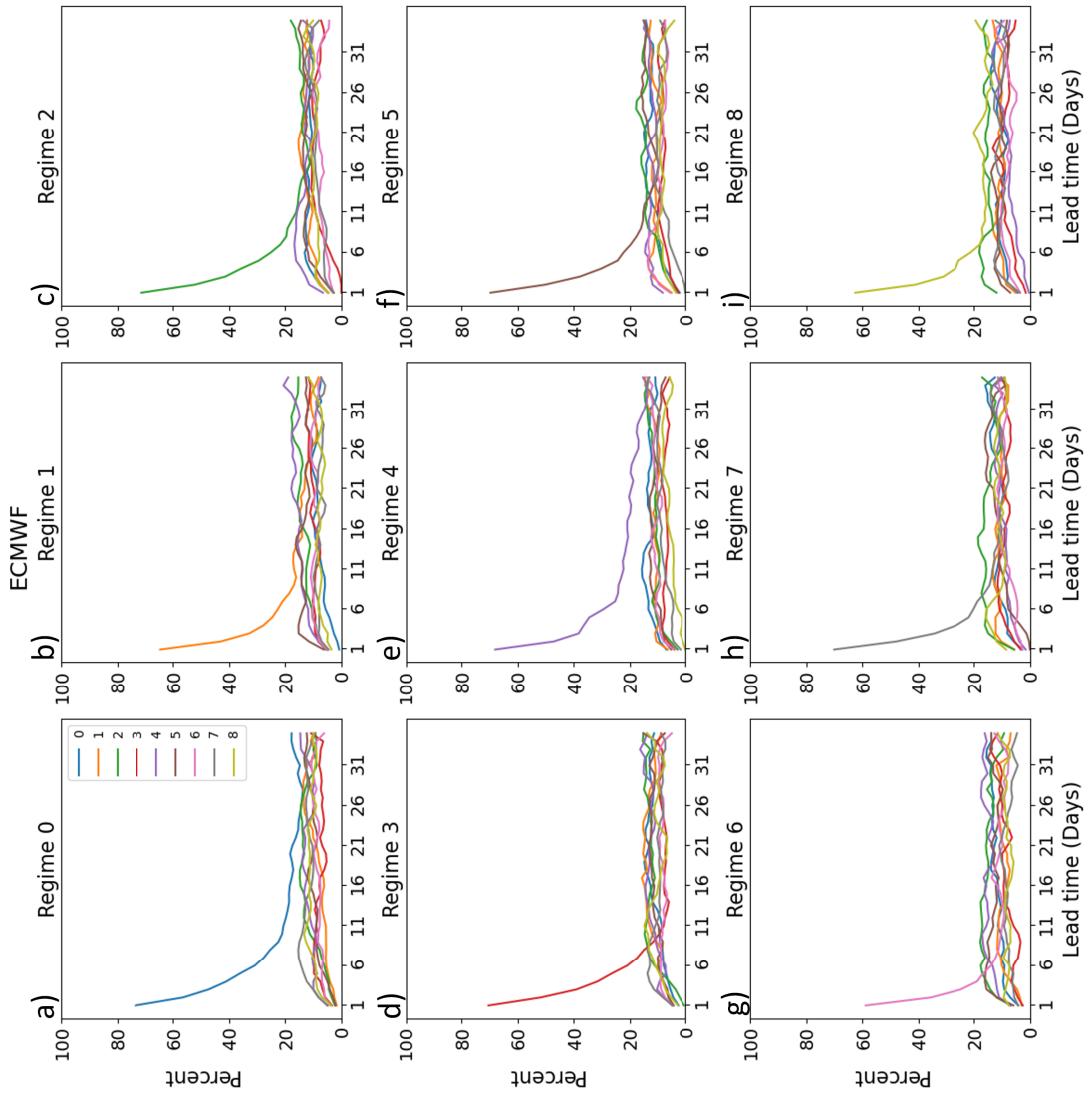

Figure B.15: Frequency of each regime occurring at each lag time up to day 28 by day 0 regime for ECMWF model forecasts.

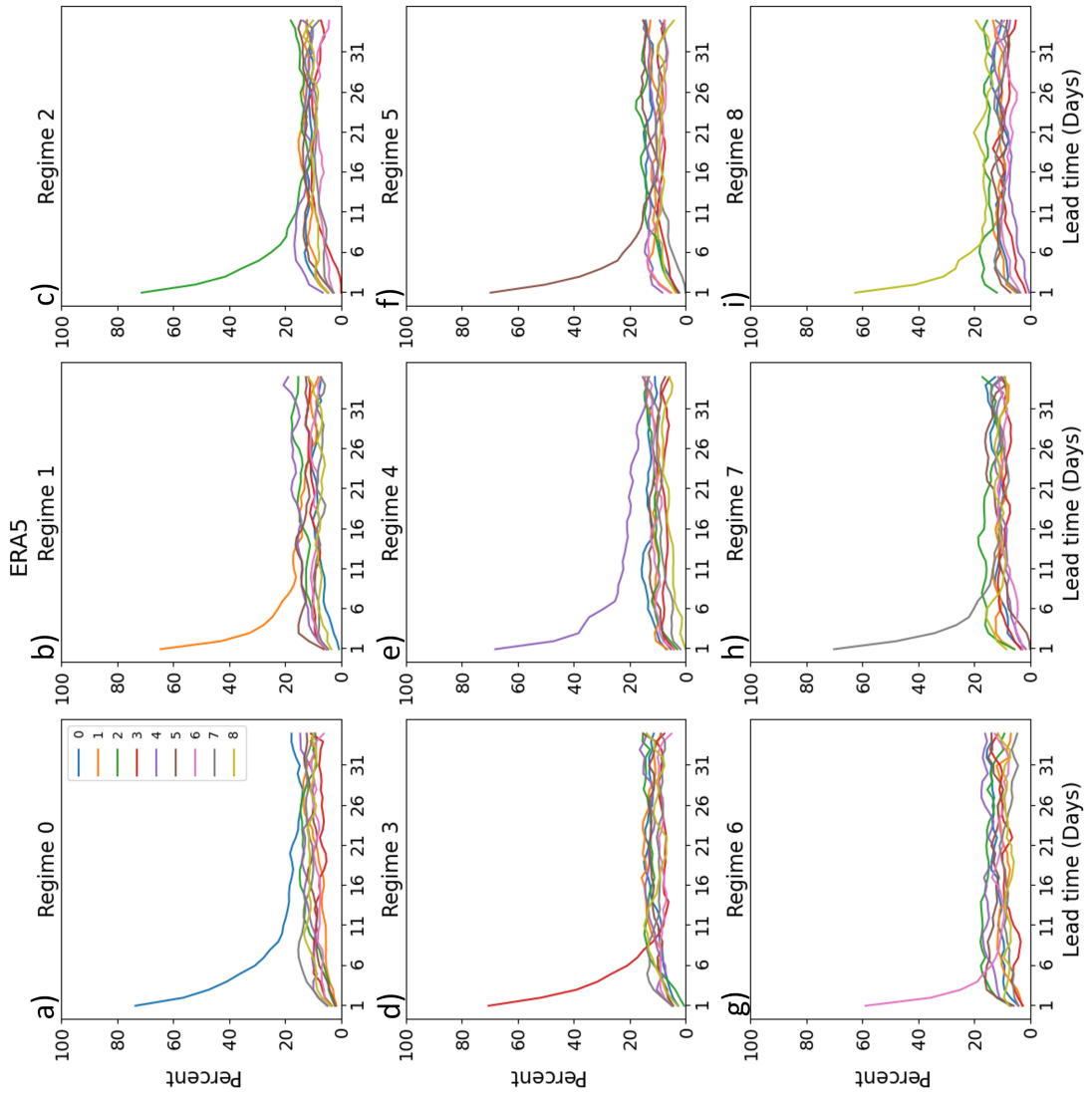

Figure B.16: Frequency of each regime occurring at each lag time up to day 28 by day 0 regime for ERA5 reanalysis.